

Application of Two-Dimensional Finite-Difference
Wave Simulation to Earthquakes, Earth Structure,
and Seismic Hazard

Thesis by
John Emilio Vidale

In Partial Fulfillment of the Requirements
for the Degree of
Doctor of Philosophy

California Institute of Technology
Pasadena, California

1987

(submitted November 14, 1986)

Acknowledgements

The Caltech Seismo Lab deserves much of the credit for germinating and nurturing the research in this thesis; I cringe at the remembrance of the marauding hordes of ridiculous ideas I've had quickly dispersed by those who had heard them before. The Gutenberg and NSF Fellowships that supported me for my first four years at Caltech removed the burden of wondering who my research should please; it need only entertain me. Heidi Houston provided invaluable support, procured advantageous housing, and reminded me to think about tomorrow while entertaining myself with my research today.

Thanks to Profs. Don Helmberger and Rob Clayton for conjuring scores of new ideas to try, some of which are represented in this thesis (and some that we now know to exile immediately if they reappear). My mother introduced me to science but (thank goodness) kept me away from geochemistry. My officemates, Harold, Mario, Bad Bob, Thorne, Phyllis, and Cathy have prevented the office from ever falling into a rut or even allowing only mild disorder, preferring instead alternating arguments, intense work, and celebrations.

Abstract

Although the earth is 3-dimensional (3-D), numerical simulations of wave propagation through laterally heterogeneous media are easier to formulate and more practical to use in 2-D. In this thesis, schemes to model seismic wave propagation through laterally varying structures with 2-D numerical algorithms are developed and applied to earthquake and explosion problems.

In Chapter 1, 2-D source expressions that have the same radiation patterns as their 3-D counterparts are derived which can rectify the following three problems: the use of 2-D simulations generally results in "line source tails" on what would be impulsive arrivals in 3-D, $1/\sqrt{R}$ rather than $1/R$ amplitude decay for body waves, and no decay rather than $1/\sqrt{R}$ amplitude decay for surface waves. Because this technique approximately transforms waves from a cartesian 2-D grid to a cylindrically symmetric 3-D world, slightly anisotropic geometrical spreading in 2-D better approximates isotropic spreading in 3-D than simple isotropic spreading in 2-D does. In Section 1.7, a correction to the explosive source expression reduces energy traveling vertically out of the source region, but leaves unchanged the energy traveling laterally out of the source region. In some cases, this correction will significantly improve the results of using a 2-D grid to simulate elastic wave propagation from an explosive point source.

In Chapter 2, synthetic seismograms are constructed for the strong motions of the 1968 Borrego Mountain earthquake recorded at El Centro. A good fit to the data results from using the laterally varying model determined by a detailed refraction survey and the source parameters determined by

teleseismic waveform modeling. Shallow faulting is no longer necessary to explain the long-period surface-wave development.

Synthetic seismograms calculated for the 1971 San Fernando earthquake show strong effects due to lateral variation in sediment thickness in the San Fernando valley and the Los Angeles basin. Using previously determined basin structure and teleseismically determined source parameters, two-dimensional SH and P-SV finite difference calculations can reproduce the amplitude and duration of the strong motion velocities recorded across the basins in Los Angeles in the period range from 1 to 10 seconds. The edges of basins nearest the seismic source show ground motion amplification up to a factor of three, and tend to convert direct shear waves into Love and Rayleigh waves that travel within the basins. The computed motions are sensitive to the mechanism and location of earthquakes. A strike-slip earthquake on the Newport-Inglewood fault zone, for example, would produce different patterns of peak velocity and duration of shaking across the San Fernando and Los Angeles basins.

In Chapter 3, the effect of shallow station structure and lateral velocity variation are investigated for records of the Amchitka explosion Milrow. The differences between the Mueller-Murphy, Helmberger-Hadley, and von Seggern-Blandford reduced displacement potential (RDP) source representations are small compared to the differences between using various possible velocity structures.

Creager and Jordan (1986) propose that penetration of subducting slabs under the Kurile Islands and other subduction zones to depths of at least 1000 km is necessary to explain the travel time anomalies of deep earthquakes.

Such penetration would also affect the amplitudes and waveforms of the body waves from these earthquakes. In Chapter 4, synthetic seismograms appropriate for a record section in a plane perpendicular to the strike of the slab are presented using a coupled finite-difference and Kirchhoff method. An inferred shear-wave version of the compressional-wave velocity structure of Creager and Jordan (1986) produces an amplitude decrease up to a factor of four and waveform broadening up to 20 seconds for SH arrivals with a take-off angle pointing straight down the slab. Slabs that extend only 300 km below the earthquake but are half as thick and twice as anomalously fast as Creager and Jordan's (1986) velocity model will roughly preserve the travel time variation pattern, and show less waveform broadening, but produce first arrivals that are emergent. Slabs that become thicker with depth show less waveform broadening. Reconciliation of the amplitude, waveform distortion, and timing of body waves from deep events is necessary to understand the geometry of slabs near and below the 650 km discontinuity.

Table of Contents

Acknowledgements	ii
Abstract	iii
Chapter 1: Explosive and double couple sources for 2-D FD wave propagation	
1. Introduction	1
2. Derivation of explosive source expressions	2
3. Derivation of double couple source expressions	6
4. Algorithm for coupling expressions with numerical scheme	18
5. Illustration of various sources	21
6. Tests of accuracy	27
7. Limitations and a more accurate explosive source	35
Chapter 2: Application to modeling the strong motions of earthquakes	
1. Introduction	52
2. The El Centro recording of the Borrego Mountain earthquake	54
3. The San Fernando earthquake: forward modeling	66
4. The San Fernando earthquake: implications for estimating strong motions	92
5. Conclusions	109
Chapter 3: Application to modeling the strong motions of the explosion Milrow	
1. Introduction	112
2. Effects of laterally varying structures	112
3. Effects of various source models	120
4. Conclusions	127
Chapter 4: Application to investigate deep structure of subducting slabs	
1. Introduction	129
2. Waveform distortions predicted by published models	130
3. Conclusions	140
References	143

Chapter 1

Explosive and double couple sources for 2-D FD wave propagation

1.1 Introduction

Wave propagation problems in complicated geological structures have generated considerable interest in recent years. Two approaches have gained popularity; one is based on approximations near the wavefront or generalizations of ray theory, the other uses the full wave equation with a method like finite-differences (FD). Ray theory has been developed by Chapman (1978) using the WKBJ method, and Cerveny et al. (1982), and more recently Madariaga and Papadimitriou (1984), among others, have been developing the Gaussian beam approach.

In this thesis, the FD techniques of Clayton and Vidale (1986) are used. Other FD techniques (Witte and Richards, 1986; Virieux, 1986) and finite element techniques (Marfurt, 1984) can do similar problems. Finite-difference (FD) techniques with transparent boundary conditions for elastic models are only now becoming economically viable at frequencies of interest. The source descriptions to allow approximate explosion and double-couple point-source seismograms to be made from 2-D FD grids are developed in this chapter.

Ideally, one would like to simulate elastic wave propagation in the earth with 3-dimensional numerical grids. Such experiments are, in fact, now being attempted (Edwards et al., 1985, and Stevens and Day, 1985). They require,

however, very large amounts of computer time and allow energy to propagate only a limited number of wavelengths, so that they do not apply to many problems of geophysical interest (see, for example, Figure 13.11 of Aki and Richards, 1980, for the range of application of various methods). Two-dimensional numerical grids have been used for many years to provide insight into 3-dimensional wave propagation problems (see Boore, 1972, for example). In this chapter, source expressions are developed that allow the simulation of point slip dislocations and explosions with 2-D numerical grids. Such formulations are most accurate for energy that propagates horizontally away from the source. This is partly because the asymptotic solution is most accurate for a large range, high frequency, and non-vertical take-off angle, but also because a 2-D grid does not properly simulate 3-D geometrical spreading. The ray and the more full wave approaches should be used together to model data because rays are the most accurate at high frequency while the FD method computes the full solution, but becomes very expensive at high frequencies.

1.2 Derivation of explosive source expressions

We begin by finding the displacement due to an explosive point source in a whole-space. At some distance outside the elastic radius from an explosion we require the displacement potential to satisfy the behavior of a spherical wave, which is

$$\phi_p = 1/R f(t - R/\alpha) \quad (1)$$

where f defines a source time function, t is time, α is the compressional wave velocity, and $R = \sqrt{z^2 + r^2}$ is the distance between the source location and

the receiver, see Figure 1.1. The Laplace transformed solution in cylindrical co-ordinates (after Strick, 1959) is

$$\overline{\phi}_p(r, z, s) = f(s) \frac{2}{\pi}(s) \operatorname{Im} \int_{\delta}^{i\infty + \delta} K_0(spr) e^{-s\eta|z-h|} \frac{p}{\eta} dp, \quad (2)$$

where p is the ray parameter, s is the transform variable over time, K_0 the modified Bessel function, $\eta = \sqrt{1/\alpha^2 - p^2}$, h is the source depth, and δ is a small number which only serves to keep the integration off the complex axis. Using the asymptotic expansion of K_0 and keeping the first term only, we obtain

$$\overline{\phi}_p(r, z, s) = \sqrt{\frac{2}{\pi rs}} \operatorname{Im} \int_0^{i\infty + \delta} \frac{\sqrt{p}}{\eta} e^{-s(pr + \eta|z-h|)} dp \quad (3)$$

where we have assumed that $f(s) = 1/s$, or that $f(t)$ is a step function. This first term approximation is valid for large spr and is not valid directly above the source (small p), at very small ranges (small r), or at very long periods (small s). This approximation is also used in Section 1.3 for earthquake sources; see equation (20). This integral occurs often in GRT and is solved by the Cagniard-de Hoop technique, (see de Hoop, 1960, or Helmberger, 1983). One defines $t = pr + \eta|z-h|$ and requires t to have real values along a contour in the complex p plane. Thus,

$$\phi_p(r, z, t) = \sqrt{\frac{2}{r}} \frac{1}{\pi} \left[\frac{1}{\sqrt{t}} * J(t) \right], \quad (4)$$

where

$$J(t) = \operatorname{Im} \left[\frac{\sqrt{p}}{\eta} \frac{dp}{dt} \right] \quad (5)$$

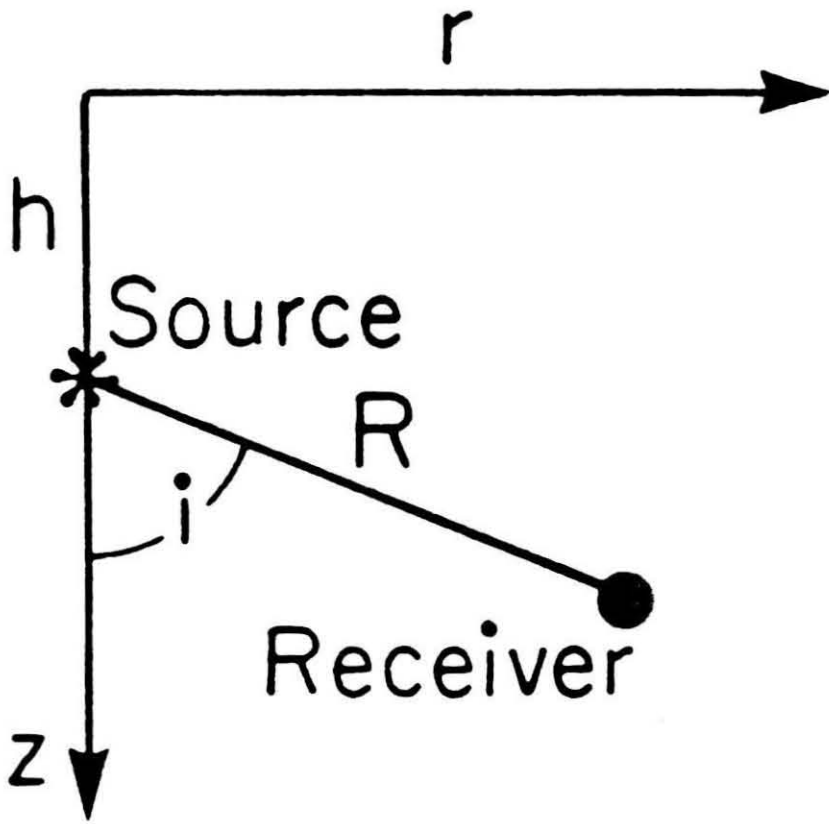


Figure 1.1 Conventions for cylindrically symmetric geometry.

or more simply

$$J(t) = \text{Re}(\sqrt{p}) \frac{H(t - R/\alpha)}{\sqrt{t^2 - \frac{R^2}{\alpha^2}}}$$

and

$$p = \frac{r}{R^2}t + i \sqrt{t^2 - \frac{R^2}{\alpha^2}} \frac{|z-h|}{R^2}. \quad (6)$$

Note that at times near $t = R/\alpha$

$$p = \frac{\sin i}{\alpha} \equiv p_0 \quad (7)$$

and hence p_0 becomes the geometric ray parameter. Substituting equation (5) into equation (4), and assuming $p = p_0$, we obtain

$$\phi_p = \frac{1}{R} H(t - R/\alpha)$$

as we should.

However, from the work of Gilbert and Knopoff (1961), we have the solution for the line source excitation as

$$\phi_L(r, z, t) = \text{Im} \left[\frac{1}{\eta} \frac{dp}{dt} \right] \quad (8)$$

or more explicitly

$$\phi_L = \frac{H(t - R/\alpha)}{\sqrt{t^2 - R^2/\alpha^2}}, \quad (9)$$

where the line source is perpendicular to the r and z axes, (see Figure 1.1). Thus, we can find the point source solution ϕ from the line source solution J as shown in equation (4) if $J = \sqrt{p} \phi_L$ is used. We use this trick to study

the effect of laterally heterogeneous structure with the FD method. The displacements derived from the potential in equation (8) are used to drive the FD grid, as described in Section 1.4. Line source vertical and horizontal seismograms $\tilde{W}(t)$ and $\tilde{Q}(t)$ extracted from the FD grid are transformed to point source vertical and radial seismograms $\mathbf{W}(t)$ and $\mathbf{Q}(t)$:

$$\mathbf{W}(t) = \sqrt{\frac{2}{r}} \frac{1}{\pi} \left[\frac{H(t)}{\sqrt{t}} * \tilde{W}(t) \right] \quad (10a)$$

$$\mathbf{Q}(t) = \sqrt{\frac{2}{r}} \frac{1}{\pi} \left[\frac{H(t)}{\sqrt{t}} * \tilde{Q}(t) \right] \quad (10b)$$

The absence of the \sqrt{p} in equation (8) means the solution is approximate. The mapping between the line-to-point source method discussed here breaks down near $p_0 = 0$ or directly above and below the source, as may be seen in Section 1.6. In the case of a laterally varying structure, each arrival in a record may have a different ray parameter p , but we can only correct for a constant $\sqrt{p_0}$. The result is that the importance of vertically as opposed to horizontally traveling energy is overemphasized in the line source compared to the point source case. A more accurate source expression for explosions is introduced in Chapter 1.7.

1.3 Derivation of double couple source expressions

We suppose that motions produced by earthquakes can be simulated by assuming a distribution of shear dislocations.

Harkrider (1976) has obtained convenient forms of displacement potentials starting with Haskell's representation, which allows a discontinuity in displacement across a fault plane. The results, after Langston and Helmberger (1975), in terms of Laplace-transformed displacements along the vertical, tangential, and radial directions are:

$$\begin{aligned}\hat{W} &= \frac{\partial \hat{\phi}}{\partial z} + sp \hat{\Omega} \\ \hat{V} &= \frac{1}{r} \frac{\partial \hat{\phi}}{\partial \theta} - \frac{1}{spr} \frac{\partial^2 \hat{\Omega}}{\partial z \partial \theta} - \frac{\partial \hat{\chi}}{\partial r} \\ \hat{Q} &= \frac{\partial \hat{\phi}}{\partial r} - \frac{1}{sp} \frac{\partial^2 \hat{\Omega}}{\partial r \partial z} + \frac{1}{r} \frac{\partial \hat{\chi}}{\partial \theta},\end{aligned}\tag{11}$$

where z , r and θ are the vertical, radial, polar angle coordinates, respectively. The P wave potential (ϕ), the SV wave potential (Ω), and the SH wave potential (χ) are:

P-wave:

$$\begin{aligned}\hat{\phi} &= \frac{M_0}{4\pi\rho} \frac{2}{\pi} \operatorname{Im} \int_c^{i\infty+c} C_1(p) \frac{p}{\eta_\alpha} \exp(-s \eta_\alpha |z-h|) K_2(spr) dp A_1(\theta, \lambda, \delta) \\ &+ \frac{M_0}{4\pi\rho} \frac{2}{\pi} \operatorname{Im} \int_c^{i\infty+c} C_2(p) \frac{p}{\eta_\alpha} \exp(-s \eta_\alpha |z-h|) K_1(spr) dp A_2(\theta, \lambda, \delta) \\ &+ \frac{M_0}{4\pi\rho} \frac{2}{\pi} \operatorname{Im} \int_c^{i\infty+c} C_3(p) \frac{p}{\eta_\alpha} \exp(-s \eta_\alpha |z-h|) K_0(spr) dp A_3(\theta, \lambda, \delta)\end{aligned}\tag{12}$$

SV-waves:

(13)

$$\begin{aligned}\hat{\Omega} = & \frac{M_0}{4\pi\rho} \frac{2}{\pi} \operatorname{Im} \int_c^{i\infty+c} SV_1(p) \frac{p}{\eta_\beta} \exp(-s \eta_\beta |z-h|) K_2(spr) dp A_1(\theta, \lambda, \delta) \\ & + \frac{M_0}{4\pi\rho} \frac{2}{\pi} \operatorname{Im} \int_c^{i\infty+c} SV_2(p) \frac{p}{\eta_\beta} \exp(-s \eta_\beta |z-h|) K_1(spr) dp A_2 \\ & + \frac{M_0}{4\pi\rho} \frac{2}{\pi} \operatorname{Im} \int_c^{i\infty+c} SV_3(p) \frac{p}{\eta_\beta} \exp(-s \eta_\beta |z-h|) K_0(spr) dp A_3\end{aligned}$$

SH-waves:

(14)

$$\begin{aligned}\hat{\chi} = & \frac{M_0}{4\pi\rho} \frac{2}{\pi} \operatorname{Im} \int_c^{i\infty+c} SH_1(p) \frac{p}{\eta_\beta} \exp(-s \eta_\beta |z-h|) K_2(spr) dp A_4 \\ & + \frac{M_0}{4\pi\rho} \frac{2}{\pi} \operatorname{Im} \int_c^{i\infty+c} SH_2(p) \frac{p}{\eta_\beta} \exp(-s \eta_\beta |z-h|) K_1(spr) dp A_5\end{aligned}$$

where

s = Laplace transform variable

p = ray parameter

$\eta_v = (1/v^2 - p^2)^{1/2}$

h = depth of source

α = compressional velocity

β = shear velocity

ρ = density

M_0 = seismic moment

c is a small constant that offsets path of integration.

In the above equations, the C_i , SV_i and SH_i are functions of p and are identified with the vertical radiation patterns defined by

$$\begin{aligned}
 C_1 &= -p^2 & SV_1 &= -\epsilon p \eta_\beta & SH_1 &= \frac{1}{\beta^2} \\
 C_2 &= 2 \epsilon p \eta_\alpha & SV_2 &= (\eta_\beta^2 - p^2) & SH_2 &= \frac{\epsilon}{\beta^2} \frac{\eta_\beta}{p} \\
 C_3 &= (p^2 - 2\eta_\alpha^2) & SV_3 &= 3\epsilon p \eta_\beta
 \end{aligned} \tag{15}$$

where $\epsilon = \begin{cases} +1 & z > h \\ -1 & z < h \end{cases}$.

The azimuthal patterns or orientation constants A_i are determined by:

$$\begin{aligned}
 A_1 &= \sin 2\theta \cos \lambda \sin \delta + 1/2 \cos 2\theta \sin \lambda \sin 2\delta \\
 A_2 &= \cos \theta \cos \lambda \cos \delta - \sin \theta \sin \lambda \cos 2\delta \\
 A_3 &= 1/2 \sin \lambda \sin 2\delta \\
 A_4 &= \cos 2\theta \cos \lambda \sin \delta - 1/2 \sin 2\theta \sin \lambda \sin 2\delta \\
 A_5 &= -\sin \theta \cos \lambda \cos \delta - \cos \theta \sin \lambda \cos 2\delta
 \end{aligned} \tag{16}$$

where

θ = strike from the end of the fault plane

λ = rake angle

δ = dip angle .

The geometry displaying the orientation of the fault in the cylindrical coordinate system is given in Figure 1.2. Note that a strike-slip event is defined by $\lambda = 0^\circ$ and $\delta = 90^\circ$. In equations (12) through (16), the subscripts 1 and 4 correspond to a pure strike-slip fault (SS), the subscripts 2 and 5 correspond to a pure normal or dip-slip fault (DS), and the subscript 3 corresponds to a 45° dip-slip (DD) fault. Any fault orientation can be obtained by a linear combination of these three (see Burridge et al., 1964).

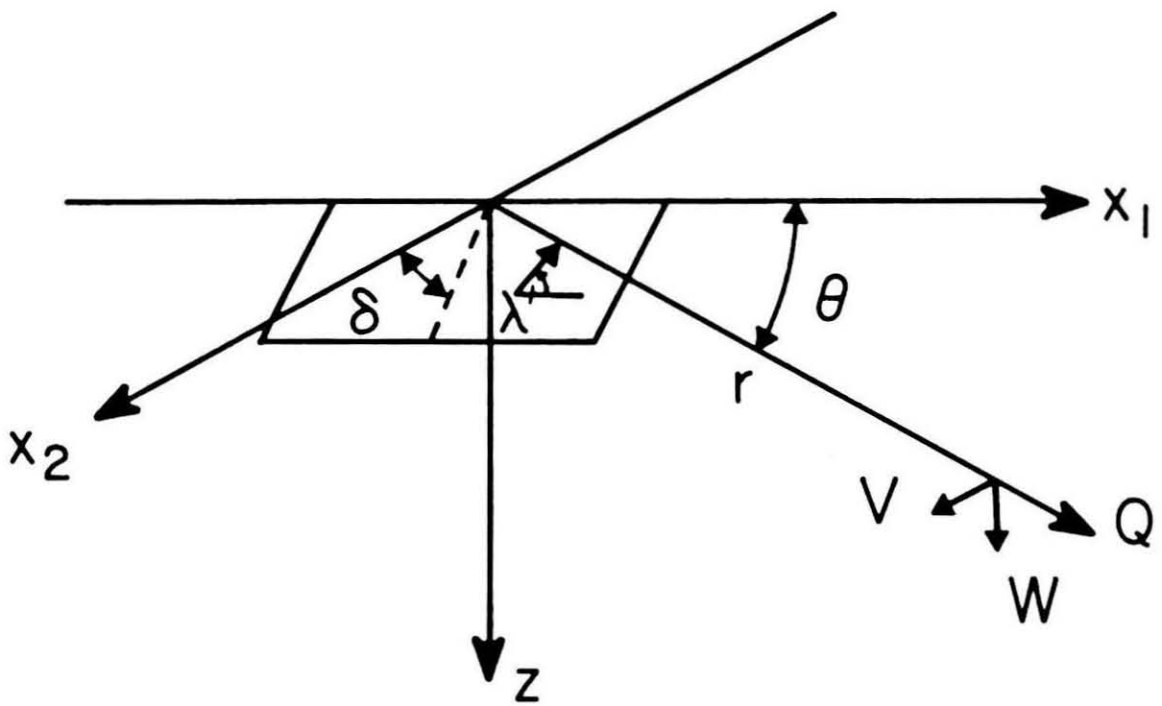


Figure 1.2 Description of conventions for mechanism and orientation.

Integrals of the type given in equations (12) through (14) can be transformed back into the time domain by applying the Cagniard-de Hoop technique. For example, suppose we consider the integral

$$\bar{\zeta}(r, z, s) = \frac{2}{\pi} s \operatorname{Im} \int_c^{i\infty + c} \frac{p}{\eta_\alpha} K_2(spr) e^{-s\eta_\alpha |z-h|} dp \quad (17)$$

that can be expressed as

$$\zeta(r, z, t) = \frac{2}{\pi} \frac{\partial}{\partial t} \operatorname{Im} \int_0^t \frac{c(t, \tau)}{\sqrt{(t-\tau)(t-\tau+2pr)}} \left(\frac{dp}{d\tau} \right) \frac{p(\tau)}{\eta_\alpha} d\tau, \quad (18)$$

where

$$c(t, \tau(p)) = \cosh \left\{ 2 \cosh^{-1} \left(\frac{t-\tau+pr}{pr} \right) \right\}$$

The various functions of p are to be evaluated along the Cagniard-de Hoop contour, namely

$$\tau(p) = pr + \eta_\alpha |z-h|$$

from the first arrival time R/α to t . The integral is computed numerically. This particular integral has a closed form solution,

$$\zeta(r, z, t) = \frac{d}{dt} \left[\frac{1}{R} + \frac{2\alpha}{r^2} \left(t - \frac{R}{\alpha} \right) \right] H \left(t - \frac{R}{\alpha} \right) \quad (19)$$

as discussed by Helmberger and Harkrider (1978).

Thus, one way to proceed is to substitute equations (12) through (14) into equation (11) and evaluate the integrals following the above scheme. This is the full Cagniard solution, and the results for a simple case are shown in the bottom row of seismograms in Figure 1.3.

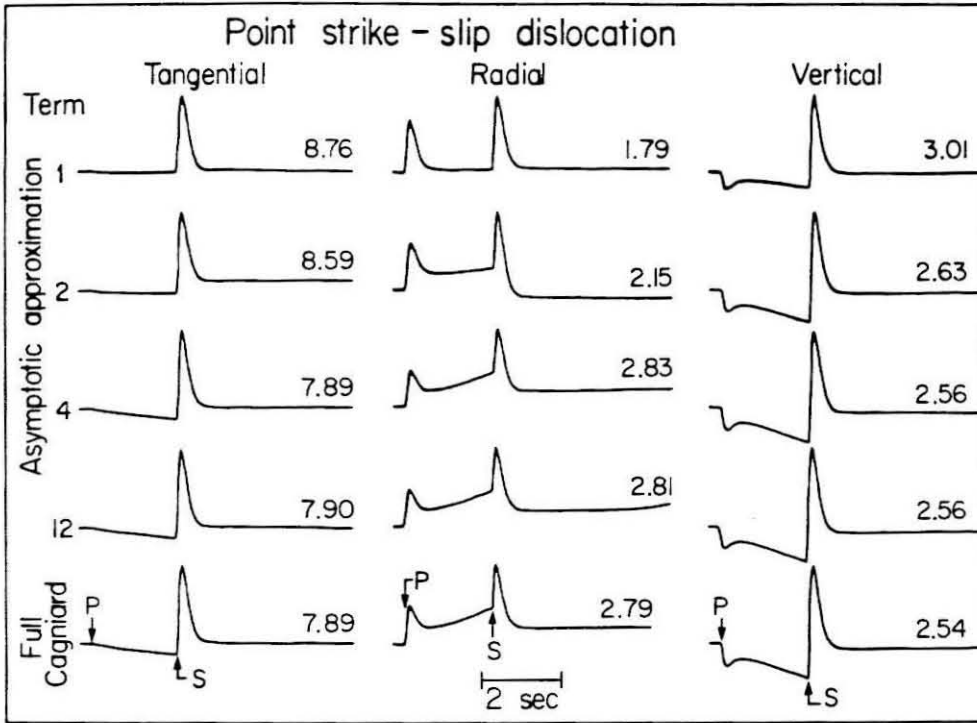


Figure 1.3 Comparison of the three components of displacement for a whole-space with a strike-slip source. The top four rows contain the asymptotic summation with 1, 2, 4, and 12 terms. The full solution is displayed on the bottom. The source depth is $h = 8$ km and the range is $r = 16$ km. Model parameters are $\alpha = 6.2$ km/sec, $\beta = 3.5$ km/sec, and $\rho = 2.7$ g/cm³.

A much faster procedure is to expand the modified Bessel functions of order n , K_n , as

$$K_n (spr) = \sqrt{\frac{\pi}{2spr}} e^{-spr} \left[1 + \frac{4n^2-1}{8spr} + \dots \right] \quad (20)$$

and substitute the potentials in equations (12), (13), and (14) into the displacement equation (11) and expand in powers of s^{-1} . The first term of such an expansion has the following form:

$$\mathbf{V}(r, z, t) = \frac{M_0}{4\pi\rho_0} \frac{d}{dt} \left[\dot{D}(t) * \sum_{j=1}^2 A_{j+3} (\theta, \lambda, \delta) v_j (r, z, t) \right] \quad (21)$$

$$\mathbf{W}(r, z, t) = \frac{M_0}{4\pi\rho_0} \frac{d}{dt} \left[\dot{D}(t) * \sum_{j=1}^3 A_j (\theta, \lambda, \delta) w_j (r, z, t) \right] \quad (22)$$

$$\mathbf{Q}(r, z, t) = \frac{M_0}{4\pi\rho_0} \frac{d}{dt} \left[\dot{D}(t) * \sum_{j=1}^3 A_j (\theta, \lambda, \delta) q_j (r, z, t) \right] \quad (23)$$

where

$$v_j = \sqrt{\frac{2}{r}} \frac{1}{\pi} \left[\frac{1}{\sqrt{t}} * \text{Im} \left[\frac{\sqrt{p}}{\eta_\beta} SH_j p \frac{dp}{dt} \right] \right] \quad (24)$$

$$(25)$$

$$w_j = \sqrt{\frac{2}{r}} \frac{1}{\pi} \left[\frac{1}{\sqrt{t}} * \text{Im} \left[\left(\frac{\sqrt{p}}{\eta_\alpha} C_j (-\epsilon \eta_\alpha) \frac{dp}{dt} \right)_\alpha + \left(\frac{\sqrt{p}}{\eta_\beta} SV_j p \frac{dp}{dt} \right)_\beta \right] \right]$$

$$(26)$$

$$q_j = \sqrt{\frac{2}{r}} \frac{1}{\pi} \left[\frac{1}{\sqrt{t}} * \text{Im} \left[\left(\frac{\sqrt{p}}{\eta_\alpha} C_j p \frac{dp}{dt} \right)_\alpha + \left(\frac{\sqrt{p}}{\eta_\beta} SV_j (-\epsilon \eta_\beta) \frac{dp}{dt} \right)_\beta \right] \right]$$

This is a first term asymptotic expansion similar to the expansion used for explosive sources in Section 1.2. The approximation is accurate for $spr \gg$

1, which means it is most accurate for high frequency, large range, and non-vertical take-off angle. The one arrival in v_j is the SH body-wave, and the two arrivals in w_j and q_j are the P and SV body-waves. Note that the first term solution becomes uncoupled in that \mathbf{V} depends only on χ ; and \mathbf{W} and \mathbf{Q} only on ϕ and Ω , so the SH solution separates from the P-SV solution in this asymptotic form.

Note that the term

$$V_j = \text{Im} \left(SH_j \frac{p}{\eta_\beta} \frac{dp}{dt} \right) \quad (27)$$

in equation (24) and the analogous terms in equations (25) and (26) are solutions to the two-dimensional (line source) elastic wave equation. This suggests a scheme whereby sources with a radiation pattern may be introduced into a 2-D numerical grid. For a source located in a homogeneous region we have:

$$p = \frac{r}{R^2} t + i \left(t^2 - \frac{R^2}{V^2} \right)^{1/2} \frac{|z - h|}{R^2} \quad (28)$$

$$\eta_V = \frac{|z - h|}{R^2} t - i \left(t^2 - \frac{R^2}{V^2} \right)^{1/2} \frac{r}{R^2}$$

and

$$\text{Im} \left(SH_j \frac{p}{\eta_\beta} \frac{dp}{dt} \right) = \text{Re} (SH_j p) \frac{H(t - R/\beta)}{(t^2 - R^2/\beta^2)^{1/2}}. \quad (29)$$

Similar expressions may be derived from equations (25) and (26). The effective line source radiation patterns can be obtained by evaluating the various Re operators.

It is only a matter of algebra to find the explicit functions which may be used to drive the source box in the FD grid. These functions are given below. The source box mechanics are described below in Section 1.4.

SH case

The following solutions are for a whole-space. Let

$$\Gamma_\gamma = \sqrt{\frac{2}{\gamma}} \frac{1}{4 \pi^2 \rho 10^{20}}$$

$$T_\gamma = \frac{R^2}{t^2 \gamma^2}$$

where $\gamma = \alpha$ or β . The analytic source expressions at the edges of the source box are

$$V_4 = \frac{\Gamma_\beta}{\beta^2} \frac{\sin i}{R \sqrt{1 - T_\beta}} H\left(t - \frac{R}{\beta}\right) * \frac{d M_o(t)}{dt} \quad (30a)$$

$$V_5 = \frac{\Gamma_\beta}{\beta^2} \frac{\cos i}{R \sqrt{1 - T_\beta}} H\left(t - \frac{R}{\beta}\right) * \frac{d M_o(t)}{dt} \quad (30b)$$

where V_4 and V_5 represent the strike-slip and dip-slip cases, respectively. The $*$ represents convolution. H is the Heaviside step function, ρ , β , and α (used below) are the density, shear wave and compressional wave velocity at the source, $M_o(t)$ is the moment release as a function of time, R is the source-to-receiver distance, and i is the angle between the vertical and the line connecting the source and receiver, as shown in Figure 1.1. Convolution with a smooth enough time function $M_o(t)$ avoids problems with the singular pulse of energy at the geometrical arrival time.

After the energy propagates across laterally and vertically heterogeneous structure, "line source seismograms" \tilde{V}_i may be extracted from the grid. Note the difference between V and \tilde{V} . V are the whole-space solutions inserted in the source region of the FD grid. \tilde{V} are the seismograms which are extracted from the FD grid. The point source seismograms are obtained by

$$\mathbf{V}_p = \frac{1}{\sqrt{R}} \frac{d}{dt} \left(\frac{1}{\sqrt{t}} * (A_4 \tilde{V}_4 + A_5 \tilde{V}_5) \right) \quad (31)$$

where \mathbf{V}_p is the SH displacement in cm when moment is in dyne-cm, density is in g/cm^3 , β is in km/sec, and R is in km.

P-SV case

For convenience, we define:

$$\Phi_\gamma = \Gamma_\gamma \frac{t^2}{R^6 \sqrt{1 - T_\gamma}} H\left(t - \frac{R}{\gamma}\right) * \frac{d M_o(t)}{dt}$$

where $\gamma = \alpha$ or β . Next, we present the results for the three fundamental faults: the strike-slip, the dip-slip, and the 45° dip-slip cases.

Strike-slip case

(32)

$$Q_1 = r \left(\Phi_\alpha (r^2 - 3z^2 + 3 T_\alpha z^2) + \Phi_\beta (3z^2 - r^2 + T_\beta (r^2 - 2z^2)) \right)$$

$$W_1 = z \left(\Phi_\alpha (z^2 - 3r^2 + T_\alpha (2r^2 - z^2)) + \Phi_\beta (3r^2 - z^2 + T_\beta (z^2 - 2r^2)) \right)$$

Dip-slip case

(33)

$$Q_2 = z(\Phi_\alpha (6r^2 - 2z^2 + T_\alpha (2z^2 - 4r^2)) + \Phi_\beta (2z^2 - 6r^2 + T_\beta (5r^2 - z^2)))$$

$$W_2 = r(\Phi_\alpha (2r^2 - 6z^2 + T_\alpha (4z^2 - 2r^2)) + \Phi_\beta ((6z^2 - 2r^2 + T_\beta (r^2 - 5z^2))))$$

45° dip-slip case

(34)

$$Q_3 = r(\Phi_\alpha (9z^2 - 3r^2 + T_\alpha (2r^2 - 7z^2)) + \Phi_\beta ((3r^2 - 9z^2 + T_\beta (6z^2 - 3r^2))))$$

$$W_3 = z(\Phi_\alpha (9r^2 - 3z^2 + T_\alpha (z^2 - 8r^2)) + \Phi_\beta ((3z^2 - 9r^2 + T_\beta (6r^2 - 3z^2))))$$

where r is the horizontal component of R , and is positive in the direction of the receiver, and z is the vertical component of R , and is positive downward.

As in the SH case, the line source seismograms extracted from the FD grid, \tilde{Q}_i and \tilde{W}_i , are transformed into point seismograms by:

$$\mathbf{Q}_p = \frac{1}{\sqrt{R}} \frac{d}{dt} \left(\frac{1}{\sqrt{t}} * (A_1 \tilde{Q}_1 + A_2 \tilde{Q}_2 + A_3 \tilde{Q}_3) \right) \quad (35)$$

$$\mathbf{W}_p = \frac{1}{\sqrt{R}} \frac{d}{dt} \left(\frac{1}{\sqrt{t}} * (A_1 \tilde{W}_1 + A_2 \tilde{W}_2 + A_3 \tilde{W}_3) \right) \quad (36)$$

Again, \mathbf{Q}_p and \mathbf{W}_p are horizontal and vertical displacements in cm.

1.4 Algorithm for coupling expressions with numerical scheme

Energy is introduced into the FD grid with the type of source region described by Alterman and Karal (1968). The use of a source region rather than a source point is necessary to avoid singular points such as at the source of an explosion in the displacement field. The fourth-order FD calculations do poorly for propagating energy with wavelengths shorter than 10 grid points per wavelength (Alford et al., 1974), and such energy is abundant near singular points. In each timestep, the FD algorithm uses the present and past timesteps to compute a future timestep, which is written over the past timestep. During each timestep, energy insertion is a two-stage process. The first stage is to add in the energy that is coming out of the source. The second stage is to remove direct energy from the source and follow the indirect energy which is traveling through the source region. If the displacements computed analytically were simply imposed on the source box, the source area would act as a rigid reflector for energy impinging on the area from the outside. The rigid reflector source box noticeably affects the results of the FD modeling, particularly if the source is near the free surface (Alterman and Karal, 1968).

These two stages are done by the following procedure, which will be outlined for a second-order algorithm. The FD results in this paper are constructed with a fourth-order source insertion algorithm, which only differs from the algorithm described below in that rings 2 and 3 each contain 2 rings of grid points and the grid is updated by a fourth-order FD scheme. The advantages of the fourth-order FD schemes are discussed in Alford et al. (1974).

The FD grid is divided into 1) an exterior, 2) an outer ring of grid points, 3) an inner ring of grid points, and 4) an interior (see Figure 1.4). The source is in the center of region 4, the interior, which never sees the direct waves from the source.

- A. Region 4 from the past timestep is saved in an array.
- B. The entire grid is updated to the future timestep by the FD algorithm.
- C. The outer ring, region 2 in the future timestep is saved in an array for later reinsertion.
- D. Rings 2 and 3 for the past timestep are loaded into the source region grid with displacements that have had the source subtracted, and region 4 is loaded with the past time step that was saved above in step A.
- E. The grid for ring 3 and region 4 is again updated to the future timestep by the FD algorithm.
- F. The analytic source values at the grid points in rings 2 and 3 for the present timestep are read into arrays.
- G. The source-free ring 3 from the present timestep is saved for use in step D in the next timestep, and the analytic source is added to ring 3. The ring 2, which includes the source, is saved in an array, and the analytic source is

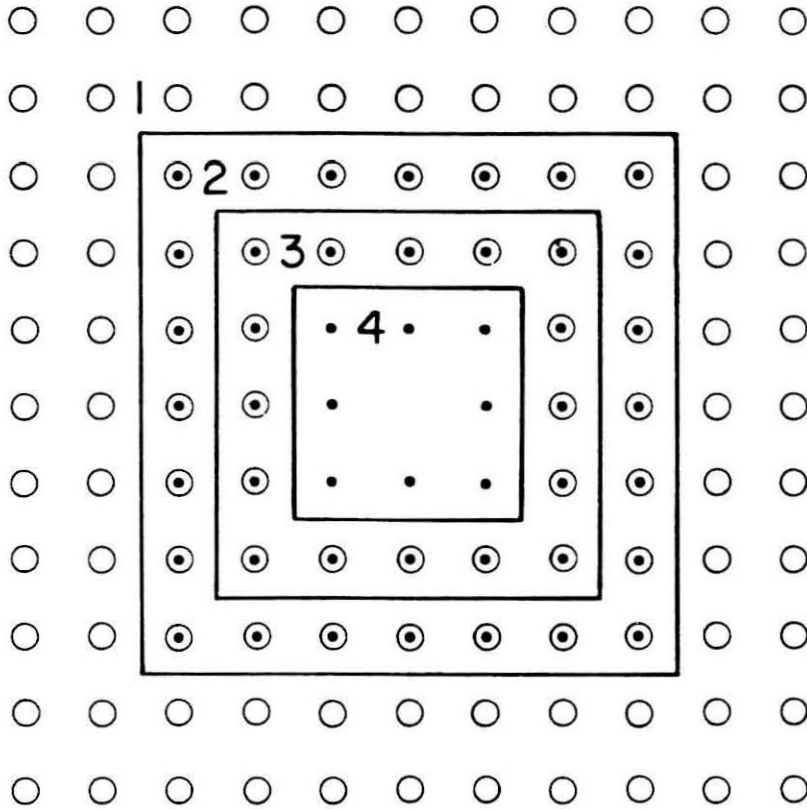


Figure 1.4 Source region geometry. Region 1 is outside rings 2 and 3, which are each 1 grid point thick. Region 4 is inside rings 2 and 3. The source is in the center of region 4. Region 1 is only computed with the source included, and region 4 is computed only without the source. Rings 2 and 3 are computed both with and without the source. The geometry for a fourth- rather than second-order FD scheme would use rings 2 and 3 which are 2 rather than 1 grid point thick.

subtracted from the array, which will also be used in step D in the next timestep.

H. Ring 2 is reloaded with the array stored in step C, so region 1, and rings 2 and 3 all contain the source.

I. All the past values at the grid points are now overwritten by the future values. The grid is advanced one timestep by making the array of present values into past values and the future values into the present values. The present arrays saved for rings 2 and 3 become the past arrays that are needed for the next timestep.

Since this process requires the analytic form of the displacement at many points in space and time, we use a homogeneous source region. This allows the use of whole-space solutions for the analytic functions. The use of even simple half-space solutions, which would allow a source closer to the free surface since the free surface could be within the source region, would lengthen the time required to compute the analytic source functions to more than the time the FD code takes to run.

1.5 Illustration of various sources

We will next show the SH and P-SV sources as a function of space at a fixed point in time to gain some insight as to how they work. The time function used to excite the grid is a Heaviside step function smoothed by

convolution with the function e^{-Kt^2} , where t is time. The smoothing operator is necessary because the FD method does not treat the highest frequencies correctly. Most FD researchers, however, convolve by te^{-Kt^2} , or, equivalently, use a spatial function like e^{-Kr^2} to start up the FD grid, where r is the distance to the source. That operation eliminates the low-frequency as well as the high-frequency ends of the source power spectrum. Without the low frequencies in the source, the $1/\sqrt{t}$ amplitude decay that characterizes line sources is not as apparent. We chose to use the e^{-Kt^2} source, which keeps the $1/\sqrt{t}$ tails and the low frequencies in the FD grid, but then we eliminate the tails without losing the low-frequency energy with the line-to-point source conversion described by equations (31), (35), and (36).

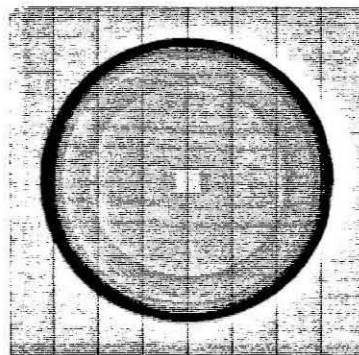
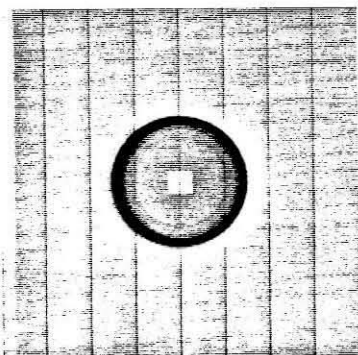
The whole-space source functions for the SH case are shown in timeslices in Figure 1.5. The explosive case is isotropic, and the strike-slip and dip-slip cases have $\sin \theta$ and $\cos \theta$ vertical radiation patterns respectively, where θ is the takeoff angle. The explosion is physical only in the acoustic problem, which obeys the same equation as the SH case with a uniform whole-space. The traveling energy in this and the two following figures, which has propagated nearly to the edge of the grid from the source by the second timeslice, has the character of a line source. The seismograms show an amplitude decay in space of $1/\sqrt{r}$ and have an impulsive arrival followed by a $1/\sqrt{t}$ amplitude decay in time. The "pseudo-near field", which is the energy seen in Figure 1.5 in the region of the source, becomes a static field with time. Note the square devoid of displacement in the center of the source region. This is region (4), the interior of the source, which never sees the direct waves.

SH VERTICAL RADIATION PATTERNS

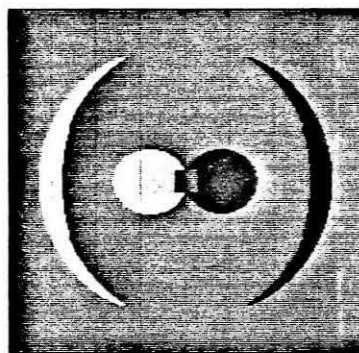
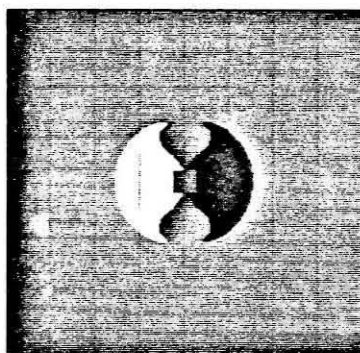
t = 125 time steps

t = 250 time steps

Explosion



Strike-Slip



Dip-Slip

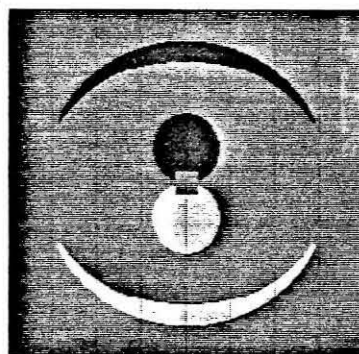
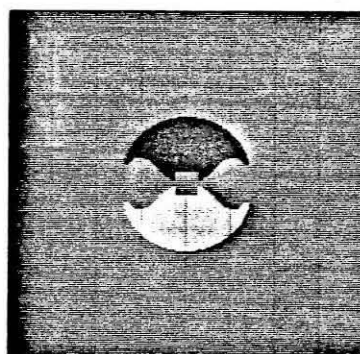


Figure 1.5 SH vertical radiation patterns. The displacement field due to explosive, strike-slip, and dip-slip sources are shown after 125 and 250 timesteps. The explosive plots have a white background, and all displacements are positive, while the plots for the earthquakes have a grey background, where positive displacements are shown in black and negative in white.

The whole-space source functions for the P-SV case are shown in timeslices in Figure 1.6. The divergence and curl of the displacements that are calculated in the FD grid are shown for the explosive, strike-slip, dip-slip, and 45° dip-slip cases. The divergence is nonzero where there is compressional wave energy and the curl is nonzero for shear wave energy. The divergence and curl are first spatial derivatives and so raise the frequency content slightly over that of the displacements themselves. The elastic explosion has an isotropic, compressional radiation pattern. The timeslice of the curl for the explosion would show only scaled-up noise which is much smaller than the energy in the divergence timeslice. The explosion is similar to the SH earthquake source in that it has a permanently displaced "pseudo-near field".

The P-SV far-field radiation patterns are the usual ones for the explosive, strike-slip, dip-slip, and 45° dip-slip cases. For example, in the strike-slip case, the P-waves show a 2-lobed pattern in the divergence, and the S-waves a 4-lobed pattern in the curl of the displacements. Figure 1.7 shows the divergence of the strike-slip case on a larger scale. The patterns of energy distribution needed to maintain the correct far-field radiation are complex. The "pseudo-near field" energy may be seen as the inner clover-leaf patterns. The clover-leaf patterns are followed by more near-field energy in 12-lobed patterns. Again, the inner region of the source area is visible by its lack of disturbance, and the edge of the inner region is visible from the divergences and curls that arise from the truncation of the displacement around the inner region. These "pseudo-near field" terms grow with time and cause the synthetic seismograms to become inaccurate after some time. These terms are more long-period than the earlier energy. For these reasons, the P-SV

P-SV VERTICAL RADIATION PATTERNS

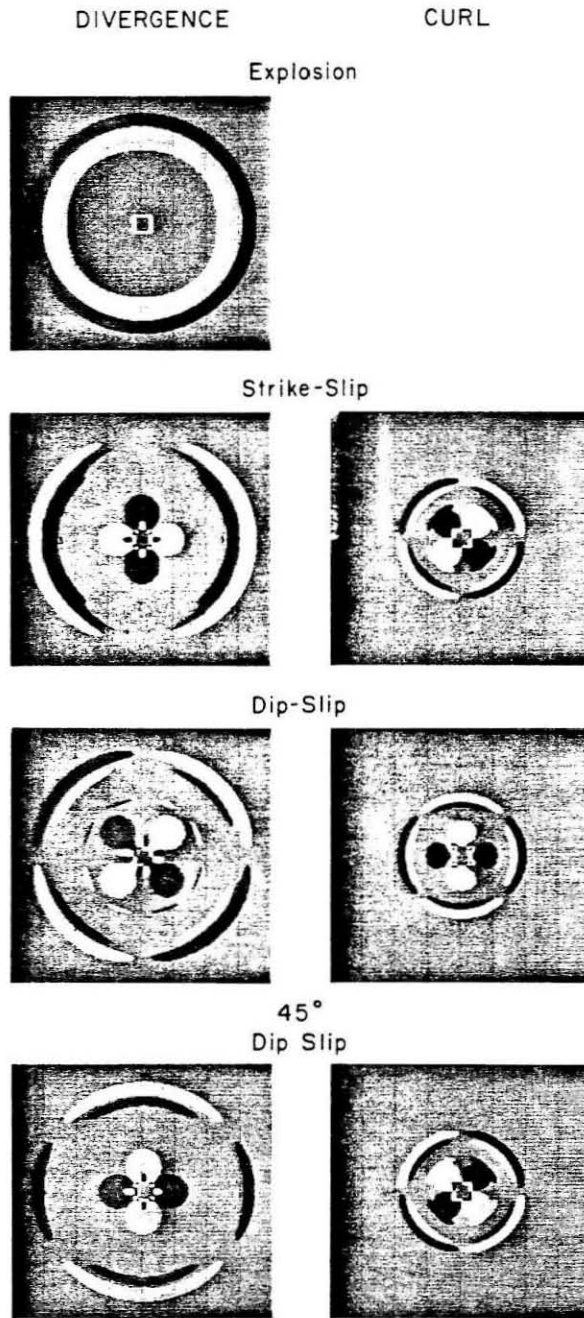


Figure 1.6 P-SV vertical radiation patterns. The divergence and curl fields due to explosive, strike-slip, dip-slip, and 45° dip-slip sources are shown after 150 timesteps. The plots have a grey background, where positive is shown in black and negative in white.

P-Wave Portion Of Strike-Slip Pattern

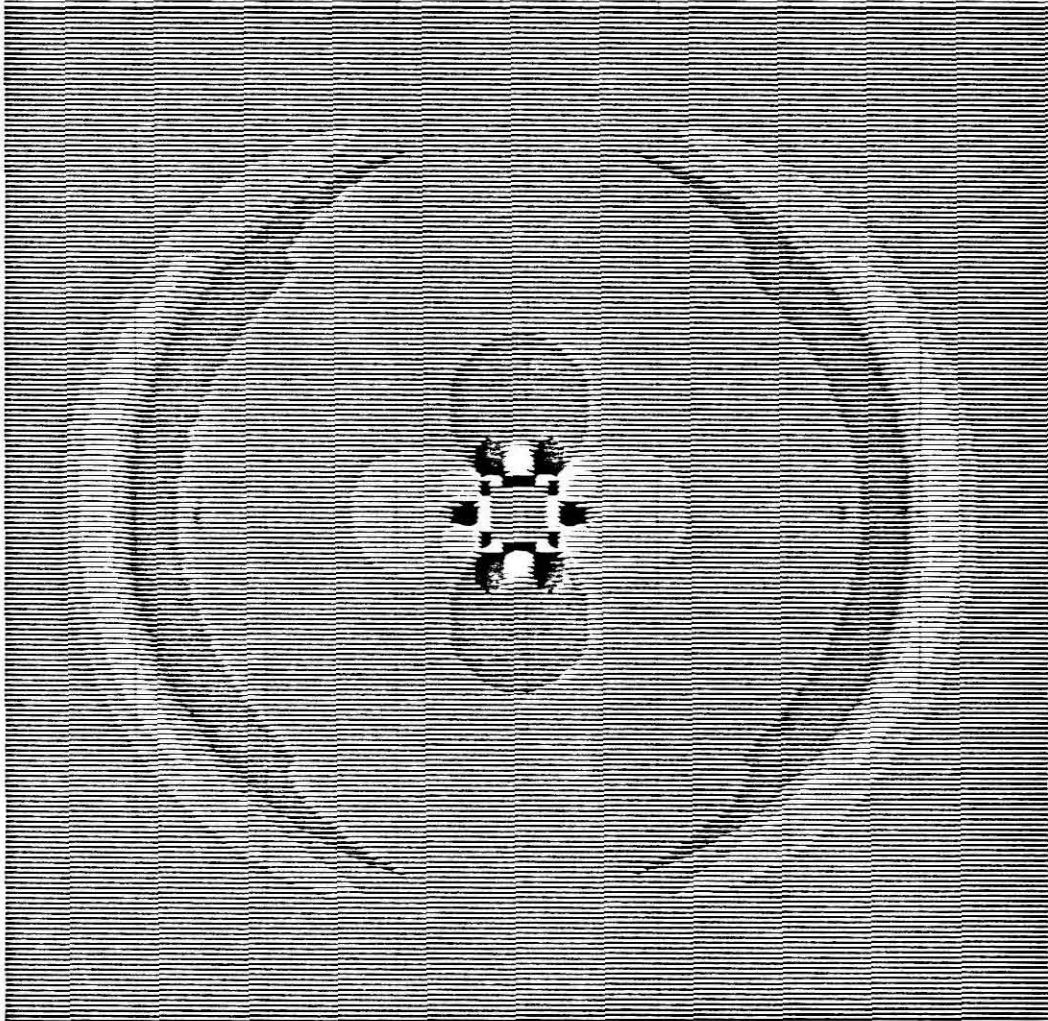


Figure 1.7 Strike-slip divergence (P-wave) vertical radiation pattern. The far-field, and two "pseudo-near field" patterns may be seen. The far-field has the familiar two lobes, the outer near-field has four lobes and the innermost near-field has twelve lobes. The near-field terms are necessary to maintain the correct far-field radiation pattern.

earthquake sources are most accurate at both earlier time and shorter period, up the short-period limit of the FD grid. The explosive P-SV source and the SH earthquake sources have "pseudo-near fields" which result in static displacements, that is, the near-fields do not grow with time, so they do not become less accurate at longer times. The limitations arise from the asymptotic approximation shown in equation (20).

The optimal choice of source box size depends on whether the source is explosive or double-couple and whether the calculation is P-SV or SH. The source box introduces energy into the FD grid far enough from the source to ensure that the displacements are sufficiently smooth. Smaller source boxes, however, are better in that they allow structure nearer the source and they require less computation. Elastic earthquake sources are more demanding in the sense that there is more amplitude variation along the source rings than elastic explosive sources, which are in turn about as demanding as SH earthquake sources, which are more demanding than acoustic explosive sources. Elastic earthquakes therefore require the largest source boxes and acoustic explosions can be inserted with the smallest source boxes.

1.6 Tests of accuracy

Several approximations must be examined. First, the GRT expansion of the solution to a finite set of generalized rays may be validated. Next, the error in only using the first term of the asymptotic series expansion of the Bessel functions must be justified. Finally, the result of using the 2-D FD grid

to propagate the energy from source to receiver may be tested.

The extension to higher order terms is simple using the analytical Cagniard-de Hoop expressions since they depend mostly on the temporal integrals of the previous terms. The results of such an expansion is shown above in Figure 1.3. When the responses are convolved with most instruments, the higher order corrections make little difference because they are more long-period. Thus, we will limit our discussion to the first term of the asymptotic expansion for the rest of this work.

The FD code that solves the SH equation is compared with the flat-layer GRT code that has been well tested (c.f. Apsel and Luco, 1983) for a model with one layer over a half-space that represents simple oceanic lithosphere. The geometry and media parameters are shown in Figure 1.8.

Receivers for the plots in Figures 1.9 through 1.12 are positioned on the surface at lateral distances of 40 to 760 km from the source. These plots are reduced by a 4.8 km/sec velocity.

Figure 1.9 contains synthetic seismograms for the line source problem with symmetric source. The results from the GRT code (Figure 1.9a) and the results from the FD code (Figure 1.9b) are in excellent agreement.

Amplitudes differ between the two sets of synthetics by no more than 3% and the detailed waveforms are nearly identical. Even the highest frequencies shown agree well for the first portion of each seismogram. The later portion of the seismograms shows some contamination by dispersed high-frequency energy. The discrepancies between the traces are high frequency and small.

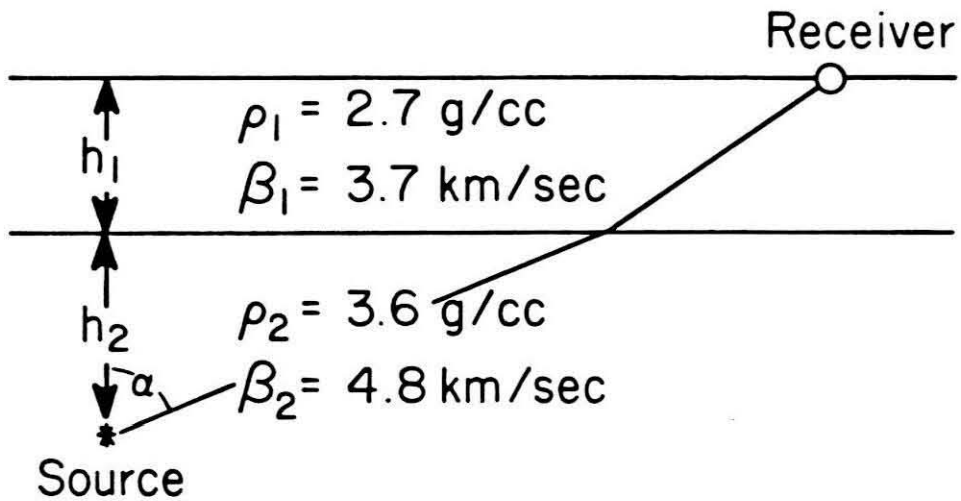


Figure 1.8 Flat layer over a half-space geometry with shear wave velocities and densities. The crust has h_1 of 9 km with a density ρ_1 of 2.7 g/cm^3 and a shear wave velocity β_1 of 3.7 km/sec, and the underlying upper mantle has ρ_2 of 3.6 g/cm^3 and β_2 of 4.8 km/sec. The source is placed 18 km below the surface, or h_2 is 9 km.

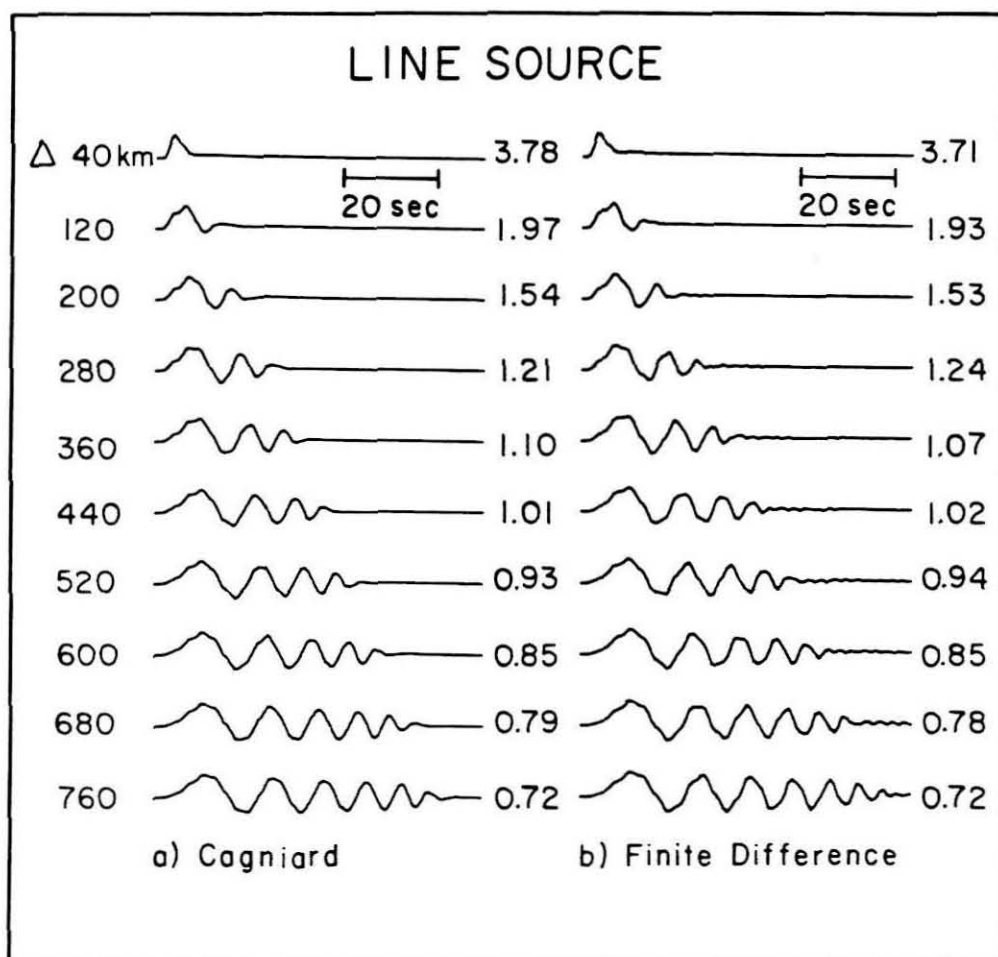


Figure 1.9 Comparison of the line source synthetic seismograms generated by the Cagniard and FD methods. Results are for the geometry shown in Figure 1.8. The source is 9 km below the layer and the receivers are on the surface and range from 40 to 760 km in horizontal distance from the source. Both sets of seismograms are convolved with a trapezoidal time function. The amplitudes are absolute.

The point source synthetics fare nearly as well. The synthetics are convolved with the long-period WWSSN instrument response. The shortest and longest period energy is attenuated in transforming the line source seismograms to the point source seismograms and including the instrument response. The traces generated by the point-source, flat-layer GRT program (Figure 1.10a) and those obtained by the transformation of the FD seismograms (Figure 1.10b) are in close agreement. The waveform agreement is excellent. The amplitudes agree to within 20% in all cases.

The next question is whether the FD seismograms with sine and cosine vertical radiation patterns agree with their GRT equivalents. Figure 1.11 shows traces for the $\cos \theta$ radiation pattern, and Figure 1.12 shows traces for the $\sin \theta$ radiation pattern. The agreement in waveform is good, and again the amplitudes agree to within 20% for all but the nearest offsets.

Some disagreement is expected for near vertical takeoff angles because of a slight difference in geometrical spreading between the 2-D and 3-D geometries. For 3-D spreading, there should be an additional factor of $\sqrt{\sin \alpha}$ in the vertical radiation pattern. This factor can be seen, for example, as an additional \sqrt{p} for the point source that is not in the line source on p. 181 of Helmberger (1983). We are not able to simulate the additional factor of $\sqrt{\sin \alpha}$ because the expression is singular at α of 0° and 180° , which introduces numerical problems. However, we are generally not interested in vertical paths since they may be handled by other methods, see Scott and Helmberger (1983), for example.

The P-SV elastic case is more complicated than the SH case due to the possible mode changes at each boundary, and the accuracy of both the GRT

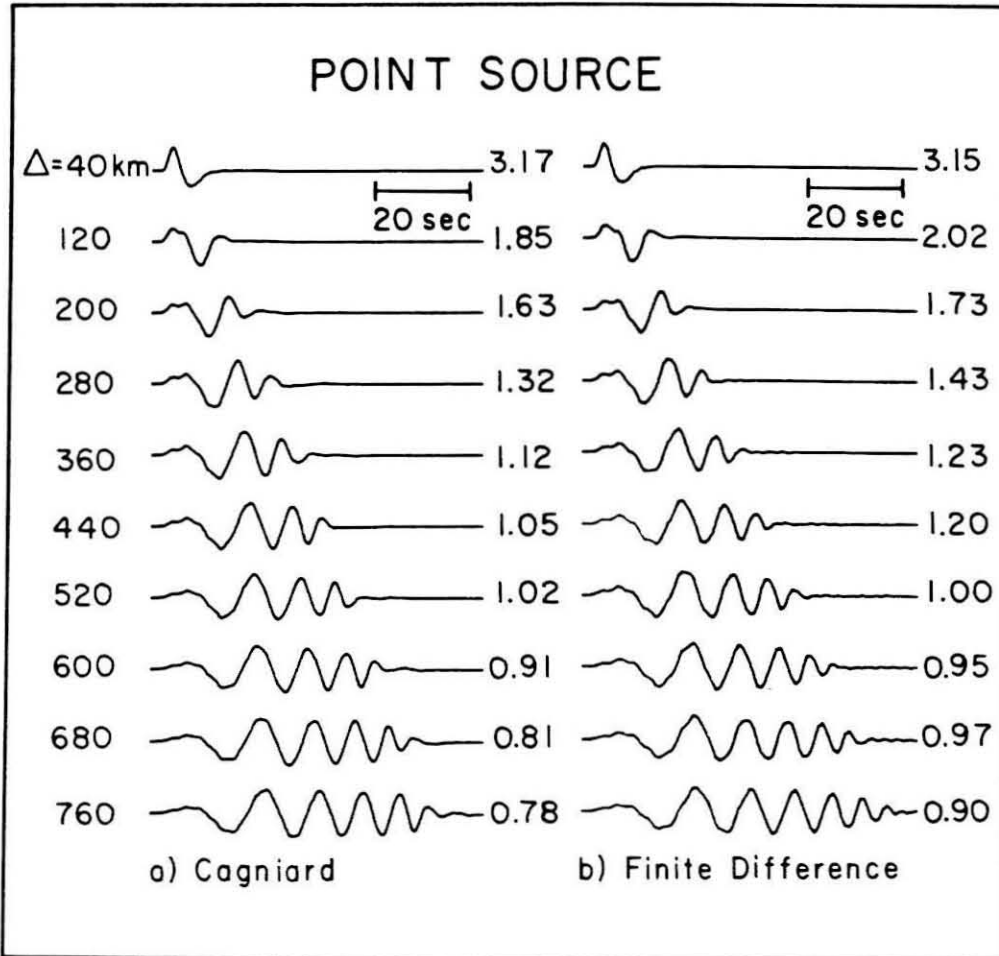


Figure 1.10 Comparison of the point source synthetic seismograms generated by the GRT and FD methods for the flat-layer geometry shown in Figure 1.8. Amplitudes are absolute and may be scaled to moment.

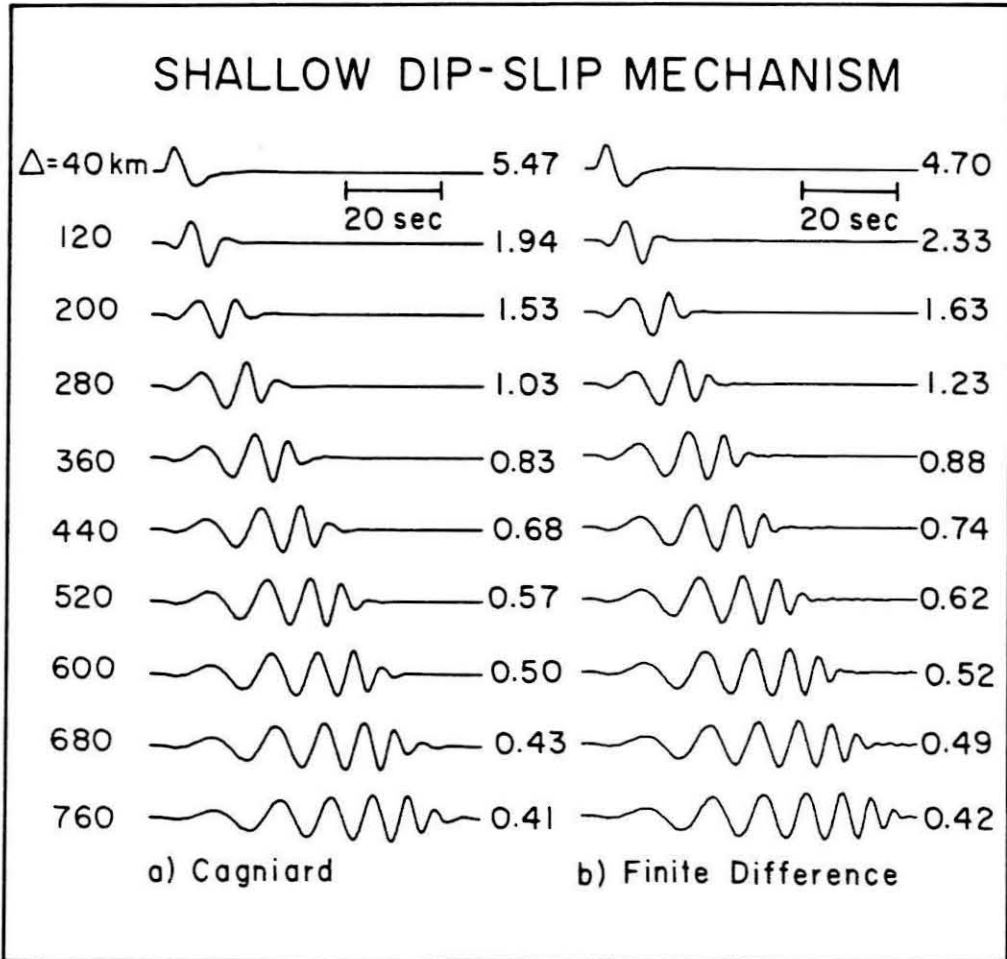


Figure 1.11 Comparison of the point source $\cos \theta$ mechanism synthetic seismograms generated by the GRT and FD methods for the flat-layer geometry shown in Figure 1.8.

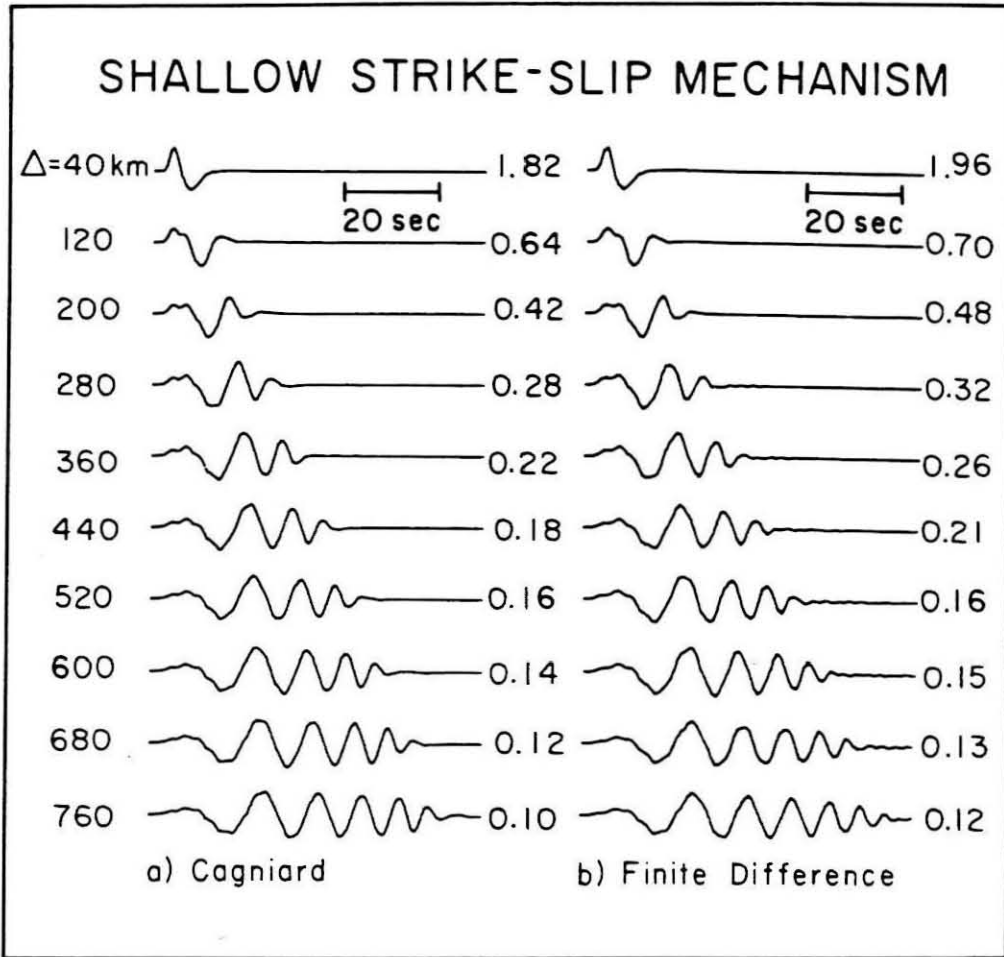


Figure 1.12 Comparison of the point source $\sin \theta$ mechanism synthetic seismograms generated by the GRT and FD methods for the flat-layer geometry shown in Figure 1.8.

and FD methods must be checked against more complete solutions. The GRT calculations for a simple layer over a half-space case described in Table 1.1 are shown as the dotted lines in Figure 1.13. These results are compared with a more exact wave-number integration solution, shown as the solid lines in Figure 1.13 (see Apsel and Luco, 1983). A comparison between the GRT results and the computationally slower, but more general FD procedure is given in Figure 1.14, where the results for all three fundamental faults are shown. The methods agree very well.

Adding layers to the model greatly complicates the GR approach especially for the latter portion of the record when many ray paths are involved. On the other hand, the FD procedure described below remains unaffected by such complexity and is well suited for exploring the effects of any lateral variations.

The explosive source is checked in Chapters 1.7 and 3.2 against several other methods.

1.7 Limitations and a more accurate explosive source

The equations for 2-D and 3-D wave propagation are similar, but there are important differences. We will examine the acoustic case, although the same arguments hold for the elastic case. In the acoustic case, the 2-D wave equation for homogeneous media is

$$P_{tt} = c^2 (P_{xx} + P_{zz}), \quad (37)$$

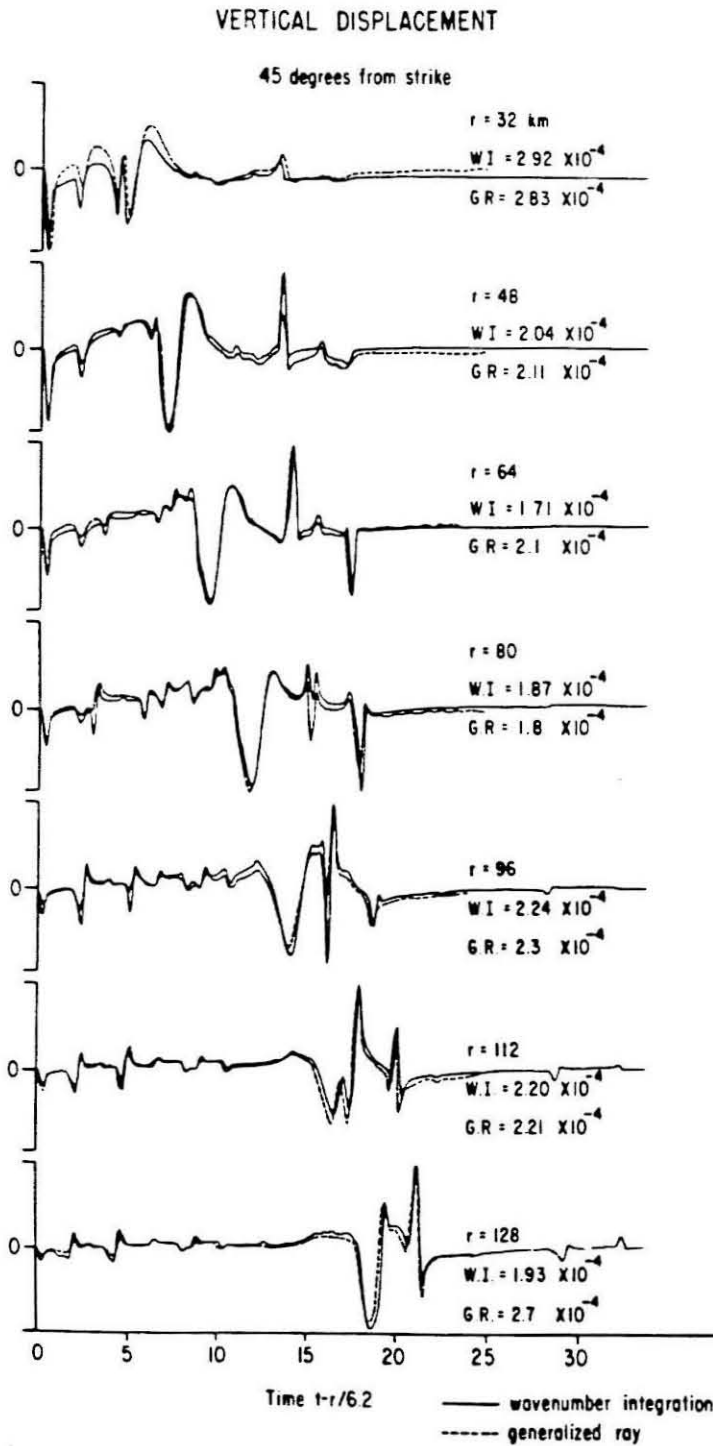


Figure 1.13 Comparison of the wavenumber integration solution with the GRT first term asymptotic solution for vertical displacement on the free surface due to a vertical strike-slip dislocation buried at a depth of 8 km in the model described in Table 1.1 (after Apsel and Luco, 1983).

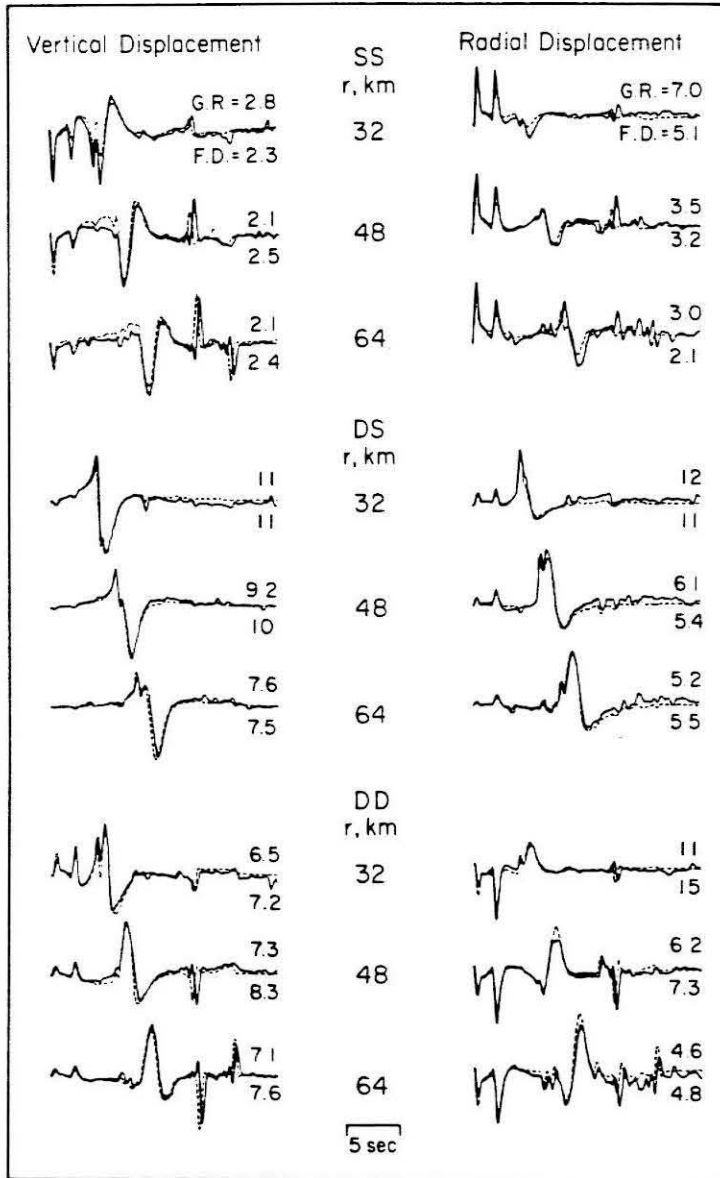


Figure 1.14 Comparison of FD and GRT seismograms for the model described in Table 1.1 for the ranges 32, 48, and 64 km for the strike-slip, dip-slip, and 45° dip-slip mechanisms. The far-field source time function, $D(t)$, is specified by a trapezoidal shape with equal δt_j 's of 0.2 seconds. Amplitudes may be scaled to moment.

Table 1.1 : Layer over half-space model

P-wave velocity (km/sec)	S-wave velocity (km/sec)	density g/cm ³	layer thickness km
6.2	3.5	2.7	32.0
8.2	4.5	3.4	∞

where P is pressure, c is the wave velocity, x and z are cartesian coordinates, and subscripts indicate derivatives. The 3-D acoustic wave equation for homogeneous media is

$$P_{tt} = c^2 (P_{xx} + P_{yy} + P_{zz}), \quad (38)$$

where y is the third cartesian coordinate. Cylindrical co-ordinates, however, are generally more appropriate for wave propagation problems. In cylindrical coordinates

$$P_{tt} = c^2 (P_{rr} + P_{zz} + \frac{P_r}{r}), \quad (39)$$

where r and z are the radial and vertical coordinates, and azimuthal symmetry in the wavefield is assumed. The term that is multiplied by $1/r$ becomes negligible as r becomes large, and in this case the equations (37) and (39) are nearly equivalent.

There are several differences between waves propagating according to equations (37) and (39). In 2-D, wave amplitude decays with geometrical spreading by $1/\sqrt{R}$, where $R = \sqrt{x^2 + z^2}$, but in 3-D, wave amplitude decays by $1/R$, where $R = \sqrt{x^2 + r^2}$. This difference can be corrected by multiplying the amplitude of seismograms produced with equation (37) by $1/\sqrt{R}$, but this correction is exact only for a homogeneous media; if the actual raypath is bent by velocity gradients, or if several raypaths connect the source and receiver, the appropriate R may be ambiguous or may be difficult to find.

In 2-D, an impulsive burst of energy at the source results in an impulsive burst of energy at the receiver followed by a "line source tail" which decays as

$1/\sqrt{t}$, where t is the time after the first arrival of energy at the receiver. In 3-D, an impulsive burst of energy at the source results in an impulsive burst of energy at the receiver. The arrivals with a line source tail that result from the use of a 2-D numerical grid can be restored to point-source-like impulsiveness by convolution with the time series $H(t)/\sqrt{t}$, followed by a derivative with respect to time. Here $H(t)$ is the Heaviside step function. The seismograms produced are approximately those that would result from a source on the axis of symmetry in a cylindrically symmetric medium.

The corrections above have been described in Chapters 1.2 and 1.3, but here another correction term is introduced to approximate the anisotropy in geometrical spreading that better simulates 3-D wave propagation in a 2-D numerical grid.

The amount of energy leaving the source region at an angle i with the vertical in the 2-D grid may be approximated by the amount of energy in the point source case multiplied by $\sqrt{\sin i}$. The additional $\sqrt{\sin i}$ in the point source or three-dimensional solution can be explained in terms of geometrical spreading as is shown in Figures 1.15a and 1.15b. The energy with takeoff angle i between i_0 and $i_0 + di_0$ for the point source becomes

$$E_P = \frac{(2\pi \sin i_0 r) r di_0}{2\pi r^2} \quad (40)$$

or

$$E_P = \sin i_0 di_0$$

while for the line-source

$$E_L = \frac{r di_0}{2\pi r}$$

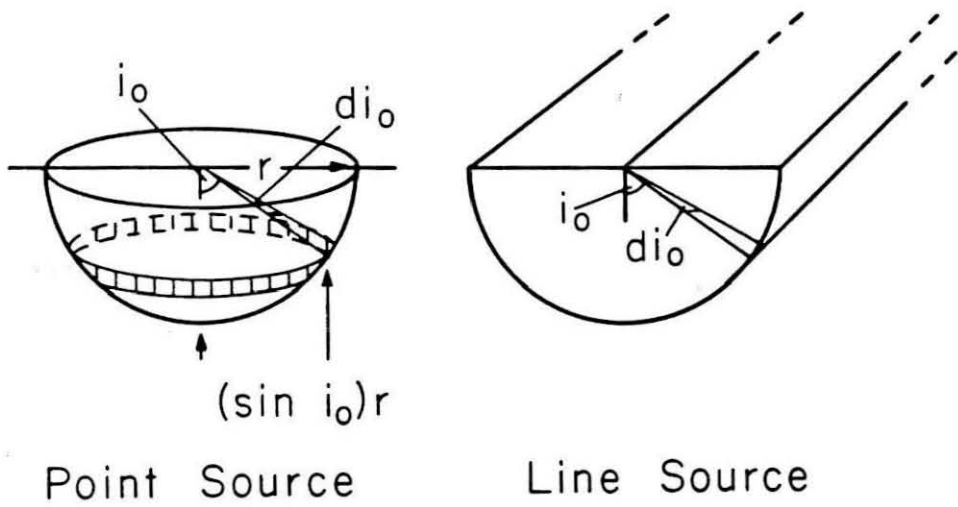


Figure 1.15 (a) Diagram showing energy with takeoff angle i in the range $i_0 < i < i_0 + di$ for point source. (b) Diagram showing energy with takeoff angle i in the range $i_0 < i < i_0 + di$ for line source.

or

$$E_L = di_0 \tag{41}$$

Since energy is proportional to the square of the amplitude we obtain the $\sqrt{\sin i}$ dependence.

If we use an isotropic explosion as the source in the 2-D grid, each arrival in a record may have a different take-off angle i , but we can only correct for a constant $\sqrt{\sin i}$. The result is that the vertically traveling energy is emphasized over horizontally traveling energy in the line source compared to the point source case.

One might ask, why not simply multiply the isotropic source by $\sqrt{\sin i}$? Such a source does not satisfy the 2-D elastic wave equation, unfortunately, and will not maintain the $\sqrt{\sin i}$ radiation pattern once the energy leaves the source region, primarily because the cusp in the $\sqrt{\sin i}$ at $i = 0^\circ$ does not satisfy the 2-D elastic wave equation.

The source functions we have found which are solutions to the 2-D elastic wave equation have radiation patterns of $\sin^n i \cos^m i$, where we may choose n and m . An isotropic line source explosion, for example, is the solution with $n = m = 0$, and the dislocation sources have $n + m = 2$, as described in Chapters 1.2 and 1.3. Also, because of the asymptotic nature of our solutions, the compressional and shear parts of the source separate. The correction we introduce is to add the compressional component of the horizontally-directed force term ($n = 1$ and $m = 0$) to the isotropic explosive source. This correction decreases the amplitude of energy leaving the source vertically, but leaves unchanged the amplitude of energy going horizontally out the side.

These two terms can be thought of as the first two term of a Taylor series expansion of $\sqrt{\sin i}$ about the point $i = 90^\circ$. Higher order corrections could be added, but we choose not to for the following reasons. The first two terms provide an accurate solution and whenever n or m is increased by 1 the "pseudo-near-field" terms in the solution grow more prominent by a factor of t , that is, the asymptotic solution diverges by another factor of t . In other words, an isotropic line-source explosion has a constant pseudo-near-field term, which is analogous to an explosion in a 3-D medium, where there may be some permanent deformation near the source. The compressional component of force described below grows with time as t , and slip dislocation sources given in Chapter 1.3 grow with time as t^2 . The addition of higher-order terms in the Taylor series would make the source radiation pattern more closely resemble $\sqrt{\sin i}$, but would also add more severe pseudo-near-field terms to the displacement field in the finite difference grid.

The following solutions are for a whole-space, and are repeated from Chapter 1.2. For convenience, define

$$\Gamma_\alpha = \sqrt{\frac{2}{\alpha}} \frac{1}{4 \pi^2 \rho 10^{20}},$$
$$T_\alpha = \frac{R^2}{t^2 \alpha^2},$$

and

$$\Phi_\alpha = \frac{\Gamma_\alpha}{\sqrt{1 - T_\alpha}} H\left(t - \frac{R}{\alpha}\right) * \frac{d M_o(t)}{dt},$$

where H is the Heaviside step function, the $*$ indicates convolution, α is compressional wave velocity (km/sec), ρ is density (g/cm^3), t is time (sec),

and $\frac{d M_o (t)}{dt}$ is the rate of moment release. The factor of 10^{20} is for conversion of units. The analytic whole-space expressions for an isotropic explosion that may be used at the edges of the source box in a 2-D numerical grid are

$$Q_E = \frac{r}{\alpha^2 R} \Phi_\alpha \quad (42a)$$

and

$$W_E = \frac{z}{\alpha^2 R} \Phi_\alpha, \quad (42b)$$

where r is the horizontal component of R , and is positive in the direction of the receiver, and z is the vertical component of R , and is positive downward. Q_E and W_E are the radial and vertical components of displacement.

The expressions for Q and W for a "line force", which has a $\sin i$ radiation pattern are

$$Q_F = \frac{t r}{\alpha R^2} \Phi_\alpha (r^2 - z^2 + T_\alpha z^2) \quad (43a)$$

$$W_F = \frac{t z}{\alpha R^2} \Phi_\alpha (- 2 r z + T_\alpha r z) \quad (43b)$$

By judiciously mixing the explosive and force terms, we can modify the vertical radiation pattern of the explosion to mimic the $\sqrt{\sin i}$ we desire. Figure 1.16 shows the radiation patterns that result from using 100% explosion, 50% explosion mixed with 50% force, and 40% explosion mixed with 60% force. These cases are compared with the $\sqrt{\sin i}$. Energy that leaves the source at angles near $i = 90^\circ$ is not affected by the correction, but energy at angles near $i = 0^\circ$ is markedly affected. The mix of explosive and force

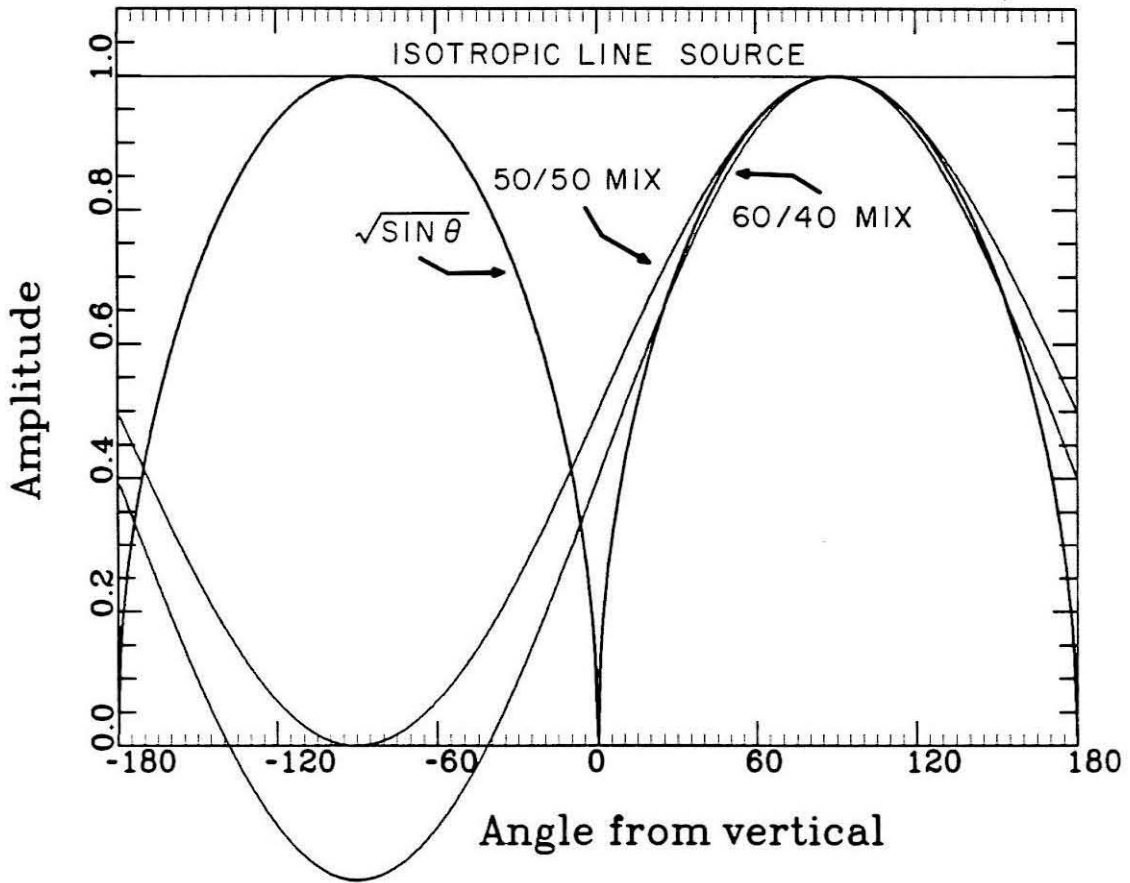


Figure 1.16 Comparison of radiation pattern for corrected and uncorrected line sources. The level line shows the isotropic radiation pattern which results from an uncorrected explosive line source. The $\sqrt{\sin i}$ curve shows the best radiation pattern to simulate an explosive point source. The two sinusoidal curves show the result of mixing a line source force with a line source explosion with 50%/50% and 60%/40% weighting. The mixed sources are meant to be accurate in the range $i = +20^\circ$ to $+160^\circ$.

source expressions determines where in the radiation pattern the source is most accurate. The 50%/50% mix is most accurate near $i = 90^\circ$ and the 60%/40% mix is less accurate near $i = 90^\circ$, but is more accurate near $i = 30^\circ$, as may be seen in Figure 1.16. It is clear from Figure 1.16 that only energy leaving the source at positive angles may be modeled with this corrected source.

As described in above in Sections 1.2 and 1.3, the line source seismograms extracted from the finite difference (FD) grid, \tilde{Q} and \tilde{W} , are transformed into point seismograms by:

$$Q_p = \frac{1}{\sqrt{R}} \frac{d}{dt} \left(\frac{1}{\sqrt{t}} * \tilde{Q} \right) \quad (44a)$$

$$W_p = \frac{1}{\sqrt{R}} \frac{d}{dt} \left(\frac{1}{\sqrt{t}} * \tilde{W} \right), \quad (44b)$$

where Q_p and W_p are horizontal and vertical displacements in cm.

Test of improvement due to correction factor

This correction factor will change the relative amplitude of arrivals by the $\sqrt{\sin i}$ factor shown in Figure 1.16. The effect of the 50%/50% correction plotted in Figure 1.16 on the seismograms for an explosion in a half-space is shown in Figure 1.17. The corrected FD seismograms have larger amplitude Rayleigh waves relative to the direct compressional waves than do the uncorrected seismograms, and agree better with the seismograms generated by the Cagniard method, which is known to be accurate (see, for example, Apsel and Luco, 1983). The $\sqrt{\sin i}$ corresponds to $\sqrt{p_o}$, where the real part of the slowness p is $Re(p) = rt/R^2$. The correction increases the size of the

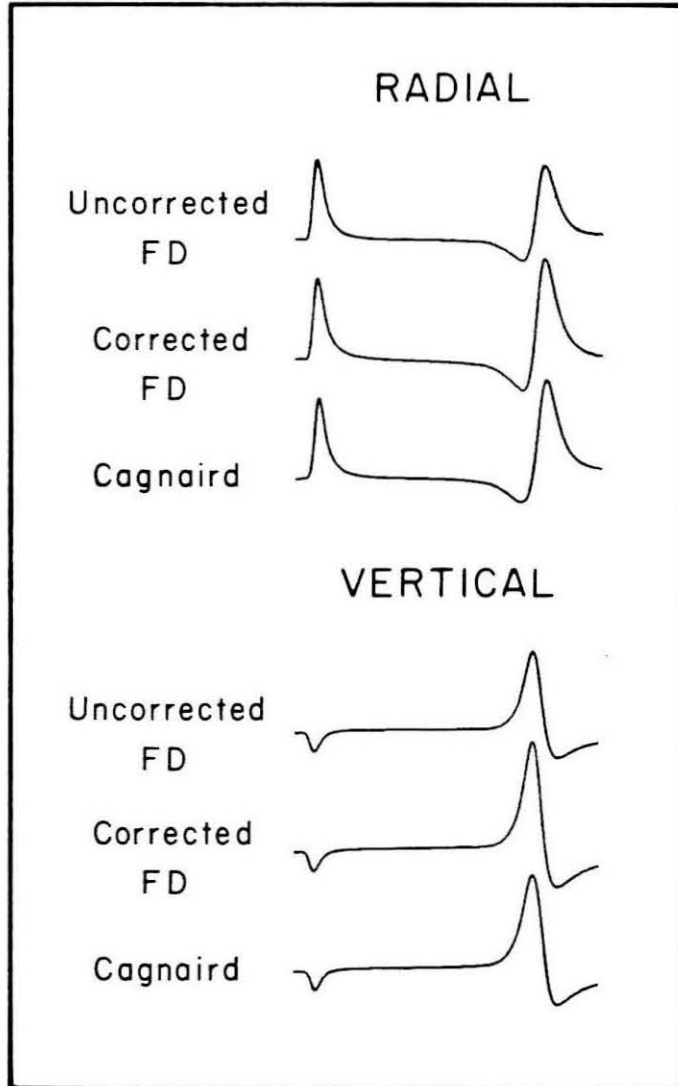


Figure 1.17 Comparison between uncorrected and corrected FD seismograms and analytic Cagnaird seismograms for an explosive point source in a half-space. The receiver is at a range 30 times the source depth to allow for the development of a Rayleigh wave large compared to the direct P-wave. The amplitude scale is the same for all the radial and all the vertical traces, but different between the radial and vertical components.

Rayleigh waves because they have a greater slowness p than the direct compressional waves.

The more nearly vertically the energy is traveling, the more important the correction becomes. For takeoff angles i near 20° , the correction term reduces the amplitude by a factor of 2, as is shown in Figure 1.16. In modeling short-period P waves from the Nevada test site, Stead and Helmberger (1985) have found this correction to be crucial.

For dislocation sources, however, the complicated radiation patterns dominate the seismograms, although the same $\sqrt{\sin i}$ problem arises. This effect is shown above in Figure 1.14, where seismograms due to dislocation sources are compared with Cagniard seismograms for a layer over a half-space geometry. The layered model is given in Table 1.1. Although slight amplitude discrepancies appear, they are subtle compared with the amplitude effects of the radiation pattern.

For a more demanding test of the corrected explosive source, a model that was developed for Amchitka Island which consists of a stack of 8 layers over a half-space is used. The P-wave crustal model consists of 9 layers derived by Burdick (1984) by fine-tuning the model proposed by Engdahl (1972). This model predicted the observed P-wave travel times well (1984). The S-wave velocity structure was added to model the Rayleigh wave arrivals by Burdick (1984). The layered model is given in Table 1.2. In Figure 1.18, the FD results are compared with those of the wavenumber-frequency numerical integration (WI) approach of Burdick (1984), which is similar to that of Apsel (1979). The RDP (reduced displacement potential), which is a source time function, of Helmberger and Hadley (1981) is used, namely

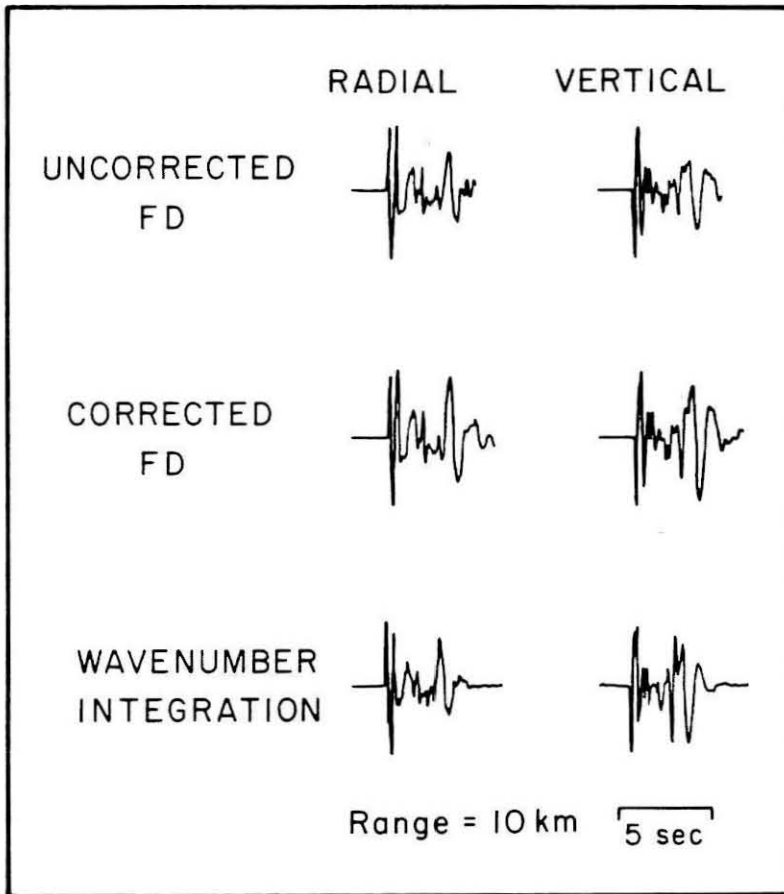


Figure 1.18 Comparison between uncorrected and corrected FD seismograms and frequency-wavenumber integration seismograms for an explosive point source in the layered velocity model described in Table 1.2. The source depth is 1.2 km and the receiver is at a range of 10 km.

Table 1.2 : Velocities in Burdick's (1984) model

P-wave velocity (km/sec)	S-wave velocity (km/sec)	density g/cm ³	layer thickness km
3.4	1.7	2.3	0.2
3.7	1.9	2.4	0.6
4.2	2.1	2.4	0.5
4.6	2.3	2.5	0.5
4.9	2.8	2.6	0.7
5.1	2.9	2.7	0.5
5.9	3.3	2.7	6.0
6.9	4.0	2.8	28.0
8.2	4.7	3.2	∞

$$\Psi(t) = \Psi_{\infty} \left[1 - e^{-Kt} \left(1 + Kt + 0.5(Kt)^2 - B(Kt)^3 \right) \right] \quad (45)$$

In Figure 1.18, the corner frequency parameter, K , is set at 8 sec^{-1} and the overshoot parameter B is set at a value of 1.

The corrected FD seismograms agree well with the wavenumber-frequency integration algorithm, but the uncorrected FD seismograms have surface waves that are too small relative to the body waves. The FD method, in addition to allowing lateral structural heterogeneity, is faster than the wavenumber-frequency method. Cagniard calculations for this model are impractical as innumerable multiples within the layered stack would have to be summed.

Chapter 2

Application to modeling the strong motions of earthquakes

2.1 Introduction

The understanding of earthquake generated motions has improved significantly in recent years. This progress is due in large part to the refinement of methods for generating synthetic seismograms to compare with an ever growing collection of observations. Synthetic seismograms are generally used in iterative forward modeling schemes where the source and medium parameters are perturbed until a best match with the data is obtained. This technique has proven to be powerful for determining subtle features of both the source and the medium. The technique is limited, however, by the range of earth structure that can be modeled. Traditionally, the earth models have been a stack of homogeneous layers, which is inadequate for laterally heterogeneous structures such as ocean-continent transition zones and basin structures.

In Chapters 2 through 4, we relax some of these limitations by allowing dipping structure with the procedure described in Chapter 1, whereby 2-D finite-difference (FD) calculations can be mapped into synthetic seismograms with the proper point source shear dislocation characteristics. This procedure has the advantage of allowing for arbitrary density and velocity fields in two dimensions.

First, this technique is applied to model the seismogram recorded at El Centro for the 1968 Borrego mountain event. The next two sections, Sections 2.3 and 2.4, compare synthetic seismograms and data from the 1971 San Fernando earthquake.

The San Fernando earthquake of February 9, 1971 produced one of the most complete sets of strong-ground records from a large thrust earthquake to date, and consequently has generated a large body of seismological literature. Hanks (1975) notes that seismic moment, source dimension, radiation pattern, rupture propagation, the development of local surface waves and their subsequent dispersion, and azimuthal variations in the gross geological structure all appear to have first-order significance in fashioning the amplitude and frequency content of the strong-motion waveforms. Heaton (1982) has modeled some of these features, but adds that many features of the observed motions remain unexplained, and considerable uncertainty still exists regarding the faulting history of the San Fernando earthquake.

One drawback of existing studies is the inability to properly simulate the propagational effects associated with the complicated sedimentary basins in and around Los Angeles. Finite-difference (FD) and finite element schemes have proven useful in explaining some of the surface wave distortions (Drake and Mal, 1972) and the static deformation (McCowan et al., 1977). However, these efforts did not address the demanding task of modeling seismic profiles along paths crossing the various basin and ridge structures, as discussed qualitatively by Liu and Heaton (1984). The modeling of one such three-component profile is the subject of Sections 2.3 and 2.4.

2.2 The El Centro recording of the Borrego Mt. earthquake

We have developed above a method for constructing seismograms for general structures, but it remains to show that this flexibility aids in the interpretation of data. To show its usefulness, we will investigate the well-studied Borrego Mountain strong-motion recording from El Centro. Figure 2.1 shows the relative locations of the epicenter, major structures, and the receiver. The displacement data is summarized in Figure 2.2, which is taken from Heaton and Helmberger (1977). The agreement between the deconvolved Carder displacement record and the integrated accelerogram is excellent. El Centro is located along the strike of the fault, roughly 8° off, which places it near the SH maximum and a P-SV node. If the station were at a P-wave node in the far-field on a flat-layered earth, one would expect the N-S and E-W traces to have the same waveform, and all the energy would rotate to the transverse component. For simplicity, we follow Ebel and Helmberger (1982) in modeling the the first 50 seconds of the N-S integrated accelerogram after dividing by $\cos 37^\circ$, which is the angle between the back-azimuth and north. This record is shown as the second trace of (a) in Figure 2.2. For later times, the motion appears to arrive at the station mostly on the radial and would not be explicable with a two-dimensional SH model. The objective of this section is to investigate the effect of using the most recent data about the cross-sectional structure on the long-period motions, given the simple teleseismic source description.

One of the first teleseismic waveform modeling studies was conducted on this earthquake by Burdick and Mellman (1976). They modeled the long-

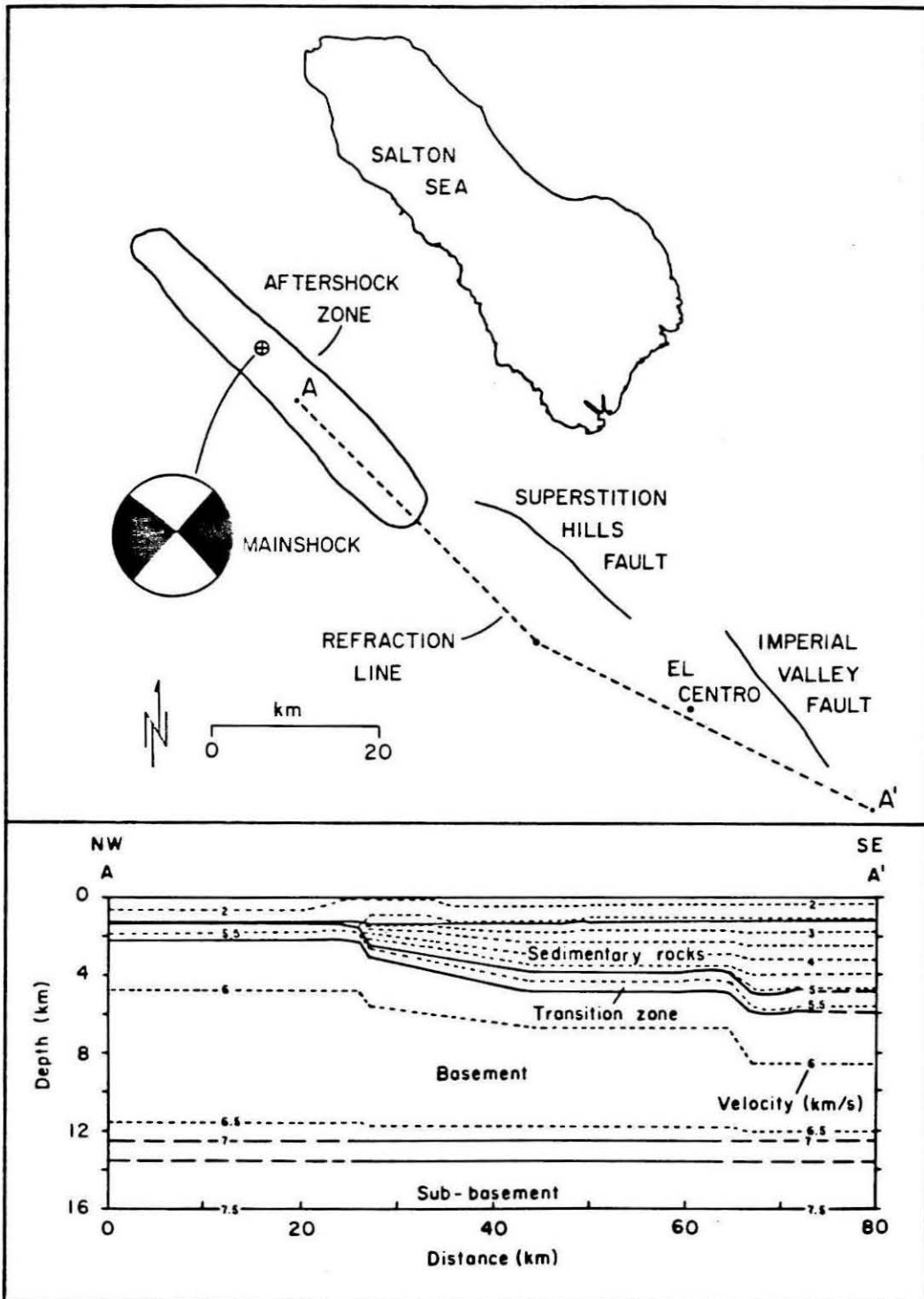


Figure 2.1 Sketch map of the area of the Borrego Mountain mainshock and the El Centro strong motion station. The aftershock zone and some of the faults in the area are shown. The cross-section shows the P-wave velocities estimated by Fuis et al. (1983) from refraction work along profile A-A'.

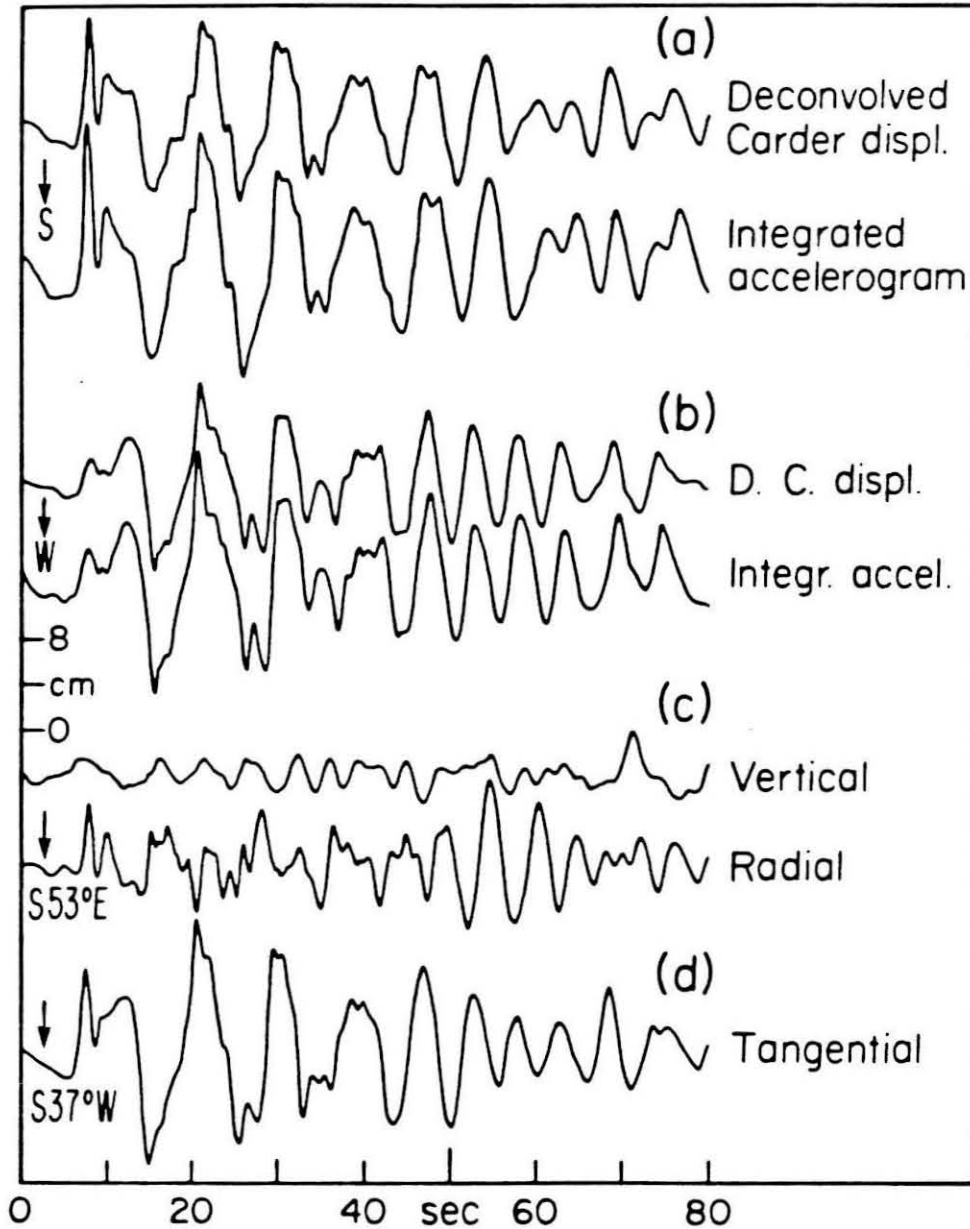


Figure 2.2 Summary of observed ground motion. (a) Comparison of deconvolved Carder displacement meter record and integrated accelerogram for N-S component. (b) Comparison of deconvolved Carder displacement meter record and integrated accelerogram for E-W component. (c) Ground motion rotated into vertical, radial, and tangential components. From Heaton and Helmberger (1977).

period P-waveform with P, pP, and sP rays as well as the long-period SH-waveform with S and sS rays. Their results suggest a zone of faulting around a depth of 8 km, with three distinct sources. Their first source has 75% of the moment and has the expected focal mechanism. The other two subevents have unexpected mechanisms that may be a result of crustal phases produced by non-planar structure, and are less accepted by the seismological community. More recently Ebel and Helmberger (1982) studied the P-wave complexity and found evidence for two asperities. Forward and inverse modeling of the data suggest a two source model, each of less than 2 second duration. The second source occurred about 2.2 seconds after the first and both events appear to be at a depth of 8 km. This complex source was used to synthesize the direct SH arrival on velocity and acceleration records with some success. The long-period teleseismic synthetics generated with the more complicated source model appears to agree well with those from the initial source found by Burdick and Mellman (1976).

Little evidence for shallow faulting is suggested by the teleseismic data. On the other hand, Heaton and Helmberger (1977) suggest substantial shallow faulting to explain the strength of the Love waves at El Centro. From a modeling point of view, one would expect the ratio of body waves to surface waves to be an excellent depth discriminant. However, a flat-layered model may not provide the appropriate Green's function in this particular path as suggested by the recent study of Fuis et al. (1983). We will investigate the properties of the more complicated Green's functions in this study using the first long-period source found by Burdick and Mellman (1976), namely a 0.1, 1.0, 4.0 second trapezoid.

Three structures are shown in Figure 2.3 that increase in verisimilitude as well as complexity from model A to model C. Model A is the layer over a halfspace used by Heaton and Helmberger (1977) and Swanger and Boore (1982). Model B is a more accurate dipping layer model. Model C is the S-wave version of the structure from Fuis et al. (1983). The S-wave velocities for profiles on the left and right sides of model C are given in Table 2.1. The ratio of P- to S- wave velocity is assumed to be $\sqrt{3}$ except in the top layer where it is taken to be 2.

A strike-slip source is introduced with the depth (8 km) and the time function (a 0.1, 1.0, 4.0 second trapezoid) estimated from teleseismic studies (Burdick and Mellman, 1976). The resulting displacements for models A, B, and C are shown in Figures 2.4a, 2.4b, and 2.4c. The El Centro displacement record is shown in Figure 2.4d. The seismogram in Figure 2.4e results from a perturbation to model C discussed below.

The flat-layered model A generates the correct initial long-period displacement, as it was designed to do. There is little short-period energy, and the signal dies away too fast. The dipping-layer model B is seen to trap short-period energy in Figure 2.4b, as discussed below, but the long-period energy does not mimic that in the data.

The seismogram in Figure 2.4c from model C matches the first 20 seconds of the data reasonably well, aside from the initial pulse. The initial pulse is higher in frequency and arrives with a polarization suggesting a direction of travel that is 30° away from the azimuth from receiver to source. This section is focusing on a match to the longer-period displacement records with can be attained with a 2-D model, as discussed above, so the misfit with the initial

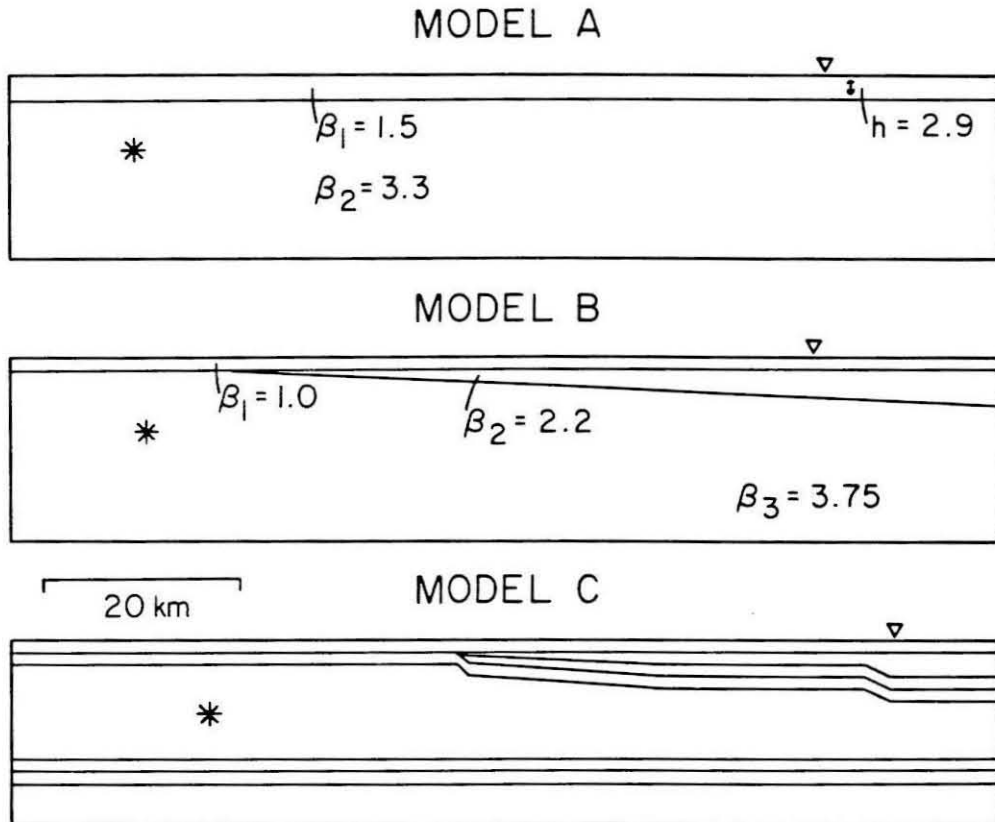


Figure 2.3 Three models of the structure between the Borrego Mountain earthquake, shown by an asterisk, and the El Centro station, shown by a small triangle. There is no vertical exaggeration. The velocities and assumed densities for the profiles on the left and right sides of the model are given in Table 2.1.

Table 2.1 : Velocities in model C

S-wave velocity km/sec	density g/cm ³	depth to top of layer km	
		left side	right side
1.0	1.4	0.	0.
1.55	1.9	1.6	1.6
1.8	2.0	--	3.8
3.0	2.3	1.8	5.0
3.75	2.7	2.6	6.2
4.0	2.8	12.2	12.2
4.125	2.8	12.6	12.6
4.25	2.9	13.2	13.2
4.375	2.95	13.8	13.8
4.5	3.0	14.2	14.2
4.625	3.1	14.6	14.6
4.75	3.2	15.2	15.2

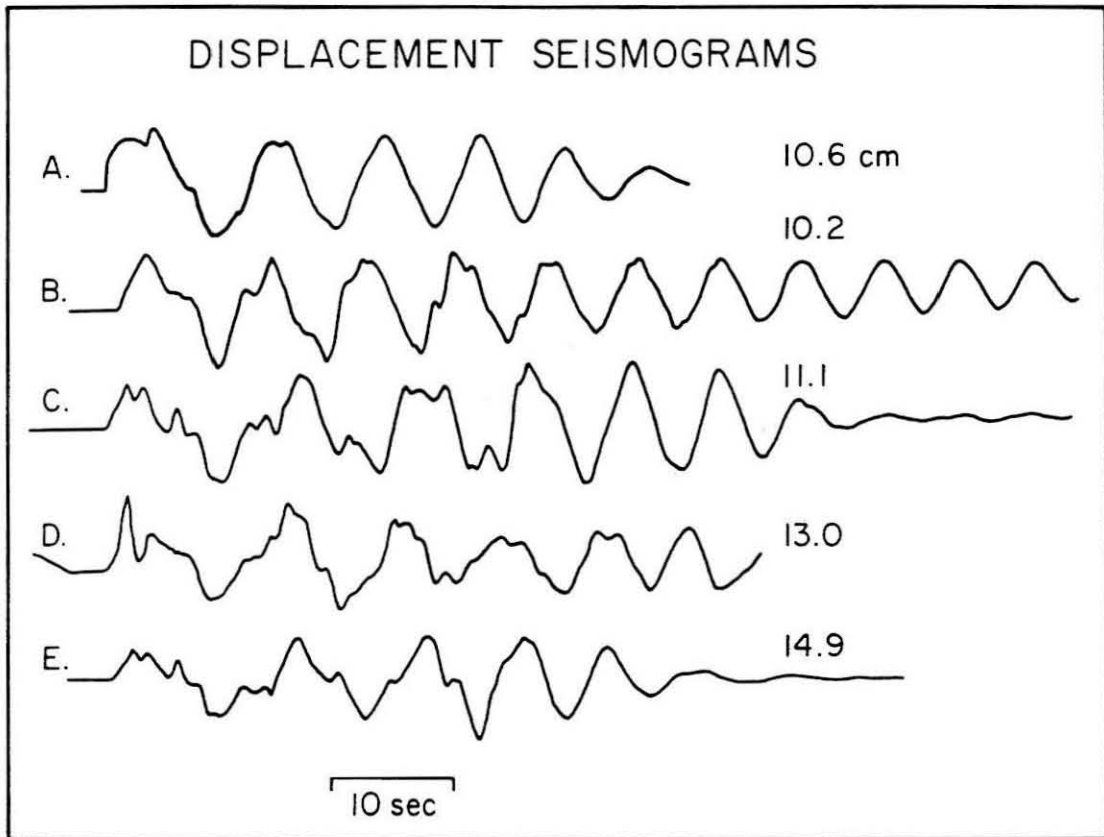


Figure 2.4 The displacements at El Centro resulting from: (a) model A in Figure 2.3, (b) model B in Figure 2.3, (c) model C in Figure 2.3, (d) the actual earthquake, and (e) model C, but with the velocity of the top layer set to 1.2 km/sec instead of 1.0 km/sec. See text for detailed description.

pulse is not investigated in this paper.

A moment of 1.2×10^{26} dyne-cm is found by matching the amplitude of the synthetic in Figure 2.4c with the displacement record, which is similar to the result of 1.1×10^{26} found by Burdick and Mellman (1976) from teleseismic body waves and also by Butler (1983) from long-period surface waves.

Profiles for a single layer that dips down away from the source are shown in Figure 2.5 both to reaffirm the accuracy of our methods and to investigate the effect of dipping layers. The agreement in waveform and amplitude is excellent (see Helmberger et al., 1985, for GRT method). The initial arrival has the same frequency content as the source but the later arrivals have higher frequency content. This phenomenon may be qualitatively understood as follows. In the geometrical ray limit, energy is trapped in the layer when it is refracted by the dipping interface past the critical angle. In the low-frequency limit, the energy is not affected by the thin layer.

The depth sensitivity of the seismograms is investigated by the GRT method (Helmberger et al., 1985) in Figure 2.6. The GRT method is considerably faster than the FD method and generally can treat higher frequencies, so when the structure is simple enough, the GRT method is preferred.

Seismograms for the flat-layered case vary much more than they do for the dipping-layer case when the source depth changes. The depth sensitivity is an important issue. Sibson (1982) argues that one would expect the most moment release from the deeper parts of the fault plane. McGarr (1984) presents data that suggest that peak accelerations and velocities depend strongly on focal depth. For the Borrego Mountain earthquake, Heaton and Helmberger (1977) postulate a component of moment release in the shallow

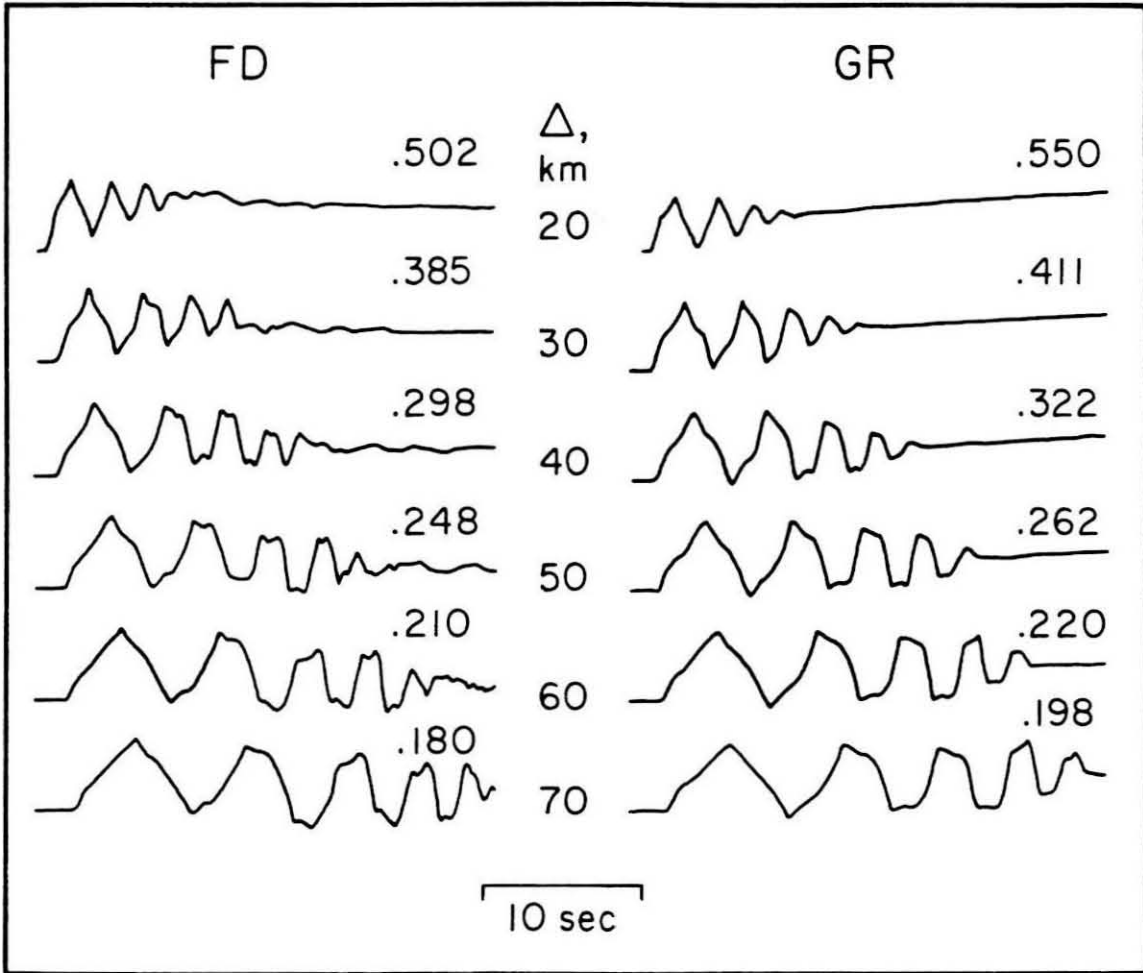


Figure 2.5 Profiles for a single layer that dips down 2.8° from the horizontal away from the source. The layer is 0.3 km thick directly above the source. The source is 6 km below the surface. A trapezoidal time function of 0.3, 0.3, 0.3 seconds has been convolved into both suites of seismograms. The seismograms on the left are generated by the FD method described above, those on the right are from a generalized ray method.

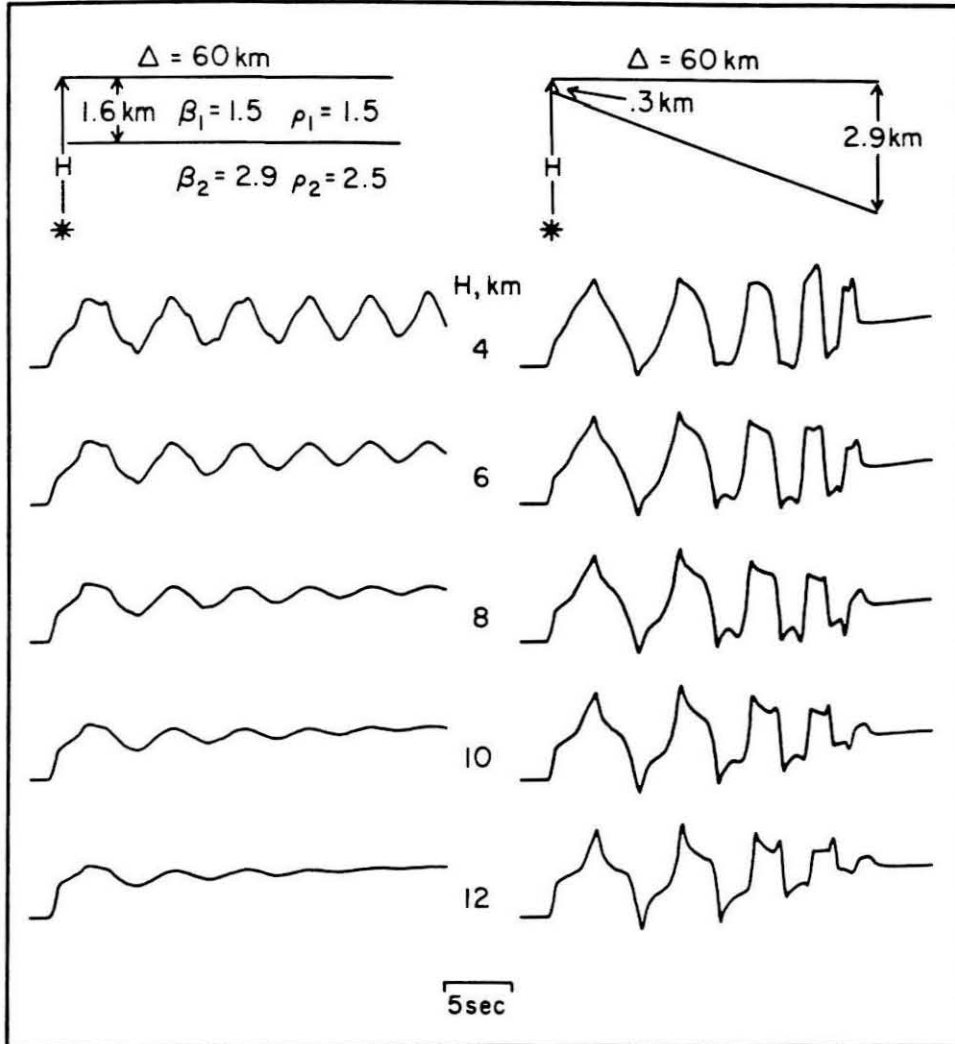


Figure 2.6 Profiles for a single layer that is either flat (left), or dips (right). The geometries are given at the top of the figure, note that the layer thickness is the same under the station in both cases. A trapezoidal time function of 0.2, 0.2, 0.2 seconds has been convolved into both suites of seismograms.

sediments to generate enough long-period energy to match the data. With the more realistic structure derived from the refraction profile, there is instead too much long-period energy 30 to 40 seconds into the record in Figure 2.4c, so the need for a shallow component of moment is no longer as evident.

The structure about Borrego Mountain has considerable variations in all three dimensions, as may be seen by the structures shown on Figure 2.1 or by the various cross-sections in Fuis et al. (1983). This variation may also be seen by noting in the radial and tangential components of the El Centro record shown in Figure 2.2 that both the initial SH pulse and the later portion of the Love wave approach El Centro off-strike by up to 30° . As a result, it is not clear what is the appropriate velocity structure to use for modeling the El Centro record.

Many parameters could be perturbed in the attempt to improve the fit to the data. The time function, source finiteness, and velocity structure are not known beyond a shadow of a doubt. The seismogram in Figure 2.4e, generated from model C with the velocity in the top 1.8 km increased by 20%, illustrates that small changes in structure can cause significant differences in the synthetic seismogram. Figure 2.6 shows, however, that the source finiteness does not make nearly as large a difference as in the flat layer case. We suspect that the source time function and the structure are the primary determinants of the seismogram, and we do not know the 3-D structure well enough to uniquely determine the time function from the El Centro record. With just the one station used in this study, the source finiteness is difficult to investigate.

The good agreement between the data and the synthetic seismogram shows that incorporating the known 2-D structure can lead to improved prediction of path effects on long-period strong-ground motion.

2.3 The San Fernando earthquake: forward modeling

Strong motion records

The filled triangles in Figure 2.7 locate three-component accelerometers that recorded the strong motions of the San Fernando earthquake along a north-south profile. Figure 2.8 shows the vertical, radial, and transverse velocities recorded at these stations. The accelerations were integrated to velocities by EERL (1974). These records comprise profile I in Liu and Heaton (1984). The absolute timing of these records is not known so they are lined up relative to an early, high-frequency arrival on the vertical component that is probably a direct compressional wave.

Before discussing these motions in detail, it is useful to review the geological structure along this profile. A schematic cross-section is given on the bottom of Figure 2.7. Figure 2.9 shows the stratigraphy in this cross-section in more detail, with an inferred shear wave velocity structure below. The stratigraphy is taken from Duke et al. (1971), who reviewed the well logs and the geological cross-sections in the literature for this area. Many well logs have been recorded around the Los Angeles basins because of oil exploration and these logs yield estimates of density and velocity. Duke et al. (1971) also

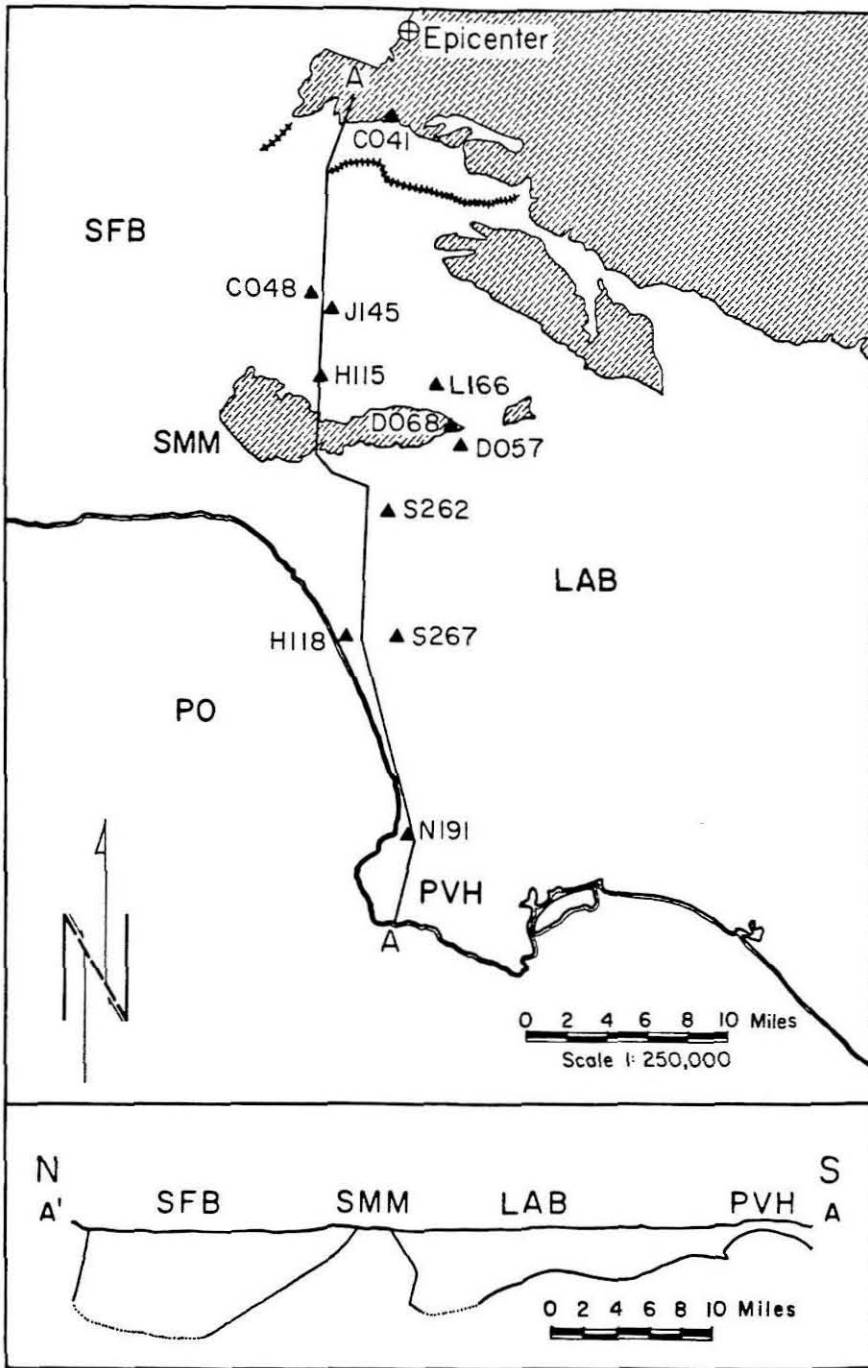


Figure 2.7 Map and cross-section of the San Fernando region from Duke et al. (1971). The epicenter is marked by a cross. The filled triangles are the locations of the strong-motion instruments used in this section. Cross-hatched areas show surface exposure of bedrock. The bottom of the basin for the profile A-A' is shown below, where dashed portions show where the boundary is not known. The cross-section has vertical exaggeration of 2:1. SFB indicates the San Fernando basin, SMM the Santa Monica mountains, LAB the Los Angeles basin, PVH the Palos Verdes hills, and PO the Pacific ocean.

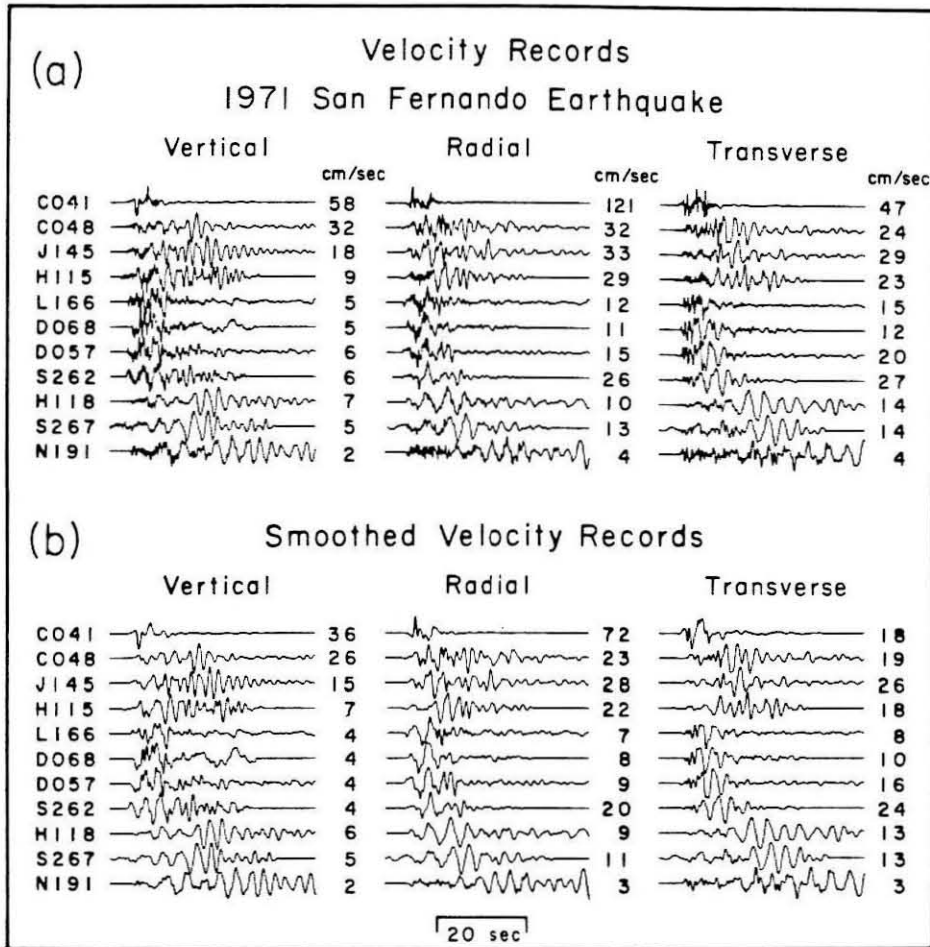


Figure 2.8 (a) Velocity records of the 1971 San Fernando earthquake, taken from EERL (1974). The traces are aligned relative to a high-frequency, early arrival on the vertical component that is interpreted to be a direct compressional wave. Amplitude is given in cm/sec. The station names are listed at the far left. The stations are shown in order of increasing epicentral distance, but the actual station spacing is irregular. (b) Smoothed velocity records. The records shown in (a) are convolved by a gaussian pulse about one second wide to filter out frequencies that cannot be properly handled by the finite-difference grid.

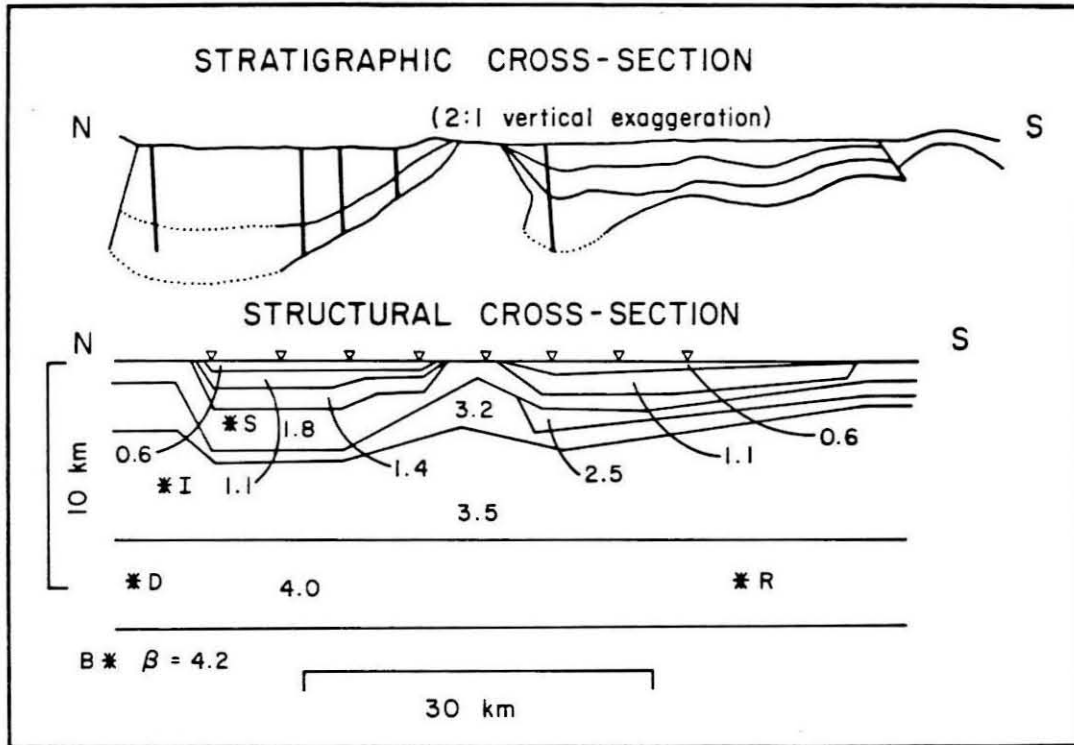


Figure 2.9 Stratigraphic and structural cross-section of the profile from the San Gabriel mountains on the left, across the San Fernando basin, the Santa Monica mountains, and the Los Angeles basin, to the Palos Verdes hills on the right. The stratigraphy is after Duke et al. (1971), and the velocities and density are also mostly derived from Duke et al. (1971). The heavy vertical lines in the stratigraphy diagram indicate the location of well logs used by Duke et al. (1971) to construct the model. Only the shear wave velocity is shown, the compressional wave velocity and the density corresponding to each shear wave velocity are given in Table 2.2. The encircled letters B, D, I, and S correspond to the locations of the bottommost, deep, intermediate, and shallow sources discussed in the text. The triangles along the surface mark the location of the receivers for the finite difference seismograms. The vertical exaggeration is 2:1.

Table 2.2 : Velocity and density structure for the cross-section in the middle of the San Fernando basin

P-wave velocity	S-wave velocity	Density
1.2	0.6	1.7
2.0	1.1	1.8
2.5	1.4	1.9
3.1	1.8	2.1
4.3	2.5	2.3
5.5	3.2	2.5
6.1	3.5	2.7
6.9	4.0	2.9
7.3	4.2	2.9

conducted numerous small-scale refraction surveys to find the near-surface compressional wave velocity profile. With knowledge of the composition of the rocks at depth, the shear wave velocity can also be reliably estimated. Near surface values of the attenuation operator Q have also been provided by Duke et al. (1971).

Although the structure within the San Fernando and Los Angeles basins along this profile can be reliably estimated from the above study, the structure below the basins is less well known since, unfortunately, the well logs stop as soon as they encounter the basement rock. Below the basins, we use the structure given in Kanamori and Hadley (1976) for compressional waves, and assume that V_p/V_s is $\sqrt{3}$. Table 2.2 gives the compressional wave velocity and density associated with each shear wave velocity shown in Figure 2.9.

The motions shown in Figure 2.8 appear to correlate with the geologic setting in which they were recorded. Within the San Fernando basin, a train of surface waves develop with an apparent velocity of 1 km/sec. On the Santa Monica mountains, the surface waves disappear and the amplitude falls by a factor of two. In the Los Angeles basin, the surface wave is again present with an even slower apparent velocity. Near the ocean, in the Palos Verdes hills, the surface wave is still present, but the amplitude has dropped more rapidly than geometric spreading would predict. These are the patterns we will attempt to understand by forward modeling with the FD technique.

Before forward modeling with a technique that assumes two-dimensional symmetry, we will verify that the seismic energy in the records is not significantly laterally reflected. Vidale (1986) uses complex polarization analysis that is an extension of the method of Montalbetti and Kanasewich

(1970) to examine the three-component records for this profile of records from the San Fernando earthquake. Because the method works in the complex domain, elliptically as well as linearly polarized data may be interpreted. This analysis finds the strike of propagation for the Love and Rayleigh waves. The strike may be obtained because the Love wave is linearly polarized transverse to the direction of propagation, and the Rayleigh wave is elliptically polarized in the plane that contains the vertical and the propagation directions.

The analysis in Vidale (1986) shows that the energy in this particular profile is traveling within 15° of radially outward from the source. This suggests that despite the three-dimensional nature of the basins, the geometry may be approximated by a two-dimensional model with useful results. We should note, however, that although the energy in this profile travels radially out from the source to the receiver, amplitude attenuation due to geometrical spreading depends on the curvature of the wavefront, so the amplitude may vary somewhat due to three-dimensional effects even if the energy path is not laterally deflected.

To match the frequency limitations of the FD algorithm, we low-pass filter the data. The FD method can only propagate energy with ten or more grid points per wavelength, so to properly treat high frequencies, more grid points and therefore more computation is required. Figure 2.8b shows the filtered vertical, radial, and transverse velocities that will be addressed in this modeling study. The peak velocities and waveforms are not strongly altered by this filter. The accelerations, on the other hand, are too high-frequency to model with the FD code in the way we model the velocities.

Review of source parameters

The San Fernando earthquake has also been the subject of studies that concentrated on other data sets, namely the teleseismic body waves, the surface waves, the location of preshocks and aftershocks, and the static displacements. These studies will help us estimate the source parameters. First, we will briefly review these studies to help limit and clarify some of the uncertainties.

The seismicity studies (Allen et al., 1973, Whitcomb et al., 1973) reveal a relatively diffuse zone of aftershocks with a combination of thrust and left-lateral strike-slip mechanisms. By locating the mainshock relative to well-located aftershocks recorded on a temporarily deployed array, Whitcomb et al. (1973) place the hypocenter at a depth of 8 kms at $34^{\circ} 24.7'$ N and $118^{\circ} 24.0'$ W, with the mechanism listed in Table 2.3. The errors in hypocentral depth are conservatively estimated at ± 8 km vertically and ± 4 km horizontally. The aftershocks suggest that the plane of faulting dipped 35° to the north down to 8 km depth, below which the fault plane dipped 50° .

Examination of the static displacements due to the earthquake (Alewine, 1974) reveals distributed slip from near the surface to a depth of about 14 km along the north dipping fault plane. The portion of the fault from the surface down to 5 km depth underwent about 5 m of slip, and the segment from 10 to 14 km depth shows 2-5 m slip, and there may be an area of less slip from 5 to 10 km depth. The greater the depth, however, the worse the resolution of static analysis. The long-period moment is estimated to be between 1.0 and 2.2×10^{26} dyne-cm in this analysis.

The 16-60 sec fundamental Rayleigh waves generated by the San Fernando earthquake are analyzed by Alewine (1974), and given the strike and dip suggested by Whitcomb et al. (1973), the moment is found to be 1.7×10^{26} dyne-cm. Half the moment release is found to be at depths of about 3-8 km and the other half of the moment release is below about 10 km.

The teleseismic body wave studies (Langston, 1978, and Heaton, 1982) use records from long-period WWSSN stations to find the mechanism and longer-period (5-30 second period) faulting history in time and space. The short-period WWSSN records are also examined in the search for higher frequency (0.5-3.0 second period) details of the faulting history (Hanks, 1975, and Langston, 1978).

Both Langston (1978) and Heaton (1982) find a double source. There is a source at 10-15 km depth with a moment 0.5×10^{26} dyne-cm and there is a shallower source with a shallower dip that also has a moment of 0.5×10^{26} . The two sources are found to have a slightly different strikes and the shallower source dips less, as shown in Table 2.3. When Heaton (1982) attempts to model the near-in records and static data as well as the teleseismic data, his estimate of the total moment rises to 1.7×10^{26} dyne-cm. Figure 2.10 summarizes the results from the teleseismic modeling of Langston (1978) and Heaton (1982).

The work of both Langston (1978) and Hanks (1975) suggest that the first pulse of short-period energy originated about 12 km below the surface. If the pulse of energy came from the hypocenter, which was on the fault plane as defined by the aftershocks, the location from Whitcomb et al. (1973) would have to be in error by 4 km vertically and 4 km horizontally. Some of the

Table 2.3 : Source parameters of the San Fernando earthquake

Study Method	Strike	Dip	Rake	Depth	Moment X 10 ²⁶ dyne-cm
	Single	Source			
<u>Whitcomb(1973)</u> First motions	-67°	52°	72°	8 km	-
<u>Alewine(1974)</u> Static displacements	-67°	53°	72°	0-14 km	1.0-2.2
<u>Alewine(1974)</u> Surface waves	-67°	53°	66-82°	0-15 km	1.7
	Multiple	Sources			
<u>Langston(1978)</u> Teleseismic records	-79°	44°	80°	15 km	0.53
<u>Langston(1978)</u> Teleseismic records	-80°	18°	96°	10 km	0.32
<u>Langston(1978)</u> Teleseismic records	-70°	53°	76°	8-15 km	0.41
<u>Heaton(1982)</u> combined study	-80°	29°	90°	0-10 km	0.45
	-70°	54°	76°	3-16 km	0.7
	-75°	45°	90°	0-10 km	1.0

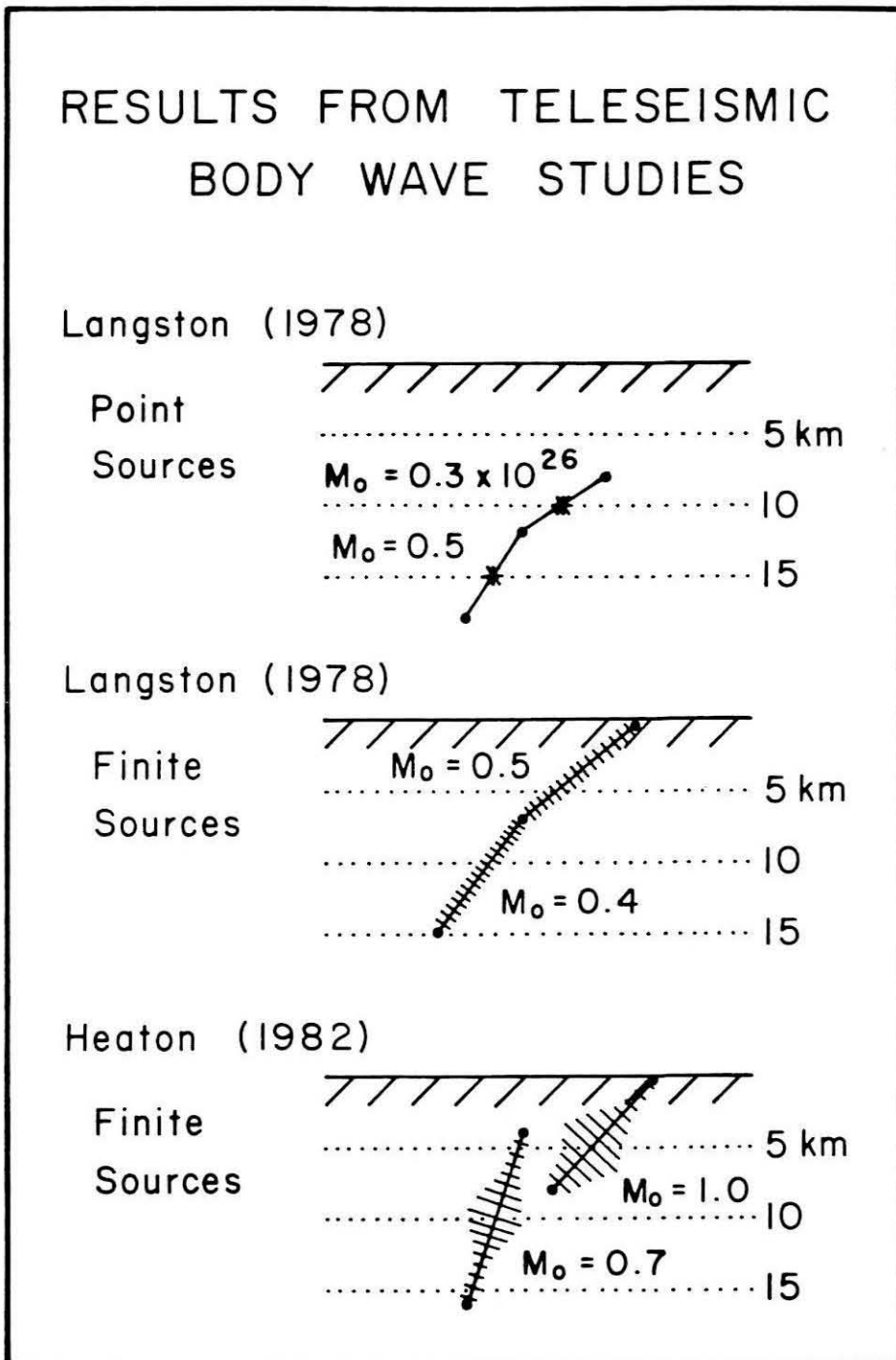


Figure 2.10 Schematic summary of results from teleseismic body wave studies. Langston (1976) interprets the faulting of the San Fernando earthquake as two point sources in (a) and as two finite segments in (b). Heaton (1982) combines the teleseismic data, near-field data on hard rock sites, and static data to find the two non-intersecting finite fault segments shown in (c). The details of these models may be found in Table 2.3.

short-period WWSSN records, however, indicate a small precursor about 2 seconds before the initial large pulse, so perhaps the hypocenter and the location of the short-period energy release are not coincident.

In this study, we find that a point source at a 10 km depth with the mechanism of Heaton's deep source (which nearly identical to Langston's deep source) can explain most of the data. The sensitivity of our modeling to changes in source depth and mechanism are discussed below.

Numerical models of the strong motions

We use the two-dimensional FD SH and P-SV algorithms described in Chapter 1 and Clayton and Vidale (1986), and Vidale and Clayton (1986) to calculate the Green's functions. For example, the tangential motions for a point dislocation source can be obtained by evaluating equations (30) and (31) in Chapter 1. The function $\dot{D}(t)$ is the far-field time history (this term is written out as $dM_o(t)/dt$ in equation (30)), which is the temporal derivative of the dislocation time function. Estimates of \dot{D} can be obtained in a variety of ways. This FD procedure does not handle the near-field terms properly at small horizontal distances, but numerical checks indicate accurate results beyond about 10 km for a source at a depth of 10 km.

The Green's functions for impulsive strike-slip and dip-slip sources at the four locations shown in Figure 2.9 are displayed in Figures 2.11 and 2.12. The ranges indicated on the left are approximate and correspond to fixed positions at the surface as indicated in Figure 2.9, and are appropriate for the deepest source. Note that the shallower sources are located further to the south. The change in polarity for the first station for the source S indicates that the

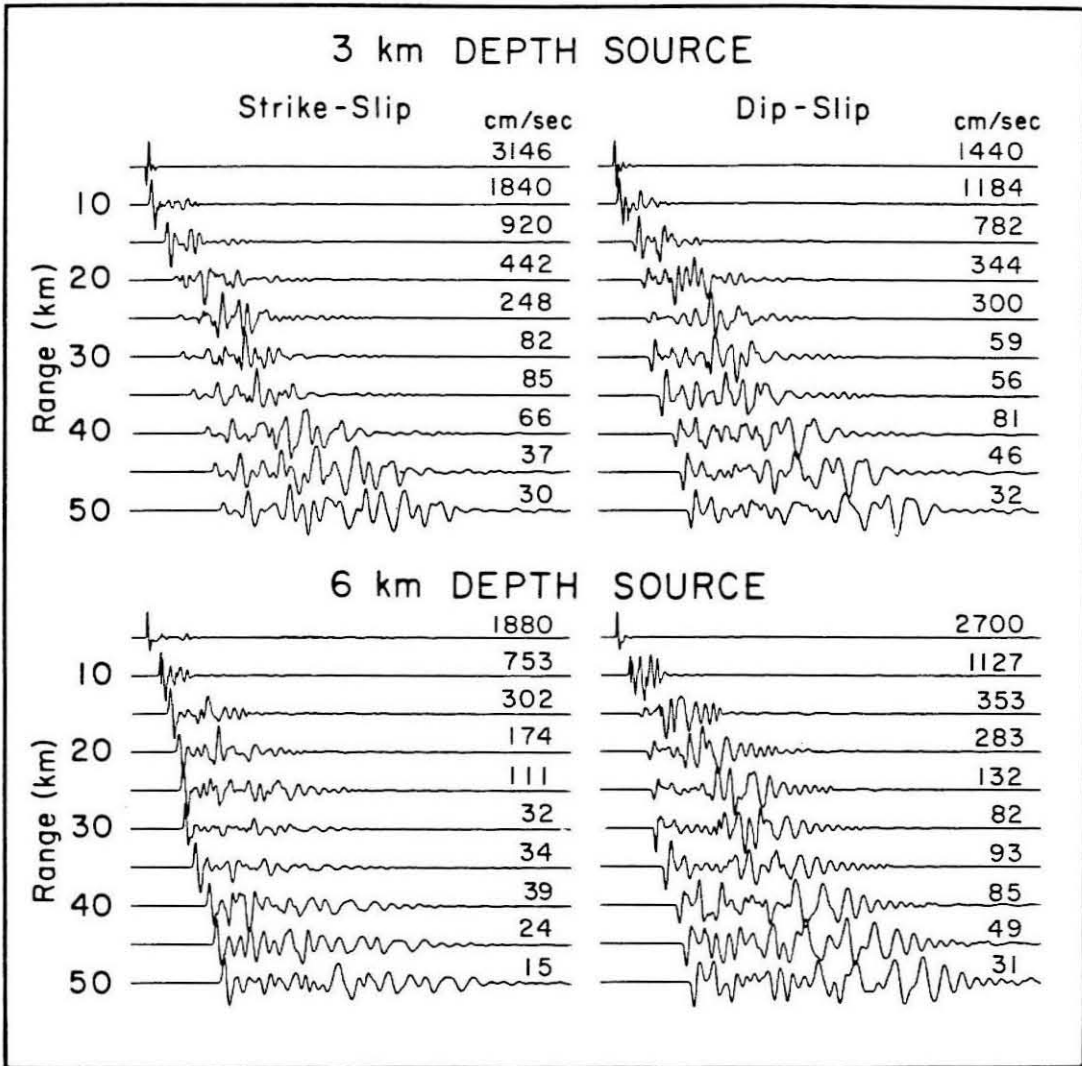


Figure 2.11 Green's functions for the transverse component of velocity with 3 and 6 km source depths, labeled S and I on Figure 2.9. The strike-slip case corresponds to $A_4 = 1$ and $A_5 = 0$, and the dip-slip case corresponds to $A_4 = 0$ and $A_5 = 1$. Moment scaling is discussed in the text. The source time function is impulsive, and the frequency content is limited by the seismic Q of 25.

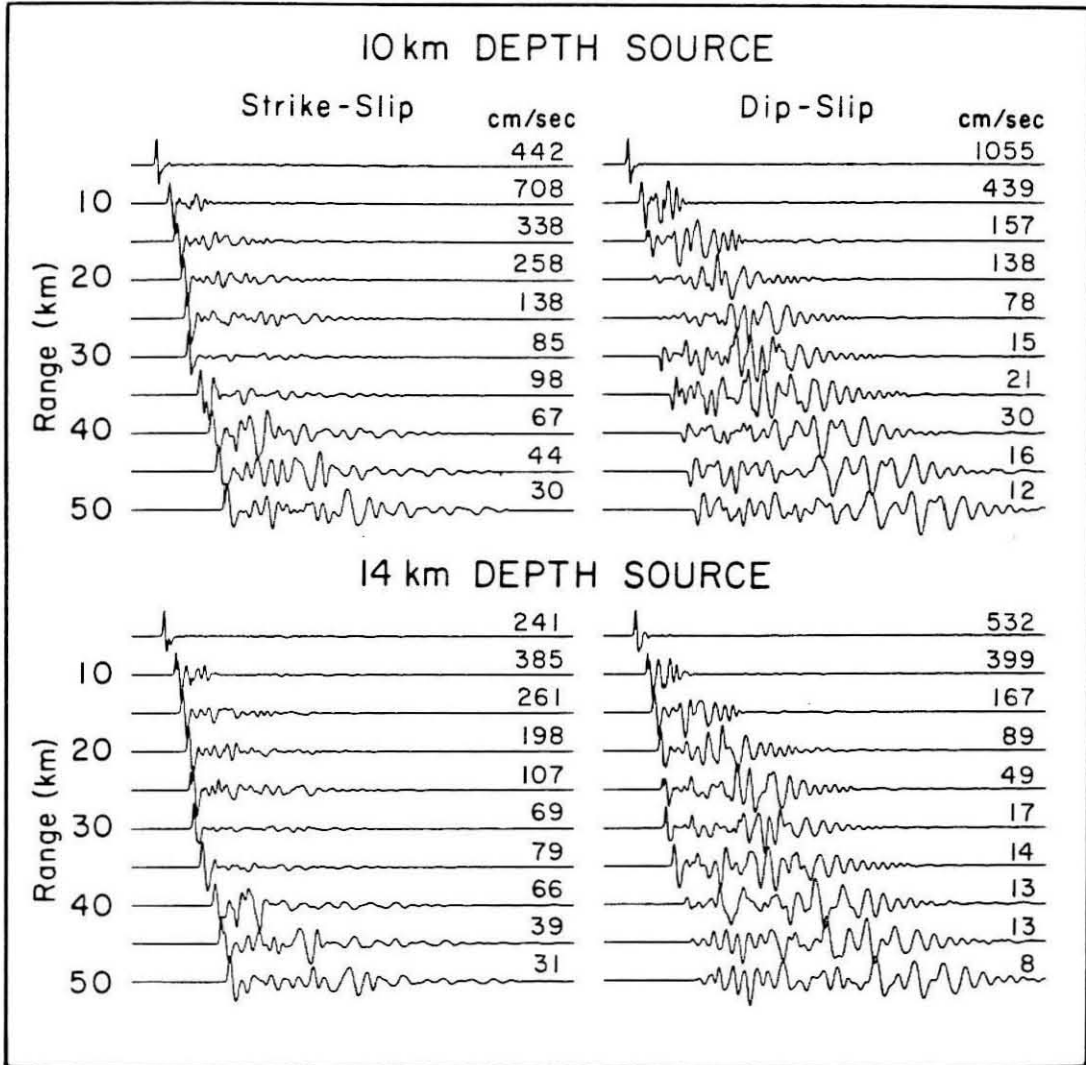


Figure 2.12 Green's functions for the transverse component of velocity with the 10 and 14 km source depths, labeled D and B on Figure 2.9. The strike-slip case corresponds to $A_4 = 1$ and $A_5 = 0$, and the dip-slip case corresponds to $A_4 = 0$ and $A_5 = 1$. Moment scaling is discussed in the text. The source time function is impulsive, and the frequency content is limited by the seismic Q of 25.

source is actually south of the first receiver. However, we are only interested in these solutions at the larger distances where the near-field terms can be neglected. A seismic attenuation Q of 25 is assumed; this value falls within the wide range of Q 's reported by Duke et al. (1971). A moment of 10^{26} dyne-cm is used for the 10 km source depth. To compare amplitudes between different depths, we hold AD_0 rather than the moment μAD_0 constant to avoid the strong tendency to generate larger seismic motions in softer material.

The Love waves dominate the motions for the dip-slip case at all depths whereas the direct S arrivals are more noticeable in the strike-slip case, especially at the greater depths. These features may be understood in terms of vertical radiation patterns. The strike-slip pattern radiates most of the energy horizontally, which appears as direct body waves, while the dip-slip pattern tends to radiate energy vertically, where it can be trapped to form surface waves. The strike-slip A_4 coefficient from equation (16) is about 10 times larger than the dip-slip A_5 coefficient in both Langston's (1978) and Heaton's (1982) solution for the deep source. Heaton's shallow source is also dominated by the strike-slip solution but Langston's shallow source is about one-third composed of the dip-slip solution. For these reasons, we have conducted most of our sensitivity studies with the strike-slip case. Velocity domain seismograms generated from the above FD Green's functions are shown in Figure 2.13b. Seismograms for a flat-layered approximation to the deep basin structure are included in Figure 2.13a for comparison.

These synthetic seismograms for a flat structure are sensitive to the source depth in both amplitude and waveform. The shallowest source excites large, slow Love waves, and would make even larger, higher-frequency waves

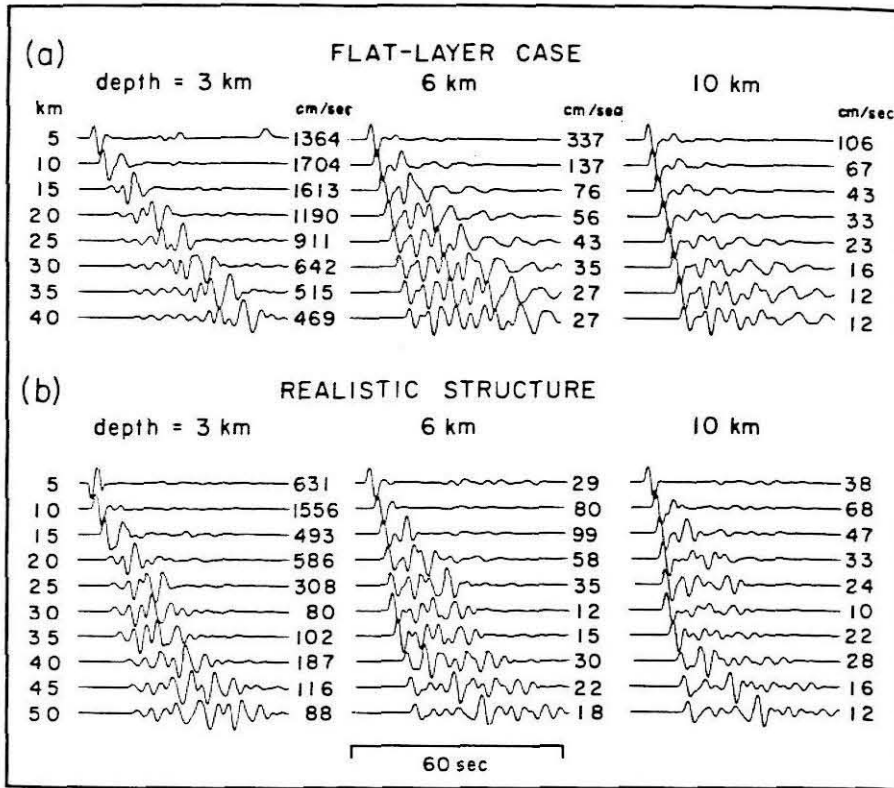


Figure 2.13 (a) FD seismograms for the transverse component of velocity for the model with flat layers of the thickness and velocities appropriate for the middle of the San Fernando basin in Figure 2.9, listed in Table 2.2. The source has a gaussian time function 4.0 seconds in width that is shown in Figure 2.14c. The mechanism is strike-slip and the moment is 10^{26} dyne-cm. The locations of the shallow, intermediate, and deep sources are indicated in Figure 2.9. Velocities are in cm/sec. (b) Finite difference velocity seismograms for the model shown in Figure 2.9. The source has the same gaussian time function 4.0 seconds in width as (a). The mechanism is strike-slip. The location of the shallow, intermediate, and deep depth sources are indicated in Figure 2.9.

were it not for the strong damping due to the Q of 25. Even considering the inefficiency of the shallow source in exciting radiation along this profile, 0.1×10^{26} dyne-cm of moment in the shallow source would suffice to generate waves as large as those observed. The shallow source creates such large waves for two reasons; first, the softer material near the surface allows larger velocities to develop for a given moment than the stiffer material at greater depth, and second, the shallower source can trap a larger portion of its energy as surface waves. The direct diving wave has a negligible amplitude compared to the surface wave for all but the two closest stations. The medium-depth source generates smaller seismic waves, and excites surface waves with a range of velocities. The direct arrival is distinct for all ranges, whereas the deep source produces predominantly a direct diving wave. Surface waves do not contribute much energy to the records for the intermediate and deep sources. It is clear that for this flat-layered geometry, the shallow source generates much more surface motion per unit moment than the intermediate and deep sources. The moments of $1-2 \times 10^{26}$ dyne-cm found by the studies in Table 2.3, placed at the intermediate or deep depth can roughly explain the peak velocities observed.

The waveforms from the more realistic structure, Figure 2.13b, are more complicated than in the flat-layered case. Sources at all depths can excite noticeable surface waves in both basins. This result arises because direct energy incident on the edges of the basin can be trapped by the basins much more efficiently than the direct waves can tunnel into the flat layers. The shallow source still excites larger motions on the surface, again largely because the slower medium generates larger amplitude waves, and also because the

shallow source is closer to the basin edge, allowing a larger percentage of its energy to be trapped. The source at 14 km depth produces seismograms very similar to those of the source at 10 km depth, except for a smaller amplitude, which is due to the faster velocity at the deeper depth.

The surface waves that are traveling within the San Fernando basin can, to some extent, tunnel across the Santa Monica mountains to enter the Los Angeles basin. Significant energy also must be reradiated as body wave energy when the surface waves reach the far side of the basins. Little energy reverses direction and travels back to the north in the basins. The peak amplitudes of the velocity traces are greater for the realistic structure than for the flat-layered structure in the San Fernando basin, but the reverse is true in the Santa Monica mountains. In the Los Angeles basin, the peak amplitudes are less than in the flat-layered case because the receivers are in the shadow of the mountains, for the case of 3 and 6 km deep sources. The 10 km deep source, however, excites the Los Angeles basin with a direct S wave, which is more efficiently converted to surface waves in the realistic than the flat-layered geometry.

Note that the seismograms for the 10 km source depth begin to show many of the characteristics of the data displayed in Figure 2.8, that is, reduced amplitude with simple direct pulses at the ridge and significant surface wave arrivals in each basin. The source at 6 km depth matches the data nearly as well, but has too much energy in surface waves compared to direct waves. For the rest of the paper we will consider only the point dislocation source at 10 km depth. Most probably, the source was actually finite, but most of the effect of source finiteness may be included in the source time

function. What cannot be included is most likely much less significant than the effect of the structure, which is the focus of this paper.

The FD seismograms in Figure 2.12 suggest that the body wave appears at the ridge with a time function very similar to the source time function. The waveform of the transverse component at the ridge station D068 is shown in velocity and displacement in Figure 2.14. The displacement trace shows two strong pulses of energy. Heaton's (1982) source model predicts a strong second arrival with a 4-second time delay, while Langston (1978) finds a value of 4.9 seconds. Both models appear to fit the observations at the ridge quite well. The relative amplitude ratio of the two pulses appear to favor the Langston source model, which is given in Table 2.3. One possible strategy at this point would be to add the secondary source and make adjustments in the source time description. Another approach that might be called an "empirical source model" is to assume that the displacement record D068 is the best possible source description in this particular direction and use it to predict the other seismograms. This empirical approach is adopted and the FD seismograms with the empirical source model are presented in Figure 2.15. The moment, which is difficult to control because the long-period information is absent from the data, is set so that the amplitude matches between the station D068 and the synthetic at that range. When a cluster of stations are at nearly the same range, only one representative trace is plotted.

In Figure 2.15, the agreement between the data and the FD seismograms is excellent at all but the very close-in ranges where the near-field assumptions break down.

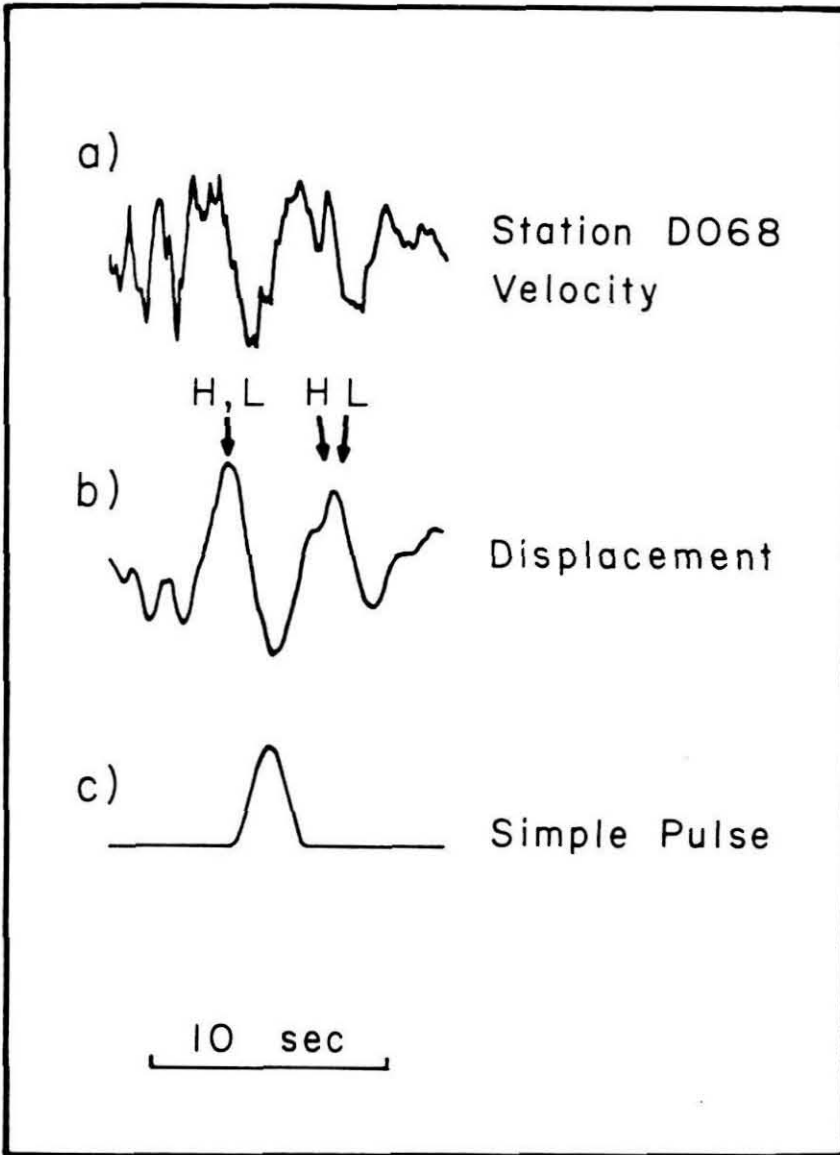


Figure 2.14 The calculation of an empirical source time function for the deep source. (a) shows the observed transverse velocity pulse at the Santa Monica mountains station D068. (b) shows the displacement pulse at station D068. Predictions of secondary arrivals by Heaton (1982) and Langston (1978) are indicated by the H and L above the trace. (c) shows the gaussian time function assumed in the construction of the synthetics shown in Figure 2.13.

Transverse Velocities With Empirical Source Time Function

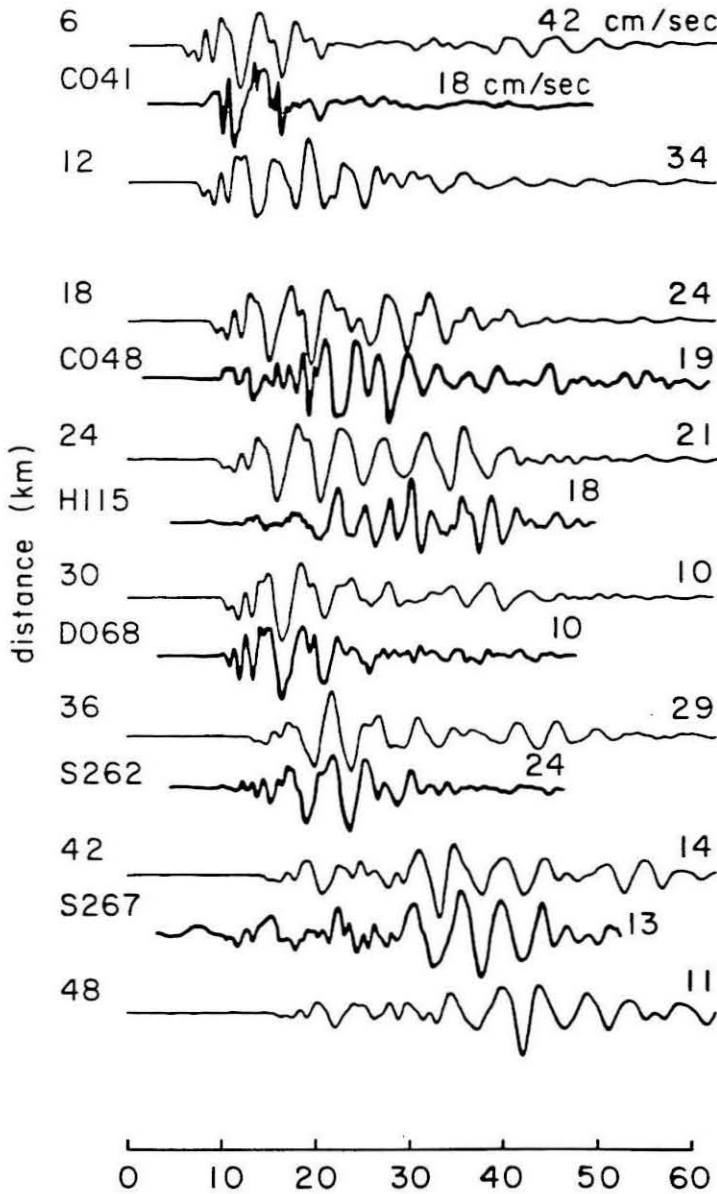


Figure 2.15 Comparison of filtered data with FD seismograms computed with the empirical time function shown in Figure 2.14 for the transverse component of velocity. The heavy traces show the data, with the station name to the left and the amplitude in cm/sec to the right. The light traces show the FD seismograms, with the range in km to the left and the amplitude to the right. The FD seismograms assume a point source at the location D (10 km depth) in Figure 2.9; they are computed with the structure shown in Figure 2.9, and a Q of 25 is assumed. The FD amplitudes are normalized so that the amplitude of the synthetic seismogram at the ridge station (30 km) matches that of station D068.

The P-SV motions can be simulated by constructing Green's functions as for the SH case except that three rather than two fundamental fault orientations are required. These responses for the assumed two-dimensional structure and 10 km deep source are given in Figure 2.16. As discussed earlier, the vertical radiation patterns strongly influence the relative body-wave to surface-wave ratios. The strike-slip A_1 , dip-slip A_2 , and 45° dip-slip A_3 factors in equation (16) are all significant for the deep source mechanisms of Heaton (1982) and Langston (1978). The A_3 or component actually dominates, as might be expected for a mostly thrust event, because A_3 is slightly larger than A_1 and A_2 , and the amplitudes of the Green's functions for A_3 are larger than those of A_1 and A_2 .

The FD seismograms are compared with the data for the vertical and radial components in Figures 2.17 and 2.18. Again, when a cluster of stations are at nearly the same range, only one representative trace is plotted. The amplitude of the synthetic seismograms is determined from the SH scaling described above. The match in timing is somewhat arbitrary since there is no absolute timing for the data.

The match in amplitude between the P-SV synthetic velocities and the data is good. In addition, the duration of shaking in the San Fernando basin and the waveforms at the start of the record in the Los Angeles basin are also well-modeled using the empirical time function. As in the SH case, the Santa Monica mountains produce a strong decrease in the amplitude of the velocity traces, and both basins apparently convert the direct waves into surface waves, Rayleigh waves in this case, at the edge nearest the source.

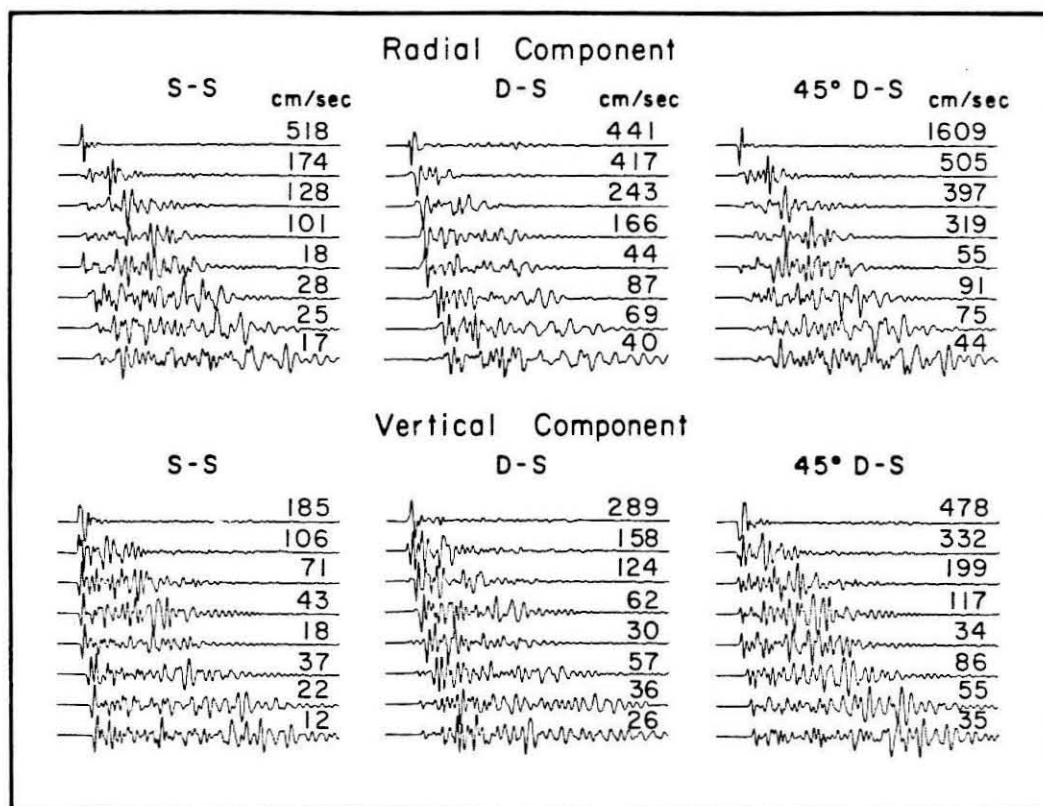


Figure 2.16 Vertical and radial Green's functions for the deep source, labeled D (10 km depth) on Figure 2.9. The strike-slip case corresponds to $A_1 = 1$, $A_2 = 0$, and $A_3 = 0$. The dip-slip case corresponds to $A_1 = 0$, $A_2 = 1$, and $A_3 = 0$. The 45° dip-slip case corresponds to $A_1 = 0$, $A_2 = 0$, and $A_3 = 1$. The moment for each Green's function is 10^{26} dyne-cm. The frequency content is limited mostly by the seismic Q of 25.

Vertical Velocity With Empirical Source Time Function

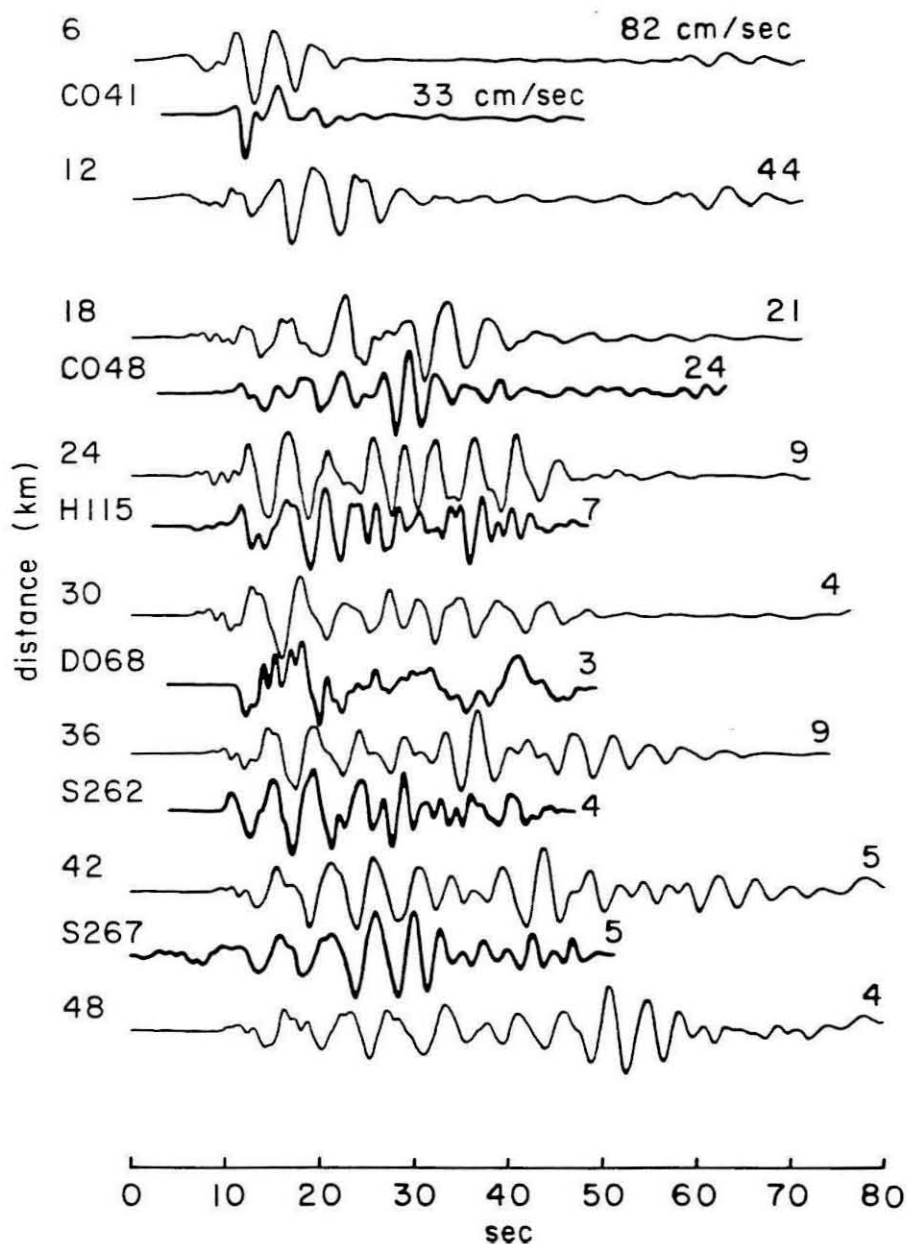


Figure 2.17 Comparison of filtered data with FD seismograms computed with the empirical time function shown in Figure 2.14 for the vertical component of velocity. The heavy traces show the data, with the station name to the left and the amplitude in cm/sec to the right. The light traces show the FD seismograms, with the range in km to the left and the amplitude to the right. The FD seismograms assume a point source at the location D (10 km depth) in Figure 2.9; they are computed with the structure shown in Figure 2.9, and a Q of 25 is assumed. The amplitudes of the FD seismograms are consistent with those for the transverse component in Figure 2.15.

Radial Velocity With Empirical Source Time Function

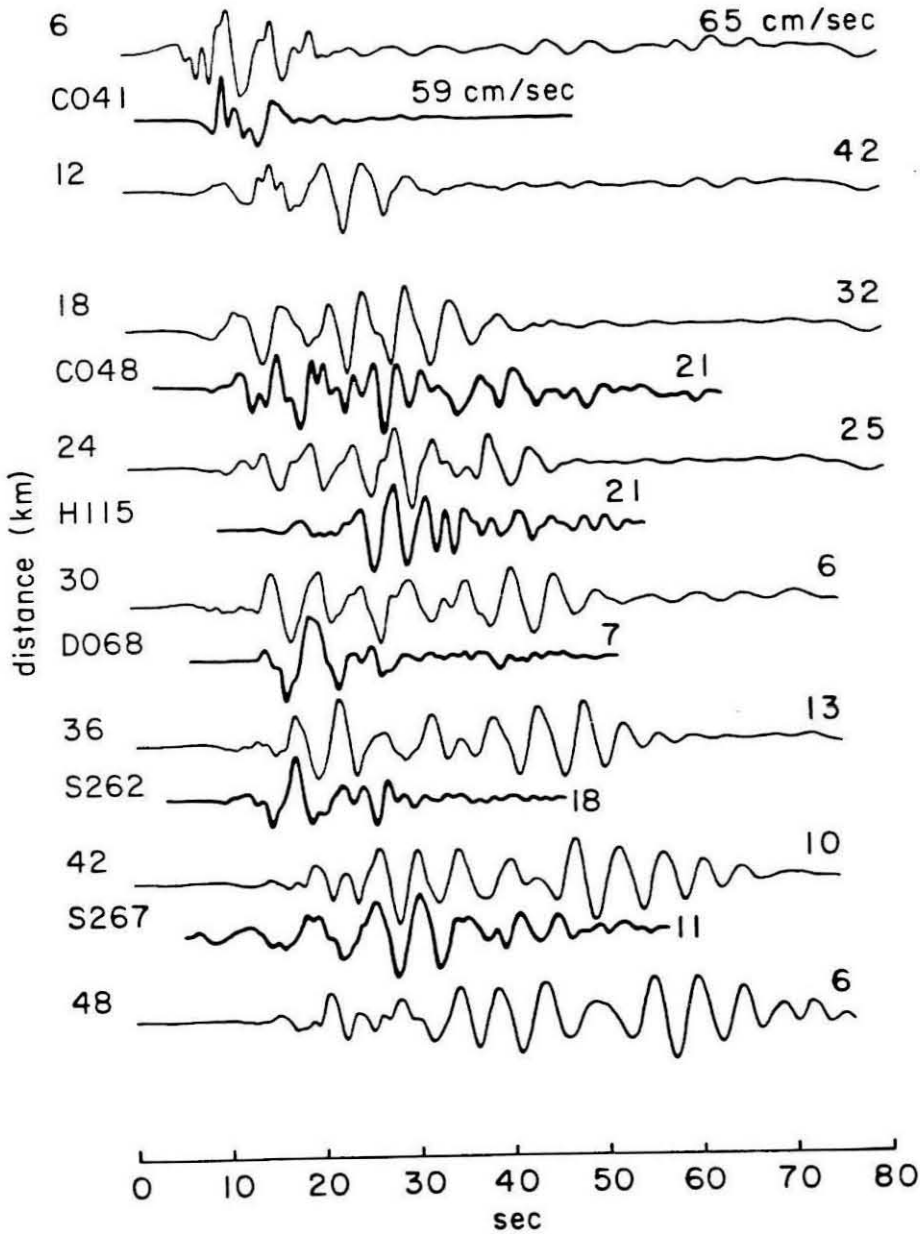


Figure 2.18 Comparison of filtered data with FD seismograms computed with the empirical time function shown in Figure 2.14 for the radial component of velocity. The heavy traces show the data, with the station name to the left and the amplitude in cm/sec to the right. The light traces show the FD seismograms, with the range in km to the left and the amplitude to the right. The FD seismograms assume a point source at the location D (10 km depth) in Figure 2.9; they are computed with the structure shown in Figure 2.9, and a Q of 25 is assumed. The amplitudes of the FD seismograms are consistent with those for the transverse component in Figure 2.15.

Only two troublesome problems appear in the forward modeling of the San Fernando records. First, the small amount of shallow moment release in our model is in conflict with observations of 1 meter of thrust motion measured at the surface (Alewine, 1974), as well as the suggestions of Heaton (1982), Langston (1978) and Alewine (1974) of significant shallow moment release. In our model, sources at between 6 and 14 km depths excite basins in a similar way, so it is only in the top 5 km that we would exclude significant moment release. The half-space model of Heaton (1982) and the layered model of Langston (1978) overestimate the velocity near the surface, so a smaller moment would serve to excite the same energy in the seismic waves given the correct lower velocities. Also, it is possible that the energy radiated from the shallow portion of the fault is absorbed by some mechanism such as decoupling of the two sides of the fault plane or very low Q in the region, but these explanations are not likely. The main point of this paper is that the relative amplitudes and duration of shaking across basins can be explained with FD modeling, and the details of faulting in our model are secondary.

The second problem may be seen in Figures 2.17 and 2.18, where the Rayleigh wave created in the San Fernando basin leaps across the Santa Monica mountains and has a much larger amplitude in the Los Angeles basin than is seen in the data. We have tried rather extreme structures such as more separation between the basins and different kinds of edges on the basins, but the Rayleigh waves simply are better at tunneling across the mountains than the Love waves, and it is difficult to match the data. Three-dimensional effects may be responsible for this problem. Since this profile skirts the west edge of the Los Angeles basin, the Rayleigh waves jumping the mountains will

be refracted into the slower material in the center of the basin and the amplitude of these Rayleigh waves at stations H118 and S267 may be small. An alternative explanation may be that the velocity model for the San Fernando basin has too thick a column of slow sediments. In the model, the same 3-5 second period surface waves are excited in both the San Fernando and Los Angeles basins, suggesting that the San Fernando basin model should have a thinner layer of slow sediments. In the data, it appears that the surface waves are shorter period in the San Fernando basin than the Los Angeles basin. If the two basins had distinctly different resonant frequencies, the surface wave from the San Fernando basin would not excite the Los Angeles basin as much.

The peak amplitude comparison between the data and the FD synthetics is summarized in Figure 2.19. The match is seen to be very good. We did not deviate from the velocity model found from Duke et al. (1971) to keep this as much of a forward-modeling exercise as possible. We feel as a forward-modeling exercise, this simulation has been successful.

2.4 The San Fernando earthquake: implications for estimating strong motions

In this section, we examine closely-spaced synthetic SH seismograms for the two-dimensional profile from San Fernando to Palos Verdes and regression curves for amplitude and duration. Then we study a reversed profile that assumes an event on the Newport-Inglewood fault rather than on the fault that broke in the San Fernando earthquake. In that case, different patterns of

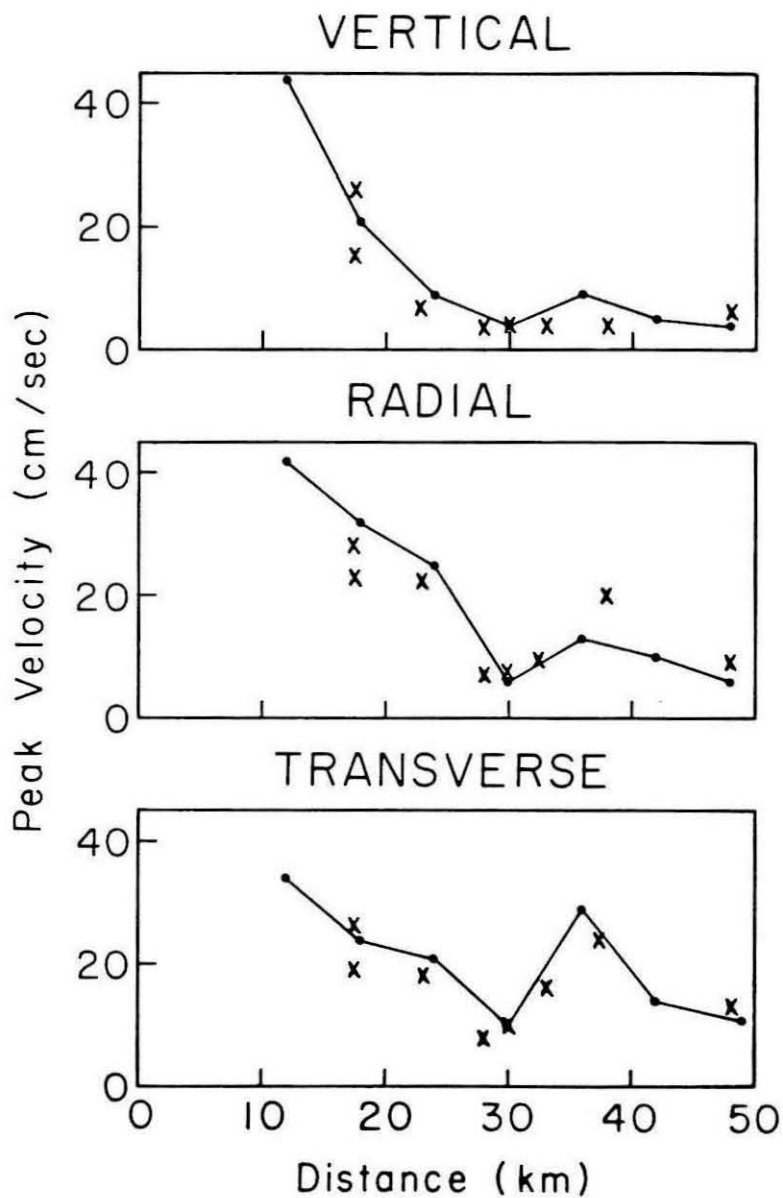


Figure 2.19 Peak velocity attenuation with distance. The filled circles show the peak velocity of the smoothed data versus offset. The line shows the attenuation for the FD simulation of the motions.

attenuation and duration of shaking result.

For insight into the creation and destruction of the surface waves at the edges of the basins, the envelope of the velocity seismograms is shown in Figure 2.20. In this and the rest of the figures, a sketch of the basins and mountains is included at the bottom for location. We use the same source location and empirical time function as we did for the previous synthetic seismograms. The first arrival in the seismograms displayed in Figures 2.15 and 2.20 is the direct SH wave. The direct wave advances slightly at the Santa Monica mountains because of the faster material at the surface. In both the San Fernando basin and the Los Angeles basin, the direct SH wave incident upon the edge of the basin nearest the epicenter produces a surface wave train (Love waves) that crosses the basin then converts back to body waves.

Some energy from the Love wave in the San Fernando basin converts to a body wave with a rapid apparent velocity across the Santa Monica mountains, then partially converts back to a surface wave in the Los Angeles basin. This arrival may be thought of as surface wave energy that has tunneled across the mountains. The surface wave generated by the direct SH pulse, however, is stronger than the tunneling surface wave for this source location and mechanism.

Duration of shaking and attenuation

Without a method for propagating the seismic energy across the laterally varying structure, one would have to resort to more empirical methods for determining the expected duration and amplitude of shaking. Joyner and Boore (1981) compile many velocity seismograms from earthquakes of a range

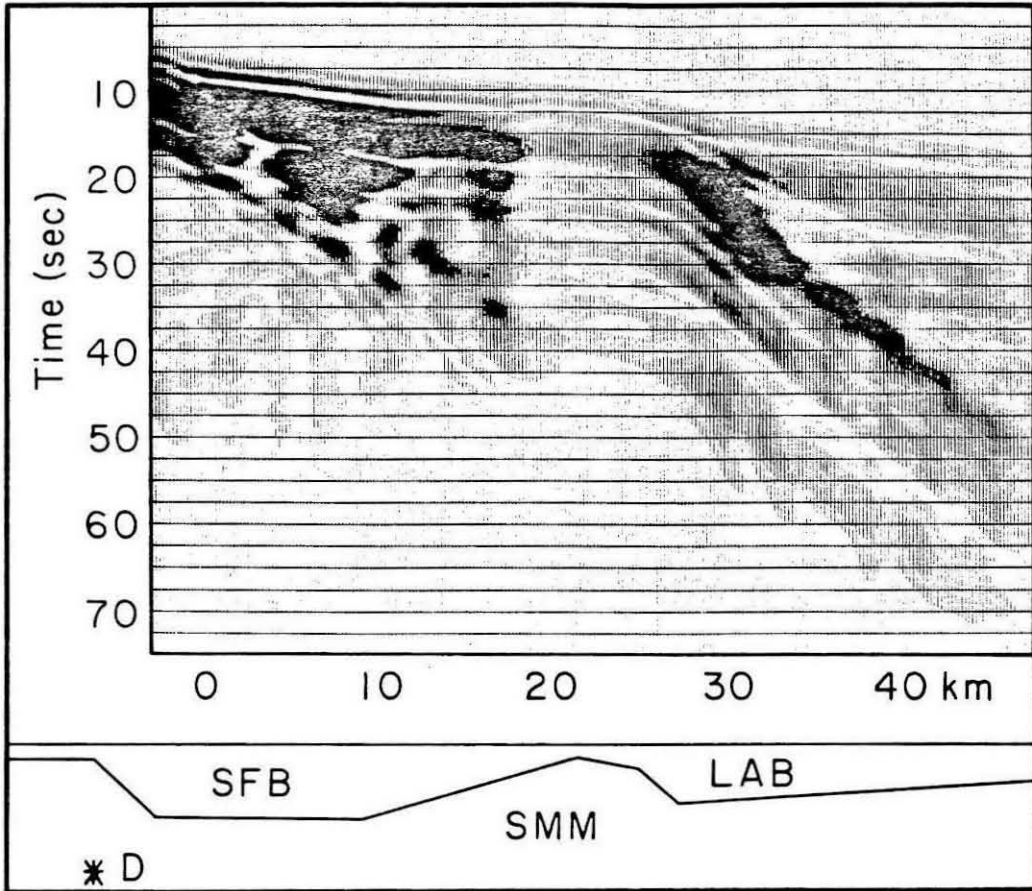


Figure 2.20 A seismic section of the envelope of the transverse component of velocity across the San Fernando and Los Angeles basins. The same source is used as in Figure 2.15. The major geologic structures are sketched below the section, where SFB indicates the San Fernando basin, SMM the Santa Monica mountains, and LAB the Los Angeles basin.

of sizes to determine an empirical law for the decrease in peak amplitude of seismic waves with distance from an earthquake. Figure 2.21 shows the observed fall-off in amplitude with distance for the radial and transverse components of the San Fernando records compared with Joyner and Boore's (1981) empirical velocity curves for hard rock and soft rock sites. Although the curves pass through much of the data, and the soft rock curve predicts the amplification in the San Fernando basin fairly well, the Los Angeles basin amplifies seismic waves about twice as much as predicted.

The data must be filtered before comparison with the FD seismogram amplitudes. The filtered and unfiltered data are compared in Figure 2.22, where it may be seen that filtering makes little difference. If filtered and unfiltered accelerations rather than velocities were being compared, significant differences would appear because the frequencies at which peak accelerations are observed are presently too high for the FD method to propagate the energy 50 km to the more distant receivers.

The comparison between the filtered data and the FD seismograms for the four depths of sources, B, D, I, and S, displayed in Figure 3 is shown in Figure 2.23. Sources at all four depths produce similar amplitude fall-off with distance, and the shallowest source produces the most motion for a given moment, as was noted in the last section. From Figure 2.23, it is difficult to distinguish at which depth most of the moment release occurred because the patterns are so similar.

The duration of shaking for large earthquakes has been examined by Triunac and Brady (1975). The shaking is defined to start once 5% of the total energy has arrived at the station, with the energy defined as the velocity

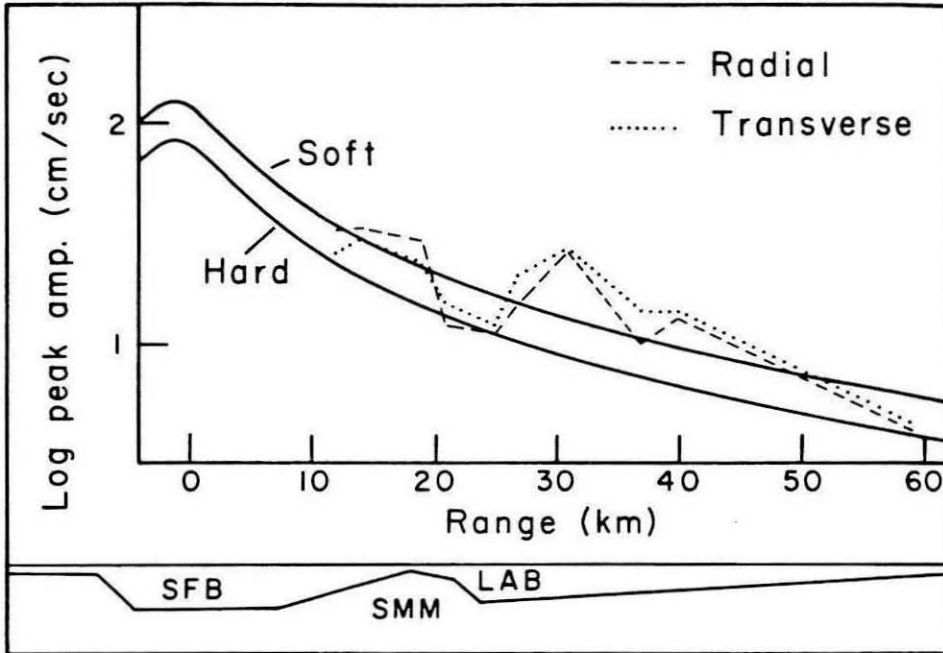


Figure 2.21 The peak amplitudes of the radial and vertical velocity traces plotted against the curve from Joyner and Boore (1982) for hard and soft rock sites. The major geologic structures are sketched below the section, where SFB indicates the San Fernando basin, SMM the Santa Monica mountains, and LAB the Los Angeles basin.

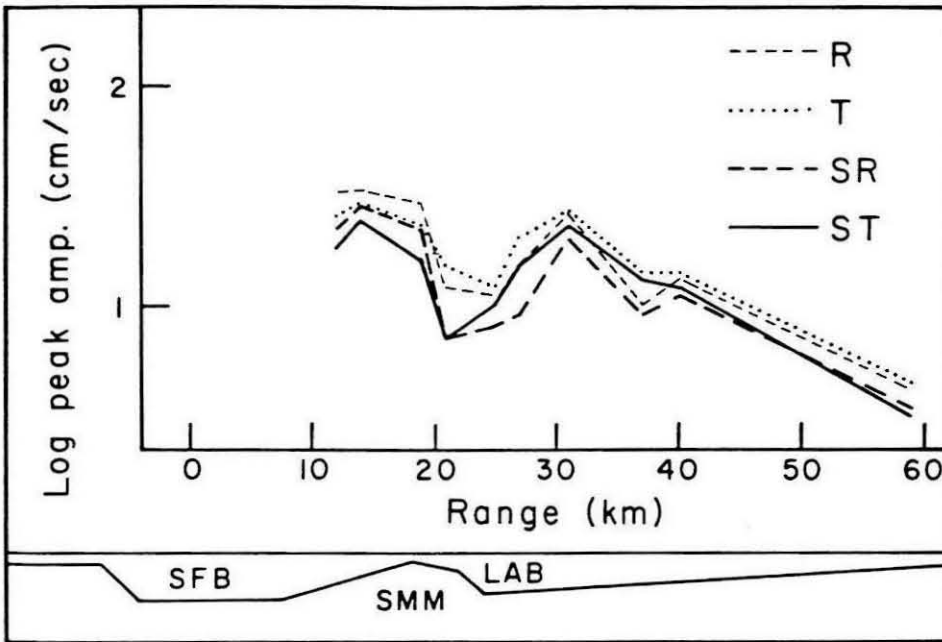


Figure 2.22 The peak amplitudes of the raw and smoothed transverse and radial velocity data are compared versus offset. The smoothed data have been convolved with a smooth pulse of half-width 0.2 seconds before measurement of the peak velocity because the FD synthetics are similarly smoothed. The major geologic structures are sketched below the section, where SFB indicates the San Fernando basin, SMM the Santa Monica mountains, and LAB the Los Angeles basin.

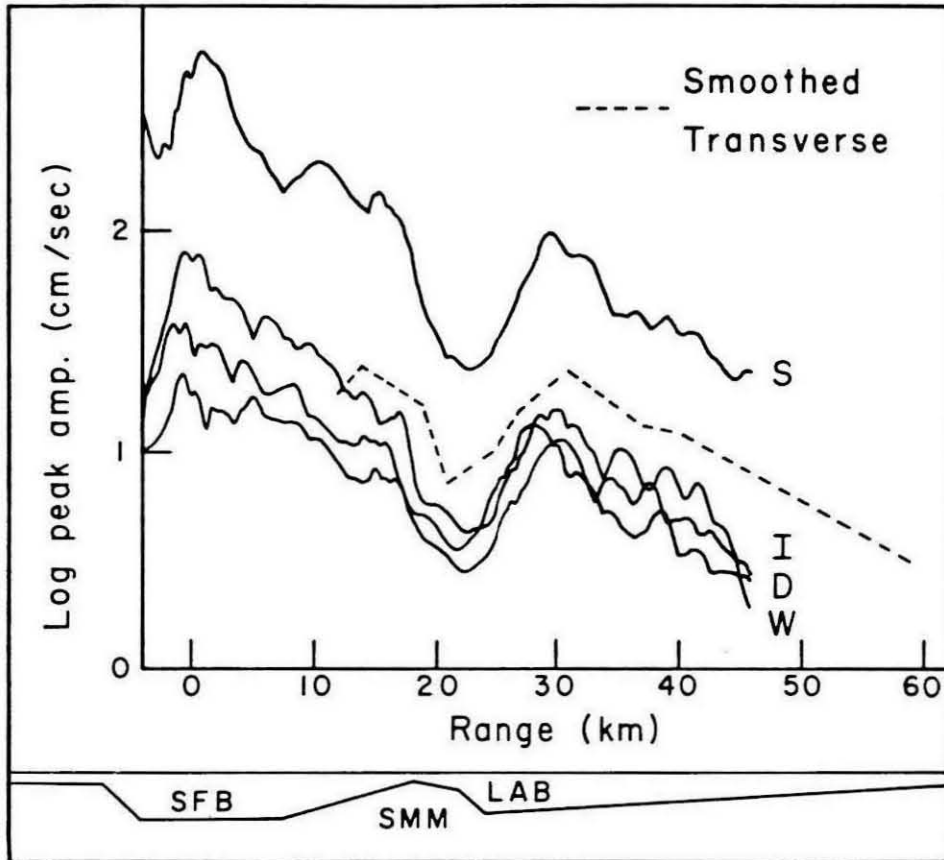


Figure 2.23 The peak amplitudes of the smoothed transverse data are compared with the peak amplitudes of the FD synthetics for the sources at points S, I, D, and W on Figure 2.9. The FD seismograms assume a moment of 10^{28} dyne-cm and use the empirical time function. The moment is held fixed as the depth varies, unlike in Figures 2.11 and 2.12, where the fault area times the slip was fixed. The mechanism is purely strike-slip. The major geologic structures are sketched below the section, where SFB indicates the San Fernando basin, SMM the Santa Monica mountains, and LAB the Los Angeles basin.

squared. The shaking is defined to stop once 95% of the energy has arrived. In Figure 2.24, the duration of shaking predicted by Trifunac and Brady (1975) is compared with the duration actually measured from the records. Two of the stations shown in Figure 2.8 (H115 and S267) have been omitted because the total length of the record is less than the duration of shaking of the neighboring stations. The shaking at the hard rock sites at Pacoima dam and in the Santa Monica mountains follows the hard rock curve of Trifunac and Brady (1975), but the shaking in the basin is seen to significantly exceed the predictions of the intermediate and soft rock curves.

Before the data and the FD seismograms are compared for duration of shaking, we prefer to redefine shaking as the time between the 10th and 90th percentiles in energy rather than between the 5th and the 95th percentiles, which tends to capture too much of the smaller reverberations late in the record, as may be verified by comparing the measured durations plotted in Figure 2.24 with the records shown in Figure 2.8. Also, the smoothed data is used for comparison with the FD simulations, but there is little difference in the duration of shaking between the raw and the smoothed data.

Figure 2.25 shows the comparison of duration of shaking between the smoothed data and the FD simulation. The 10 and 14 km depth sources closely mimic the pattern observed in the data, but the 3 and 6 km depth sources do not show the observed decline in duration of shaking in the Santa Monica mountains.

There is a dilemma if we use only a single point source to model the transverse data. The deep sources produce the correct pattern of amplitudes and duration of shaking, but the studies of Heaton (1982), Langston (1978),

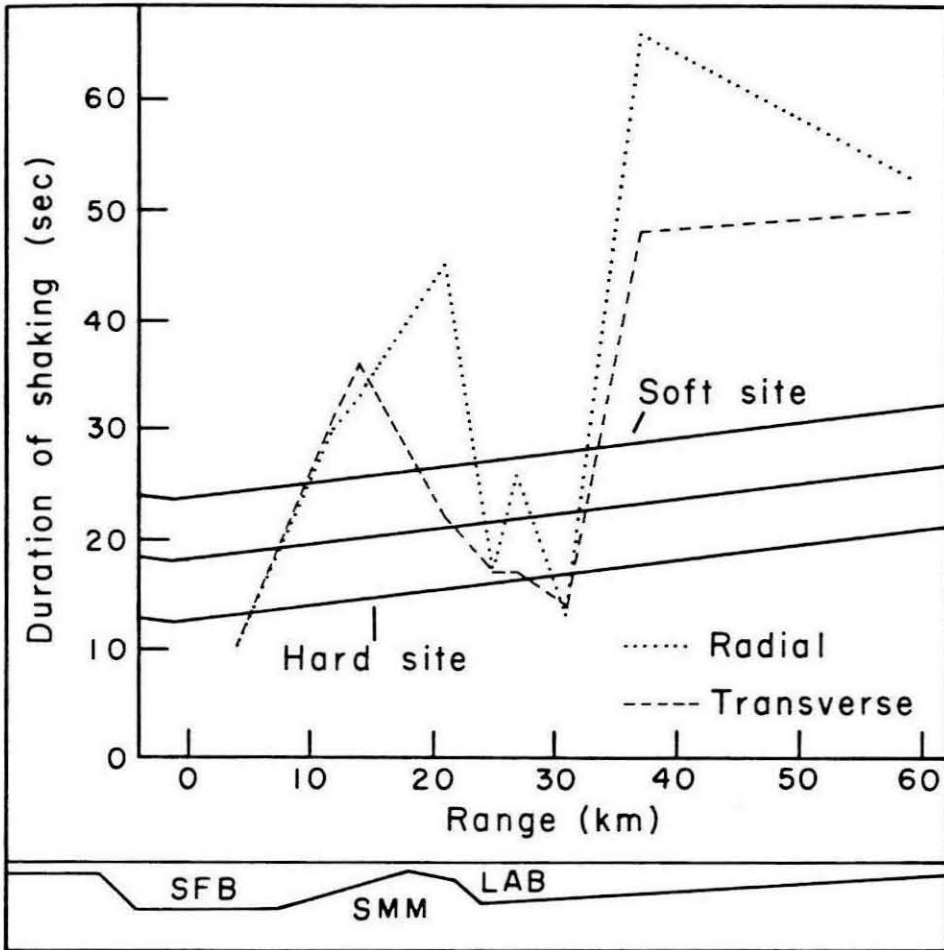


Figure 2.24 The duration of shaking measured with the definition of Trifunac and Brady (1975) for the smoothed radial and transverse components of velocity data are compared with the standard curves for soft, intermediate, and hard rock sites from Trifunac and Brady (1975). Three stations are omitted from this plot because the length of time recorded is very close to the estimated duration of shaking, which suggests that if the instruments recorded data longer, the estimated duration of shaking would be longer. The major geologic structures are sketched below the section, where SFB indicates the San Fernando basin, SMM the Santa Monica mountains, and LAB the Los Angeles basin.

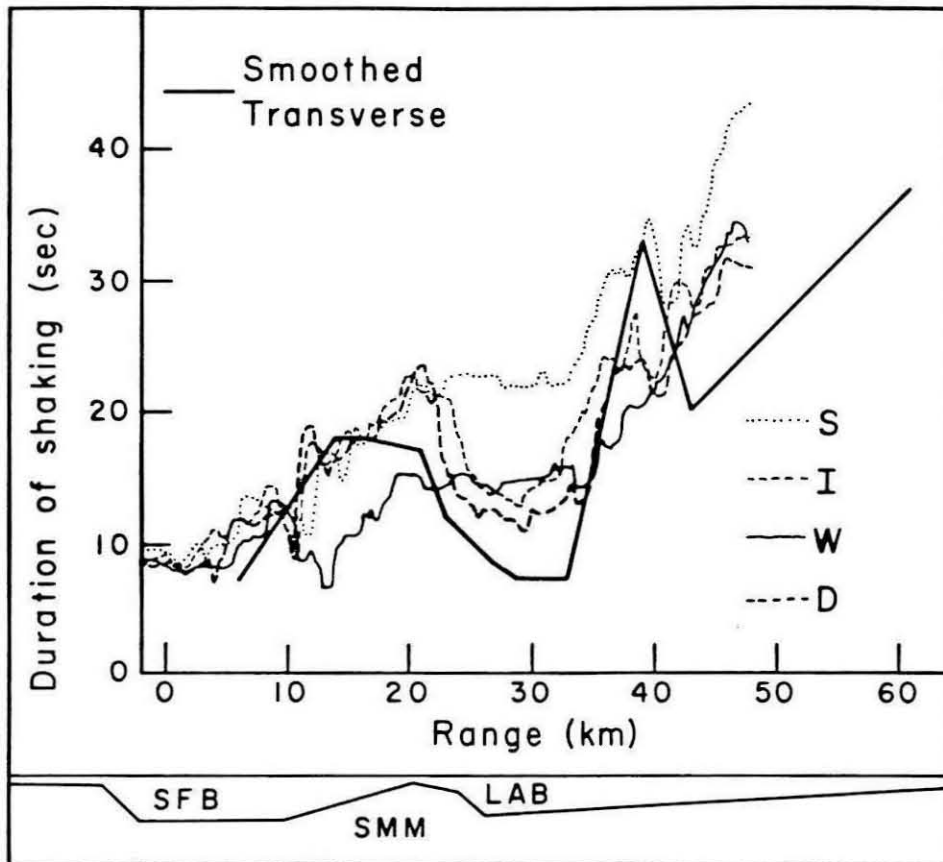


Figure 2.25 The duration of shaking for the smoothed transverse velocity data is compared with the duration of shaking for strike-slip point sources with the empirical time functions located at points S, I, D, and W on Figure 2.9. The shaking measure of Trifunac and Brady (1975), which started when 5% of the energy had arrived, and stopped when 95% of the energy had arrived is modified to a 10% / 90% criterion for this plot. The 5% / 95% criterion is undesirably sensitive to small amplitude coda at the end of the record. The major geologic structures are sketched below the section, where SFB indicates the San Fernando basin, SMM the Santa Monica mountains, and LAB the Los Angeles basin.

and Alewine (1974) find a component of shallow moment release. The shallow sources produce a duration of shaking at the Santa Monica mountains that is too long. Some small component of shallow moment release that contributes significantly to the motions in the San Fernando basin may be allowed, but is overwhelmed by the motions from the main, deeper part of the faulting in the mountains and in the Los Angeles basin.

We have shown that we can, in hindsight, predict the pattern of amplification and duration of shaking produced by an earthquake on the San Gabriel frontal fault system, namely, the San Fernando earthquake of 1971. If we had used a flat-layered velocity model, a similar pattern of amplitude and duration of shaking would be expected for any source in the area with the same epicentral depth. The only variation would be due to variations in mechanism. A more sophisticated scheme for predicting earthquake motions is to record earthquakes and explosions from NTS, for example (Rogers et al., 1984). One then computes average site responses and assumes that the site amplification is relatively independent of the range and azimuth to the seismic source. Next, we synthesize a source under the Los Angeles basin in the velocity cross-section given in Figure 2.9, effectively reversing the profile of strong motions examined above, and compare the pattern of amplification and duration to that of the San Fernando earthquake. To anticipate, we will find that the pattern of duration of shaking can be significantly different and the pattern of amplification is crudely the same, but can be in error by a factor of two for significant areas. This simulation is for the 0.1-1.0 Hertz frequency range, however, so further study would be necessary to extend to results to the 2-20 Hertz range that is of the most interest to earthquake engineers.

A seismic section of the envelope of the transverse component of velocity across the San Fernando and Los Angeles basins is shown in Figure 2.26 for the southern source. The empirical time function of Figure 2.14 is convolved with an impulsive strike-slip Green's function. The zone of low values at a range of about 38 km marks the hypocenter of the earthquake. The values are low there because the faulting mechanism is strike-slip, which has a node for both compressional and shear energy in the vertical direction. This southern source is between the Newport-Inglewood and the Palos Verde faults.

The direct shear wave is the most prominent arrival in the Los Angeles basin. A Love wave train that is created by conversions from the direct shear wave at the northern edge of the basin is the next most prominent arrival. The energy converts to surface waves at the edge of the basin rather than directly above the source. This is because the relatively flat layers above the source require energy to tunnel into the layers to form surface waves, but the abrupt edge of the basin bounces energy directly into surface waves in the basin, which is more efficient. The surface waves that traverse the San Fernando basin convert from the direct shear body waves at the edge of the basin nearest the source, as they did in the case with the source to the north.

The peak velocities produced by the FD simulation for the northern and southern sources divided by the peak velocity curve for a hard rock site from Joyner and Boore (1981) are shown in Figure 2.27. A moment of 2×10^{26} is assumed, and the Joyner-Boore curve uses a moment magnitude of 6.6 as is appropriate for the San Fernando earthquake. The recorded motions from the San Fernando earthquake are also shown. The sharp dip in the amplitude directly over the source in the Los Angeles basin is again due to the strike-slip

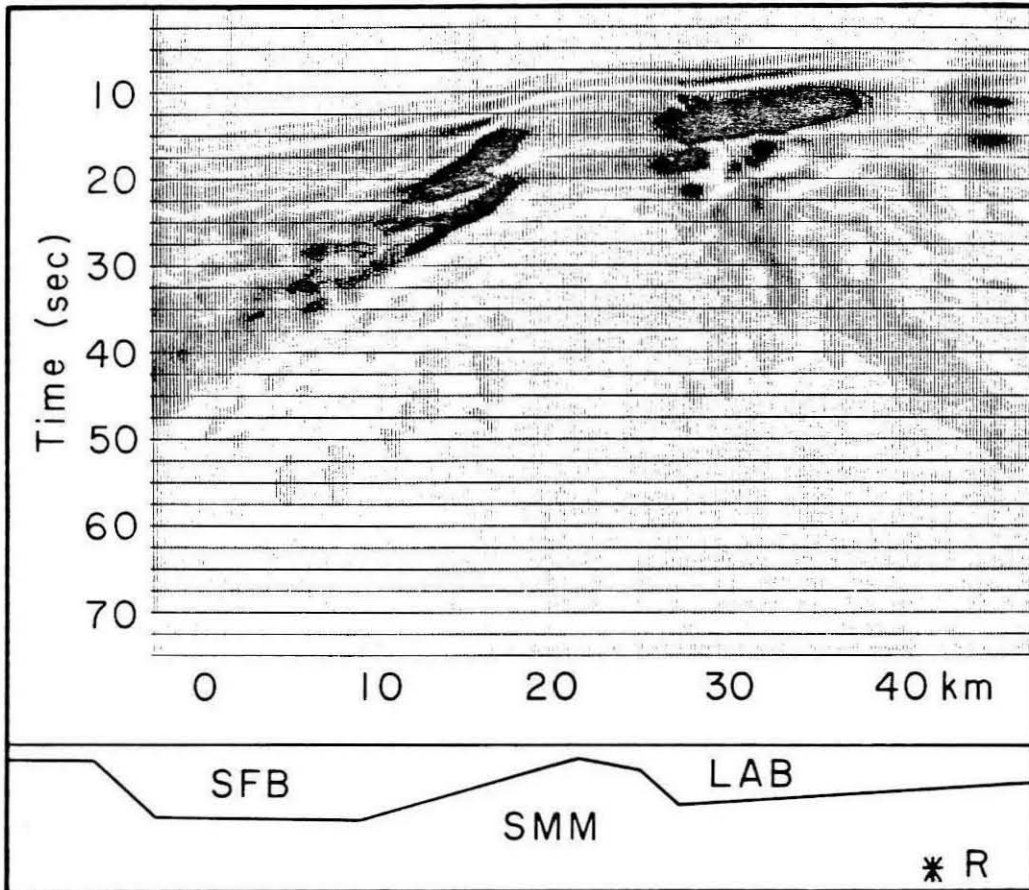


Figure 2.26 A seismic section of the envelope of the velocity across the San Fernando and Los Angeles basins. The source is at R on the right side of the cross-section and has a strike-slip mechanism. The major geologic structures are sketched below the section, where SFB indicates the San Fernando basin, SMM the Santa Monica mountains, and LAB the Los Angeles basin.

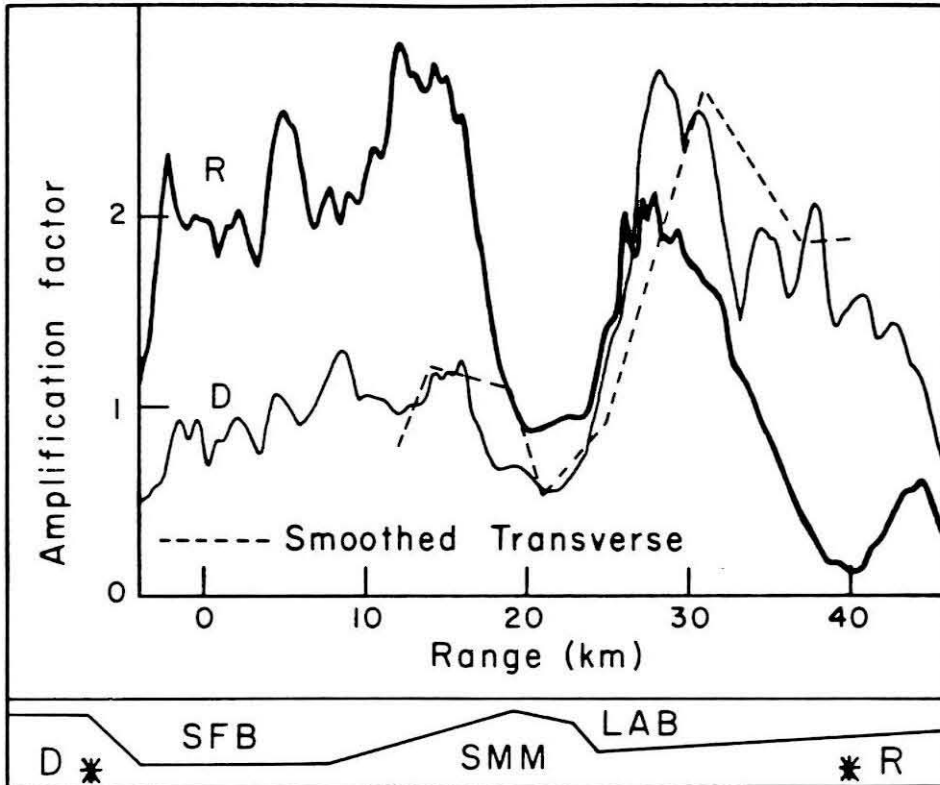


Figure 2.27 The amplification factors are shown versus location in the profile. The amplification is the peak amplitude for the profiles corresponding to sources R and D divided by the predicted values from the hardrock curve of Joyner and Boore (1982). The peak amplitudes in the smoothed velocity records of the San Fernando earthquake are shown by the dotted line. A moment of 2×10^{26} dyne-cm and a purely strike-slip mechanism is assumed and the empirical time function is used. The major geologic structures are sketched below the section, where SFB indicates the San Fernando basin, SMM the Santa Monica mountains, and LAB the Los Angeles basin.

mechanism. The mechanism is also responsible for the dip in the curve for the northern source as it goes off the plot to the left. The origin for the horizontal axis corresponds to the surface break of the fault, as is defined for Joyner and Boore's (1981) peak velocity curve, although the source is placed 10 km further north in the FD simulation. The absolute amplitude is somewhat arbitrary because here we are using a purely strike-slip mechanism, while above we used a mechanism found by Langston (1978) that radiates SH energy in this azimuth with only half the efficiency of the pure strike-slip case.

The curves show that in the case of the source to the north of the basins, the San Fernando basin is more weakly excited, but the Los Angeles basin is more strongly excited than in the case of the source to the south. This is partly due to radiation pattern, but is also due to the ease with which the edge of a basin closest to the seismic source can trap body waves into surface waves. For both sources, the edge of the basin just on the far side of the Santa Monica mountains registers the strongest peak velocity. This phenomenon of dipping layers trapping body waves is discussed in more detail in Section 2.2 above.

The mountains in both cases shows a drop by a factor of 1.5 to 5 in peak velocity over the basins to either side. The data from the San Fernando earthquake clearly follow the simulation of the source to the north, but bear little resemblance to the curve for the source to the south.

A comparison of the duration of shaking for the profiles with the source to the north and to the south are shown in Figure 2.28. The duration is again defined to start when 10% of the energy has arrived and to stop when 90% of the energy has arrived. The regions of short duration consist not only of the

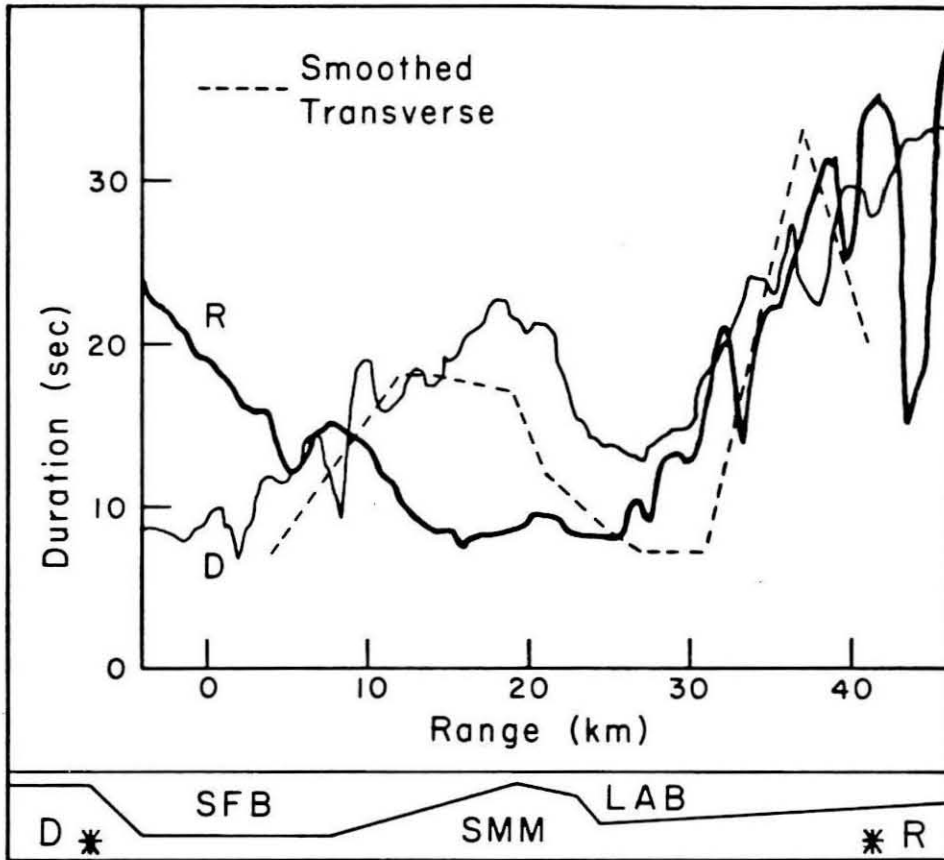


Figure 2.28 The duration of shaking using the 10% / 90% measure defined in the text for the profiles corresponding to sources R and D in Figure 2.9 are shown versus location in the profile. The duration of shaking in the smoothed velocity data is shown by the dashed line. A purely strike-slip mechanism is assumed for both events and the empirical time function is used. The major geologic structures are sketched below the section, where SFB indicates the San Fernando basin, SMM the Santa Monica mountains, and LAB the Los Angeles basin.

Santa Monica mountain sites, but also of the sites a short way into the basins where the surface waves have not yet had much chance to disperse or separate from the shear direct wave. The curves are similar for the Los Angeles basin, where the surface waves are created at the northern end in each case. The trends for the San Fernando basin are opposite, however, since for the northern source the surface waves initiate at the northern end, and for the southern source the surface waves initiate at the southern end of the basin. Again, the data follows the curve for the northern, but not the southern source.

In summary, although there are similarities between the patterns for the two sources, there are also important differences. In the worst case, the southern end of the San Fernando basin, the duration predicted from the northern source is 22 seconds while the computed duration for the southern source is 9 seconds and the predicted amplification is a factor of 1 while the computed amplification is more than 2.5. The concept of site response, therefore, needs to be generalized to include both the location of the site and the location of the source.

2.5 Conclusions

Once the path effects are known, source characteristics may be examined with more confidence. For the Borrego Mountain event, the teleseismic and long-period El Centro records may both be explained primarily by a single point dislocation near a depth of 8 km.

The strong motions recorded within the San Fernando and Los Angeles basins during the San Fernando earthquake of 1971 can be largely understood by forward modeling with teleseismically determined source parameters through known structure with only two-dimensional variations in velocity and density. This modeling will accept less moment release shallower than the 5 km depth than has been suggested in some previous studies, but this inconsistency might be reconciled if the fully three dimensional structure appropriate for closed basins is used in the FD calculation. The dramatic differences between using the laterally varying structure of Duke et al. (1971) and a flat-layered structure render it impossible to fit the data from the San Fernando earthquake with a flat-layered model.

Strike-slip sources tend to produce stronger direct body waves and weaker surface waves relative to dip-slip and 45° dip-slip sources. The geometry of the basin structure is also important in determining the attenuation of peak velocity along a profile. The mountains shadow the basins behind them against shallow surface waves, but the edges of the basin nearest the earthquake tends to convert body waves again to shallow surface waves. The source depth of the earthquake is less important than for the flat-layered case in determining the duration of shaking and attenuation of peak amplitude with distance. Basins with sharp edges tend to generate some back-scattered surface waves; basins with gradual edges have negligible back-scattered energy.

An earthquake to the south of the basins, which would correspond to an event on the Newport-Inglewood or Palos Verdes faults, shows significant differences in patterns of peak velocity and duration of shaking compared to an earthquake to the north, where the San Fernando quake was located. The

duration of shaking and peak velocity for a given site varies between sources at the two different azimuths by up to a factor of two.

A more systematic study of the effects of these basins on motions from earthquakes at various locations may be warranted. This study uses energy with 1-10 second periods, however, so some care must be taken to translate these results to the higher frequencies of interest to earthquake engineers.

Chapter 3

Application to modeling the strong motions of the explosion Milrow

3.1 Introduction

The effect of shallow station structure and lateral velocity variation are investigated for records of the Amchitka blast Milrow. The differences between the Meuller-Murphy, Helmberger-Hadley, and von Seggern-Blandford reduced displacement potential (RDP) source representations are small compared to the differences between using various possible velocity structures.

3.2 Effects of laterally varying structures

We will use the corrected source of Section 1.7 to investigate the effect of structure on the records of an explosion on Amchitka Island, which is near the Aleutian Islands in the Pacific ocean. Burdick (1984) shows that the records from the explosion Milrow for the stations shown in Figure 3.1 can be modeled fairly well with a layered structure. It is instructive to investigate the effect of several perturbations to the layered model by the FD method.

First, the FD method with the uncorrected explosive source of Section 1.2 is compared with the GRT plus modes results and those of the wavenumber-frequency numerical integration (WI) approach (Apsel, 1979) in Figure 3.2.

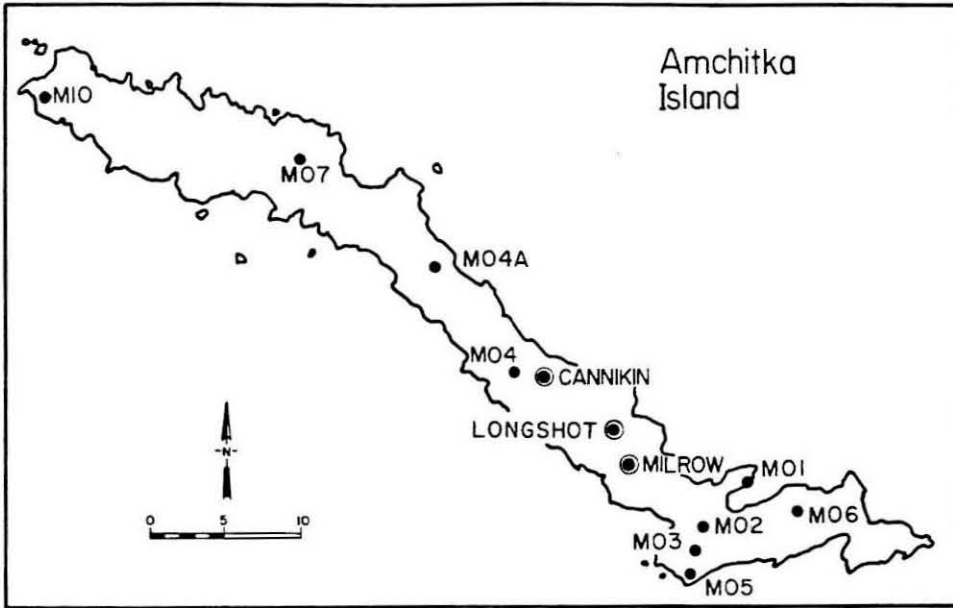


Figure 3.1 Location of the Amchitka nuclear test MILROW and of the near-field strong motion instruments deployed.

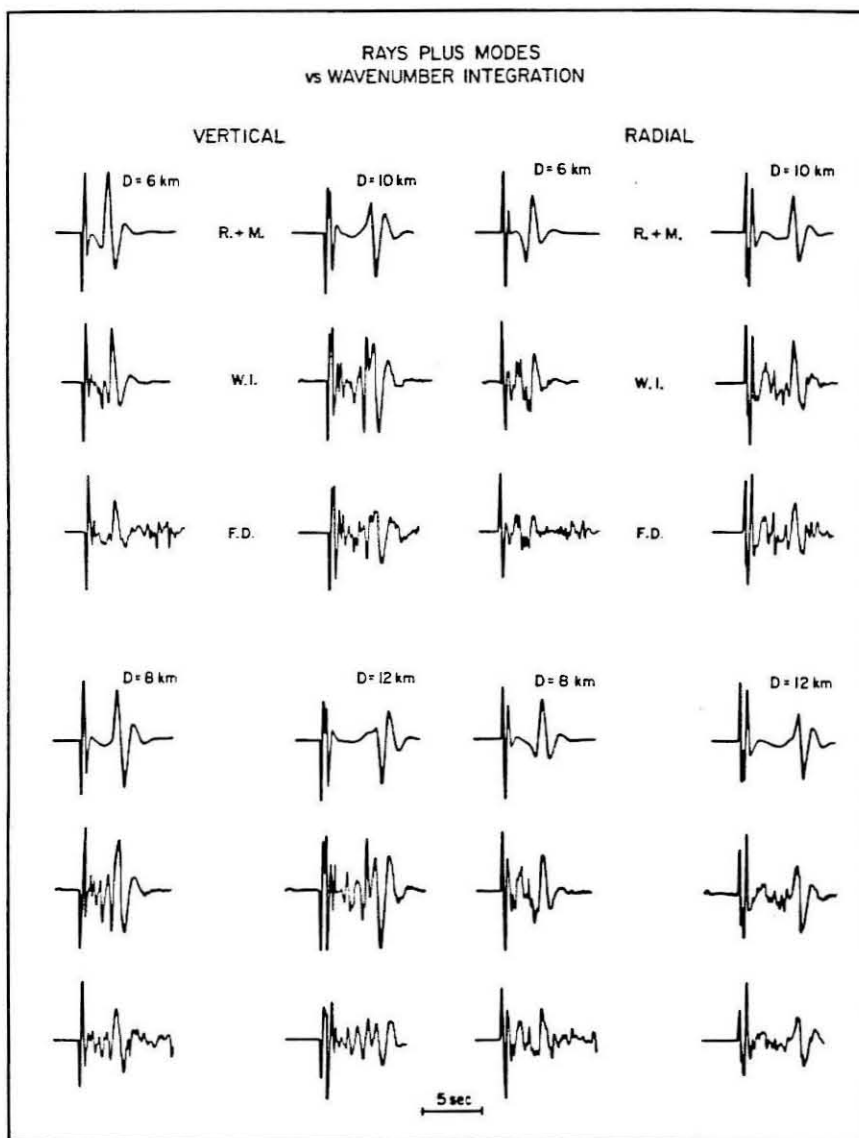


Figure 3.2 Comparison for layered velocity model listed in Table 1.2 of the results from the generalized rays plus modes methods, the wavenumber integration method, and the finite difference method. The source time function is from Helmberger and Hadley (1981) with corner frequency $K = 9.0$ Hz and overshoot parameter $B = 1.0$.

The P-wave crustal model, given in Table 1.2, consists of 9 layers derived by Burdick (1984) by fine-tuning the model proposed by Engdahl (1972). This model predicted the P-wave travel times well. The S-wave velocity structure, which is also given in Table 1.2, was added to model the Rayleigh wave arrivals by Burdick (1984). The RDP (reduced displacement potential), which is a source time function, of Helmberger and Hadley (1981) is used. In this section, the corner frequency parameter, K , is set at 9 sec^{-1} and the overshoot parameter B is set at a value of 1.

The seismograms shown in Figure 3.2 are synthetic velocity records for ranges of 6, 8, 10 and 12 km. This spans the range of distances for which there are records from Amchitka. The waveforms of the WI and the GRT plus modes seismograms match for both the body and surface wave pulses and the relative amplitude and timing of the two methods agree. The waveforms of the body waves and the surface waves match well between the FD and the WI methods. The amplitudes of the body waves are too large relative to the surface waves for the FD method. This is an artifact of using a 2-D rather than 3-D wave equation, as discussed in Chapter 1.7.

Orphal et al. (1970) displays geologic cross-sections from the blast to the various stations, and reports density and shear and compressional wave velocities for rocks from Amchitka. The two models tested below are plausible given the available information about Amchitka structure.

The effect of soft and hard rock sites as compared with the flat-layered model is investigated in Figure 3.3. The soft material has compressional wave velocity $\alpha = 2.0 \text{ km/sec}$, shear wave velocity $\beta = 1.0 \text{ km/sec}$, and density $\rho = 1.8 \text{ g/cm}^3$, the hard material has $\alpha = 4.6 \text{ km/sec}$, $\beta = 2.3 \text{ km/sec}$, and ρ

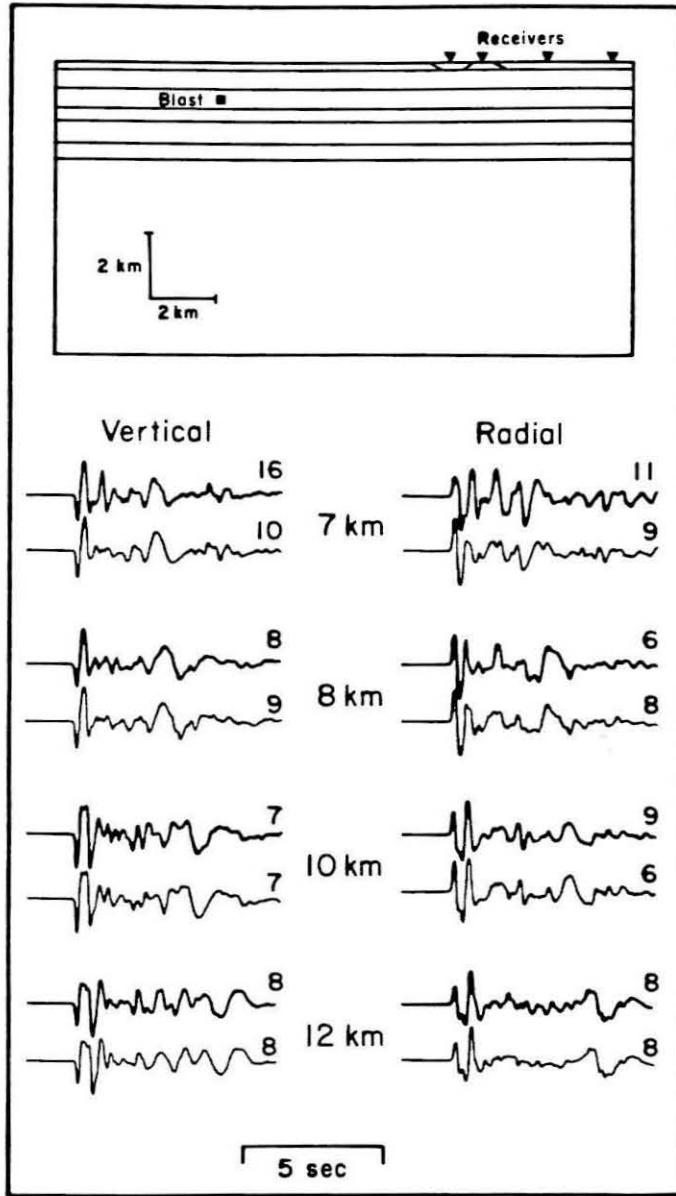


Figure 3.3 FD simulation of the effect of a soft rock site next to a hard rock site. Synthetic velocity seismograms at ranges of 7, 8, 10, and 12 km (heavy lines) are compared with those from the flat-layered model (light lines). The soft and hard rock sites are at ranges of 7 and 8 km, respectively. Soft site material has α of 2.0 km/sec, β of 1.0 km/sec, and ρ of 1.8 g/cm^3 , and hard site material has α of 4.6 km/sec, β of 2.3 km/sec, and ρ of 2.3 g/cm^3 . The model is displayed above the traces and the layering is the same model described in Table 1.2.

$= 2.3 \text{ g/cm}^3$, and the rest of the layer, which is 200 meters thick, has $\alpha = 3.4 \text{ km/sec}$, $\beta = 1.7 \text{ km/sec}$, and $\rho = 2.3 \text{ g/cm}^3$. The rest of the layers are the same as those listed in Table 1.2. The amplitude at the receiver on the soft site is a factor of 1.45 larger than at the receiver in the same position in the plane-layered model. A simple conservation of energy argument, ignoring the transmission coefficient into the slow layer, would predict an amplification of $(v_2 \sqrt{\rho_2}) / (v_1 \sqrt{\rho_1}) = 1.9$, where v_i is velocity and ρ_i is density, and 1 refers to the slow medium and 2 refers to the top layer of the plane-layered model. When the loss in transmission into the slow material is considered, the observed amplification factor agrees with the simple prediction. The particle motion is also more vertical than in the flat-layered case for the receiver at 7 km as the ray is more refracted due to the greater velocity contrast. Reverberations and conversions in the slow media may be seen 1 to 2 sec after the initial pulse.

At the station on the faster material, the amplitude is smaller by a factor of 1.2 compared to the simple prediction of 1.4, before correction for transmission, so the estimate does not work as well. Other factors, such as focusing, diffraction, and free-surface interaction may be important. The direct waves and longer-period surface waves appear unchanged at the ranges of 10 and 12 km, which are beyond the local station structures.

The best guess for the structure between the blast and station M05 inferred from Orphal et al. (1970) is used to generate the comparison shown in Figure 3.4, where each letter is translated into media parameters in Table 3.1. The same velocity model is used below the source as in the layered model, which results in similar waveforms in the body-wave arrival. This similarity is

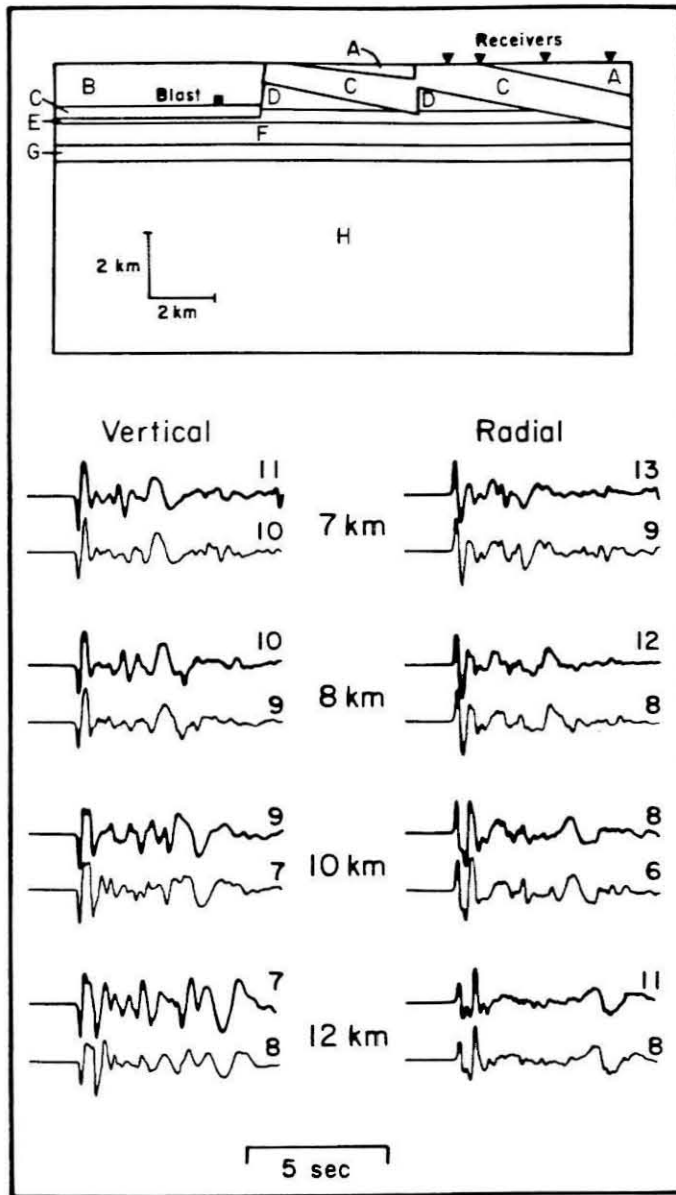


Figure 3.4 FD simulation of the effect of the cross-section derived from Orphal et al. (1970) for station M05. Synthetic velocity seismograms at ranges of 7, 8, 10, and 12 km (heavy lines) are compared with those from the flat-layered model (light lines). The model is displayed above the traces, and the velocities and densities which correspond with the letters A-H are given in Table 3.1.

Table 3.1 : Velocities in faulted Amchitka model

Letter	P-wave Velocity	S-wave Velocity (km/sec)	Density (km/sec)
A	3.4	1.7	2.0
B	3.4	1.7	2.1
C	3.7	1.9	2.1
D	4.4	2.2	2.4
E	4.6	2.3	2.5
F	4.9	2.8	2.6
G	5.1	2.9	2.7
H	5.9	3.3	2.7

because the waveforms are quite sensitive to the structure where the rays bottom. The amplitudes fluctuate by up to 25% on the vertical component and by up to 50% on the radial component. About 30% more amplitude, which translates to 70% more energy, is converted into the surface wave by the structures which dip down away from the source. This tendency of dipping layers to convert body waves to surface waves is examined above in Chapter 2.2. Derivation of a relatively detailed flat-layered model as was done by Burdick (1984) may help to understand the wave propagation involved, but should not be taken to represent the detailed structure of the earth.

Shallow structure is seen to affect the amplitude of body waves as well as surface waves. These effects are difficult to model deterministically because the structures are poorly known. Shallow structure may well contribute to the misfit presented below between the synthetic seismograms and the data.

3.3 Effects of varying source models

In this section we will show that for the data we are using, structure has more effect in determining the amplitudes and shaping the waveforms than the reduced displacement potential (RDP) used. Several RDP functions have been proposed, but in this section we will show that no one source model significantly outperforms the others for the near-field body and surface waves in the case of the explosion Milrow. The source of Helmberger and Hadley (1981) (H-H) was described above, but the sources of von Seggern and Blandford (1972) (vS-B) and Mueller and Murphy (1971) (M-M) are also frequently

used in the study of explosions.

Von Seggern and Blandford (1972) postulate a source given by

$$\Psi(t) = \Psi_{\infty} \left[1 - e^{-K' t} (1 + K' t - B' (K' t)^2) \right], \quad (10)$$

where Ψ_{∞} is the source strength, and K' and B' are corner frequency and overshoot parameters similar to K and B in the H-H source.

Meuller and Murthy (1971) postulate a source most easily expressed as a convolution (Barker et al., 1985):

$$\Psi(t) = \frac{r_{el} V_p^2}{4 \mu} P(t) * F(t) \quad (11)$$

where the $*$ indicates convolution and $P(t)$ and $F(t)$ are as follows:

$$P(t) = ((P_{0S} - P_{0C}) e^{-\alpha t} + P_{0C}) H(t) \quad (12)$$

and

$$F(t) = \frac{\sin(bt) e^{at}}{\beta b}. \quad (13)$$

Furthermore,

$$\text{elastic radius } r_{el} = 149,000 \frac{Y^{0.33}}{(h/100)^{0.42}}$$

$$\text{cavity radius } r_c = 3140 \frac{Y^{0.29}}{(h/100)^{0.11}}$$

$$\text{dynamic cavity pressure } P_{0C} = 0.8 \mu \left(\frac{r_c}{r_{el}} \right)^3$$

$$\text{static cavity pressure } P_{0S} = 1.5 \rho g h$$

and

$$\alpha = 1.5 \omega_0 = \frac{1.5 r_{el}}{V_p}$$

$$\beta = \frac{\lambda + 2\mu}{4\mu}$$

$$a = \frac{-\omega_0}{2\beta}$$

$$b = \frac{\omega_0}{\beta}(\beta - 0.25)^{0.5}$$

where Y is the yield in kilotons, h is the source depth, ρ is the density, V_p is the compressional wave velocity, and λ and μ are Lamé's constants. All parameters except the yield are in cgs units.

The parameters used for the three sources are given in Table 3.2. The M-M source has no free parameters and the parameters for the other two sources are determined from teleseismic body and surface waves by Lay et al. (1984).

The far-field displacement time functions for the three sources are shown in Figure 3.5a. There is little difference between the three traces. The RDP functions are plotted in Figure 3.5b, and the level of the permanent offset, Ψ_∞ is 1.4×10^{11} for the H-H and vS-B sources and 2.4×10^{11} for the M-M source. Figure 3.5c shows the spectra of the displacement time histories. The spectra are similar except that the M-M source has a higher long-period level, as is also seen in Figure 3.5b.

The data are compared to FD seismograms computed for the M-M, vS-B, and H-H sources in Figures 3.6 and 3.7. The FD seismograms are computed with the best guess of the structure from Orphal et al. (1970) by the method described above with the correction term. The various source time functions

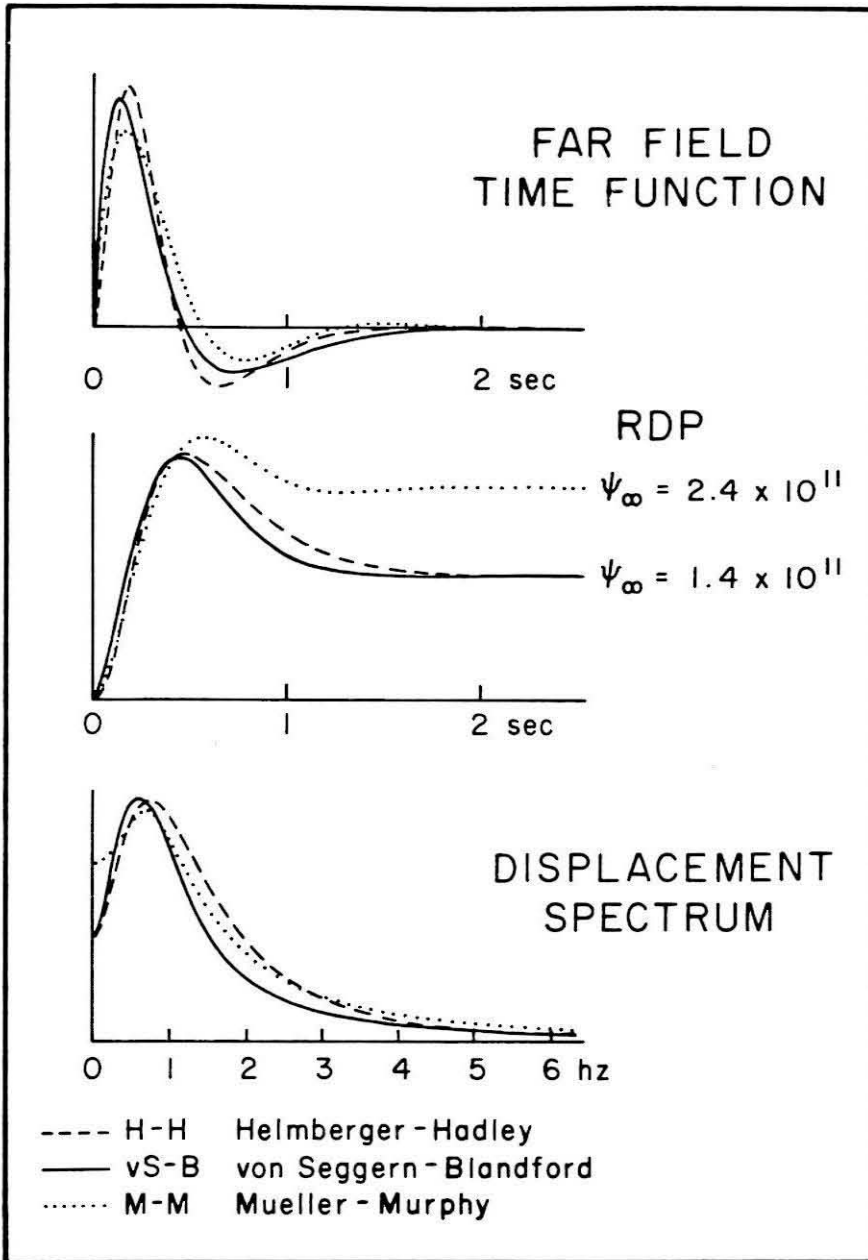


Figure 3.5 Comparisons of the Helmberger-Hadley, Mueller-Murphy, and von Seggern-Blandford RDP functions. (a) shows the time derivative of the RDP, which is the far-field displacement time function for the 3 sources. (b) shows the RDP's of the 3 sources. The long-period asymptote of the RDP is the Φ_{∞} of the source. (c) shows the amplitude spectra of the far-field displacement time functions for the 3 sources. The correct relative amplitudes are shown. The parameters used in the RDP functions are listed in Table 3.2.

Table 3.2 : RDP parameters

Helmberger and Hadley (1981) source

$$K = 8.0$$

$$B = 1.0$$

$$\Psi_{\infty} = 1.4 \times 10^{11}$$

Von Seggern and Balndford (1972) source

$$K' = 5.2$$

$$B' = 2.5$$

$$\Psi_{\infty} = 1.4 \times 10^{11}$$

Meuller and Murphy (1971) source

$$Y' = 1000 \text{ Kt}$$

$$h = 1200\text{m}$$

$$V_p = 3.4 \text{ km/sec}$$

$$V_s = 1.7 \text{ km/sec}$$

$$\rho = 2.1 \text{ g/cm}^3$$

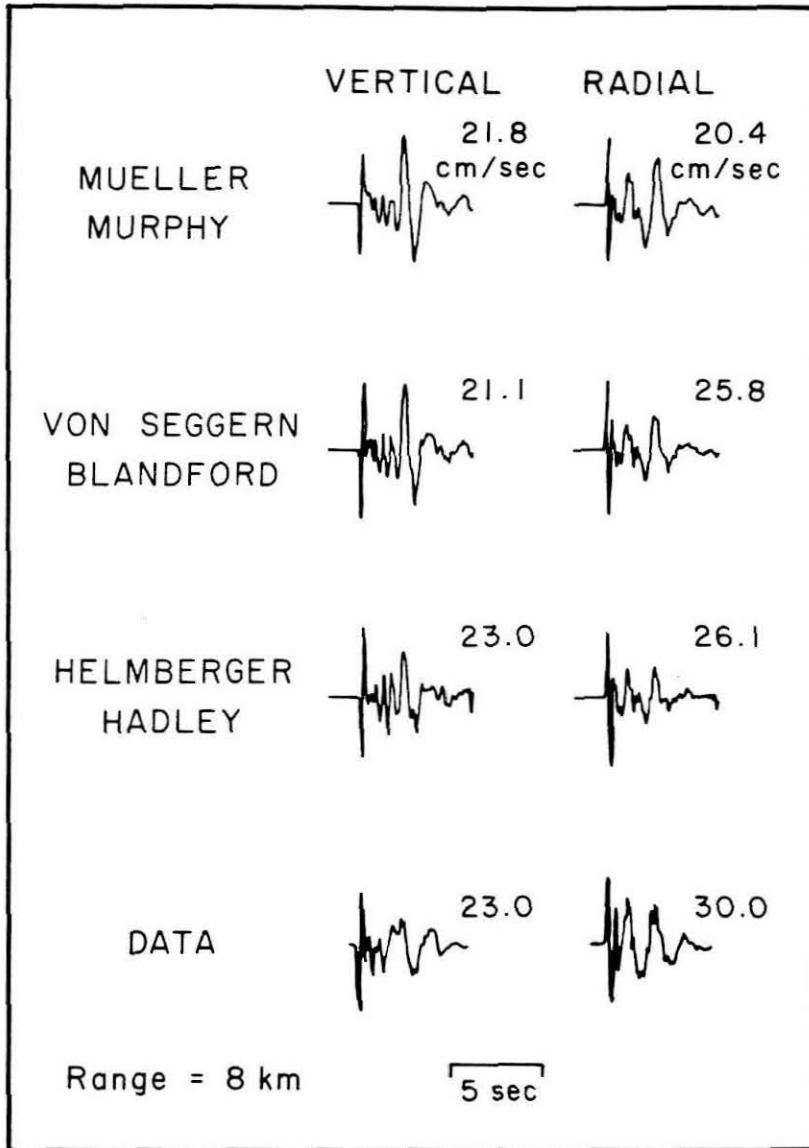


Figure 3.6 Comparison of the Helmberger-Hadley, Mueller-Murphy, and von Seggern-Blandford RDP functions used with the model shown in Figure 3.4 and the recorded velocity data at a range of 8 km. The parameters used in the RDP functions are listed in Table 3.2.

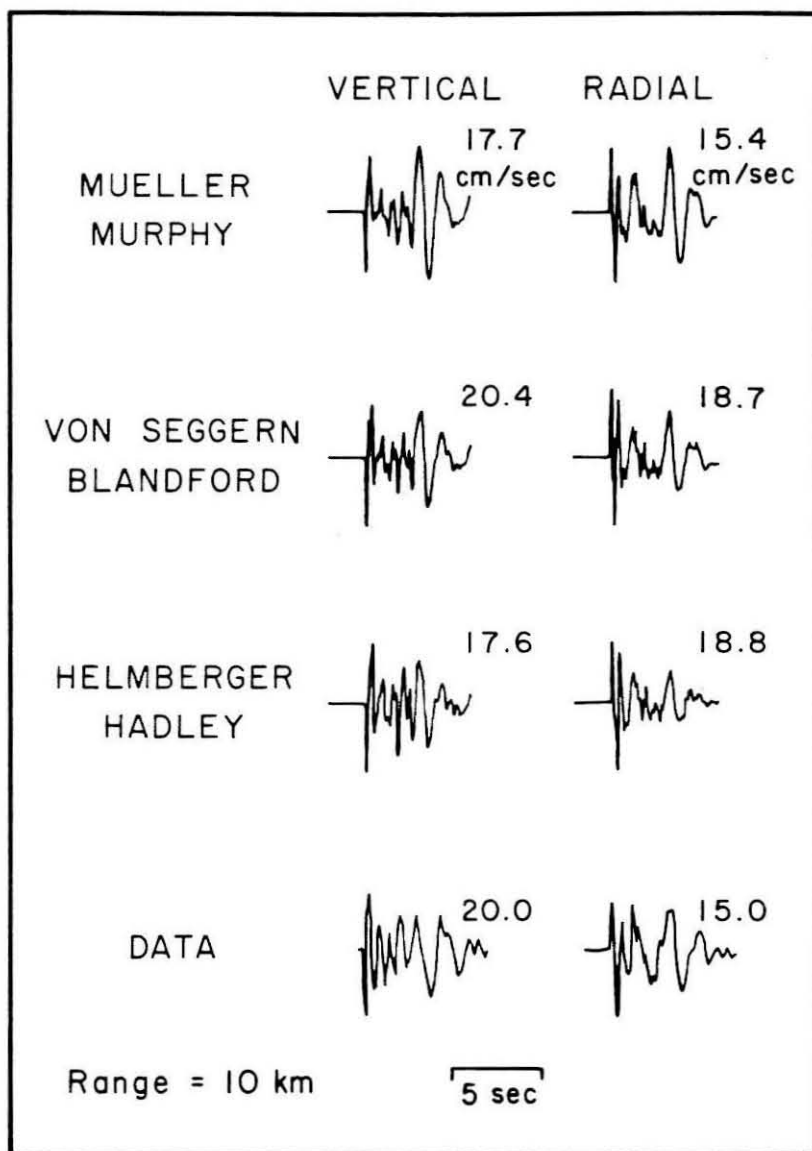


Figure 3.7 Comparison of the Helmberger-Hadley, Mueller-Murphy, and von Seggern-Blandford RDP functions used with the model shown in Figure 3.4 and the recorded velocity data at a range of 10 km. The parameters used in the RDP functions are listed in Table 3.2.

are convolved with the FD impulse responses to form the seismograms seen in Figures 3.6 and 3.7.

The amplitudes of the FD seismograms are within 35% of the those of the data in all cases, and within 20% in every case but one. The relative amplitudes of the Rayleigh wave, which is 5 seconds behind the direct arrival, vary even less than those of the direct arrivals. This observation agrees with the spectra in Figure 3.5c, where there is little difference between the different sources.

The fit to the data is good, but the differences between the synthetics for the various sources are less than the difference between the data and any of the synthetics. The differences between the data and the synthetics are of about the same size as the differences between the synthetics for different plausible structures, which are shown in Figures 3.3 and 3.4. Tilting layers which can trap a variable amount of energy and local receiver effects which amplify and de-amplify body-wave arrivals appear as important as or more important in this case than differences in the source RDP. Details of the structure must be better determined before details of the source time function can be discovered.

3.4 Conclusions

Shallow station structure and lateral velocity variations have considerable effect on the synthetic records computed for the Amchitka blast Milrow. In fact, the velocity structure is shown to be as important as or more important

than the choice of source time function parameterization in determining the ground motion for the set of strong-motion velocities, which are recorded at ranges of 6 to 12 km, that we examine in this chapter.

Chapter 4

Application to determine deep structure of subducting slabs

4.1 Introduction

The question of whether subducting slabs penetrate the 650 km discontinuity is of great concern to earth scientists. The most plausible theories of mantle convection have as end members the entire mantle overturning in a single layer of convection and two or more chemically distinct layers of mantle convection separated by a boundary near 650 km depth. To discriminate between these theories, research has been done with flow models, geoid observations, and inversions for mantle velocity models. The most detailed ideas about the geometry of slabs near and below the 650 km discontinuity are emerging from the study of travel time anomalies from deep earthquakes (Jordan, 1977, Creager and Jordan, 1984, 1986). Using shear (Jordan, 1977) and compressional (Creager and Jordan, 1984, and Creager and Jordan, 1986) wave travel time anomalies as data, and models in which only temperature and the olivine - β spinel phase changes affect velocity to constrain the geometry of the slabs, the slabs are proposed to extend to a depths greater than 1000 km.

Although these studies use only travel time data to constrain velocity models of subducting slabs, the models have implications for amplitude and waveform effects of the deep slabs. With faster computers and more advanced FD methods described in Chapter 1 and Clayton and Vidale, 1986, Vidale and

Clayton, 1986, these effects can be calculated. In this chapter, it is shown that slab structures can produce noticeable distortions of the amplitudes and waveforms for teleseismic signals from deep earthquakes. It is important to be able to calculate the distortions due to a given slab structure, both to test hypotheses about slab structure and mineralogy and to separate the effects of slab geometry from the effects of other lateral velocity variations in the mantle, anisotropy, deformation of the 650 km discontinuity and the possible effect of structure at the core-mantle boundary. It is important to realize that a high-velocity slab is an anti-waveguide. Waves are continuously refracted out of the slab, leading to waveform distortion and a reduction in amplitude.

After explaining the method, I will illustrate the wave-guide properties of a high-velocity slab with an extreme case. Finally, I will show the effect of some realistic velocity structures on the waveform and amplitudes of signals from deep earthquakes.

4.2 Waveform distortions predicted by published models

We simulate the teleseismic signals of earthquakes in slabs using a sequence of methods. The fourth order 2-D acoustic (for P waves) or SH (for S waves) finite difference (FD) scheme of Clayton and Vidale (1986) is used in the vicinity of the slab. The source is either an isotropic explosion in the acoustic case or a ring torque in the SH case. To keep the interpretation as simple as possible, we do not introduce an earthquake source. Within the FD grid, the seismic energy interacts with the high-velocity slab. Although the

seismograms may be calculated within the FD grid for distances up to 2000 km from the source, the waveforms may appear quite different at teleseismic distances. To propagate energy to distances greater than 2000 km, we first record the motions on a surface within the FD grid. From this surface, the seismic energy is propagated by the Kirchhoff scheme of Stead and Helmberger (1986) through a halfspace to a receiver 10,000 km from the source to allow the waveform to heal. Finally, the line source seismograms are transformed to point source seismograms by the line-to-point source mapping in Chapter 1.

The source in this paper is placed at 515 km depth in the middle of the high-velocity slab. The FD grid covers an area from 400 to 1400 km depth and is 1600 km wide. The simulated teleseismic signals, then, are appropriate for energy that stays in the plane perpendicular to the strike of the subducting slab. Several complexities are ignored. Ray bending after the seismic signal leaves the FD grid is not included; similarly interactions with the CMB and any triplications due to gradients outside the FD grid are not included in this analysis. I wish to isolate the effects of the slab, however, and these other effects may be included later by WKB methods, for example, once we understand the effects of the slabs.

Discussion

Consider how a subducting slab might act as a waveguide, or, more accurately, as an anti-waveguide. A simple, but extreme model of a slab surrounded by warmer and therefore slower mantle material is a 80 km thick layer with compressional wave velocity of 10 km/sec surrounded on either side by two halfspaces with a velocity of 9 km/sec. The results of the FD method

coupled with Kirchhoff method are shown in Figure 4.1.

The effects of a high-velocity layer at teleseismic distances may be seen in Figure 4.1. For the case of a receiver directly below a source ($i = 0^\circ$) in a slab, the initial arrivals with a take-off angle near the vertical dip angle of the slab have a reduced amplitude and an earlier arrival time than if the slab had not been present. The earlier arrival time is, of course, due to passage through higher-velocity material. There are two mechanisms for amplitude loss in propagation down a high-velocity slab. The first mechanism, which is acting in this example, is diffraction out of the slab. Since the velocity in the slab is faster than velocity in the surrounding material, the wavefront in the slab becomes separated from the wavefront in the surrounding material. A sharp break in a seismic wavefront will tend to smear out as the wave propagates; this process may also be thought of as the break in the wavefront acting as a secondary source. The energy in the slab is then being drained out into the surrounding material as a diffracted wavefront. The longer the period of the energy, the more of the slab is within a wavelength or two of the edge of the slab, and the diffraction more rapidly drains the energy out into the surrounding medium. This process cannot be simulated with only geometrical rays.

The second mechanism can be calculated with a ray-tracing scheme; amplitude loss can occur through defocusing as indicated by the divergence of geometric rays. This mechanism does not act here because the bottom of the slab is flat. If the source were high-frequency enough, there would be no significant decay in amplitude in this case, at least for rays that travel down the geometric center of the slab. Conversely, if the bottom of the slab had been curved, then the high-frequency energy would lose energy due to

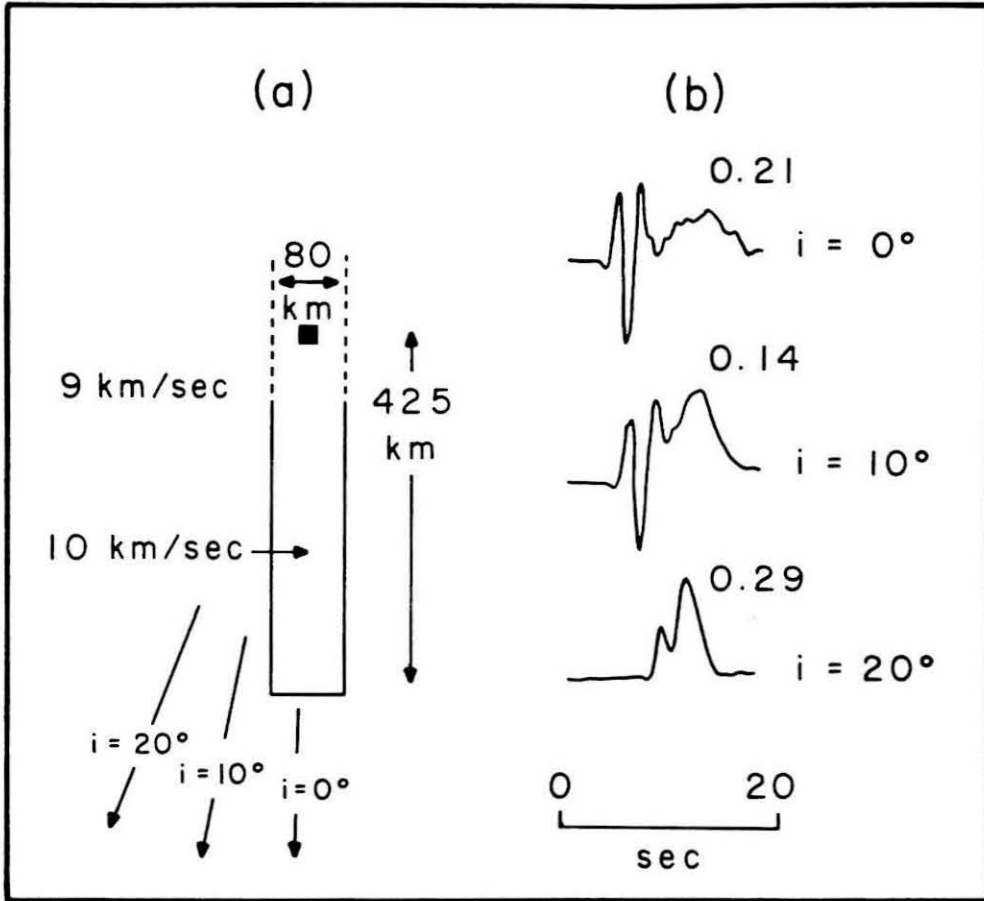


Figure 4.1 P-wave displacement waveforms distorted by propagation through a high velocity, isotropic slab. At small take-off angles, both the high-frequency, geometrical arrival and the non-geometrical lower-frequency arrival are visible. The model is shown in (a), with the source indicated by an asterisk. The receivers do not appear on this scale, but are in the direction indicated by the arrows at 0° , 10° and 20° , and are at a distance of 10,000 km. The seismograms are generated by a composite acoustic finite-difference and Kirchhoff method. The amplitudes relative to the seismograms for a uniform whole-space are printed above each trace.

defocusing.

The longer-period pulse about 8 sec behind the first arrival in the seismograms in Figure 4.1 results from long-period energy that travels in the slower surrounding media, and must diffract around the slab to reach the receiver. The second arrival has no analogue in the case where there is no slab. This pulse is not a geometrical arrival; this is clear if one considers the case of an infinitely thin, fast layer. The first, geometrical arrival will travel within the layer for some distance, but will have an infinitely small amplitude. Finite frequencies will act as if the infinitely thin layer does not exist.

As the take-off angle increases, the high-frequency arrival loses amplitude and precedes the second arrival by less time. At just past 20° , the two arrivals merge as the energy that travels down the fast slab no longer precedes the energy that travels straight from the source to the receiver. At take-off angles greater than 25° , there is little in the seismograms to indicate even the presence of a fast slab.

Figure 4.1 serves primarily to show the range of effects of a high-velocity slab; a more realistic structure is necessary to learn the effects we might expect to see in the Earth. The P-wave velocity model for the subducting slab in the Kurile-Kamchatka subduction zone for the depth range of 400-1400 km taken from Creager and Jordan (1986) is shown in Figure 4.2. Creager and Jordan (1984) show much larger velocity anomalies for the slabs, but these results arise from errors in ray tracing (pers. comm., Creager, 1986). The results for the FD-Kirchhoff scheme are also shown in Figure 4.2. The travel times are up to 3 sec early. The amplitudes for seismic energy with a take-off angle directly down the slab are reduced by a factor of 2 relative to the case with no

anomalous slab. The waveform is broadened by up to 5 sec by interaction with the fast slab.

This amount of distortion may be noticeable in the data, but the distortions in the S-waves are likely to be greater. Observations on mineral samples show that temperature induced relative changes in shear velocity are about the same as relative changes in compressional velocity (Sumino and Anderson, 1984). On the other hand, lateral velocity variations in the mantle generally show $\delta \ln V_s$ about $2\delta \ln V_p$ (e.g., Doyle and Hales, 1967, Anderson, 1986). A common physical explanation is that the shear modulus varies much more than the bulk modulus. If lateral velocity variations are primarily due to changes in the shear modulus, the percentage variation in S-wave velocity would be about twice that of the P-wave velocity.

I construct the S-wave velocity structure of the slab by multiplying the percentage anomaly from Creager and Jordan's (1986) model shown in Figure 4.2a by 9/4 and superimposing this on the mantle structure from PREM (Dziewonski and Anderson, 1981). The result is shown in Figure 4.3a. Several alternative geometries for slabs have also been proposed. Hager (1986) finds that if the lower mantle has a viscosity 100 times larger than the upper mantle, the slab flares outward as it sinks into the lower mantle. A simple flaring model is shown in Figure 4.3b, where at 1200 km depth, the slab has a width of about 500 km rather than 200 km as in Figure 4.3a. Creager and Jordan suggest that a 500 km width is less likely than a 200 km width, however, the sensitivity of travel time anomalies to the width of the slab is not well established.

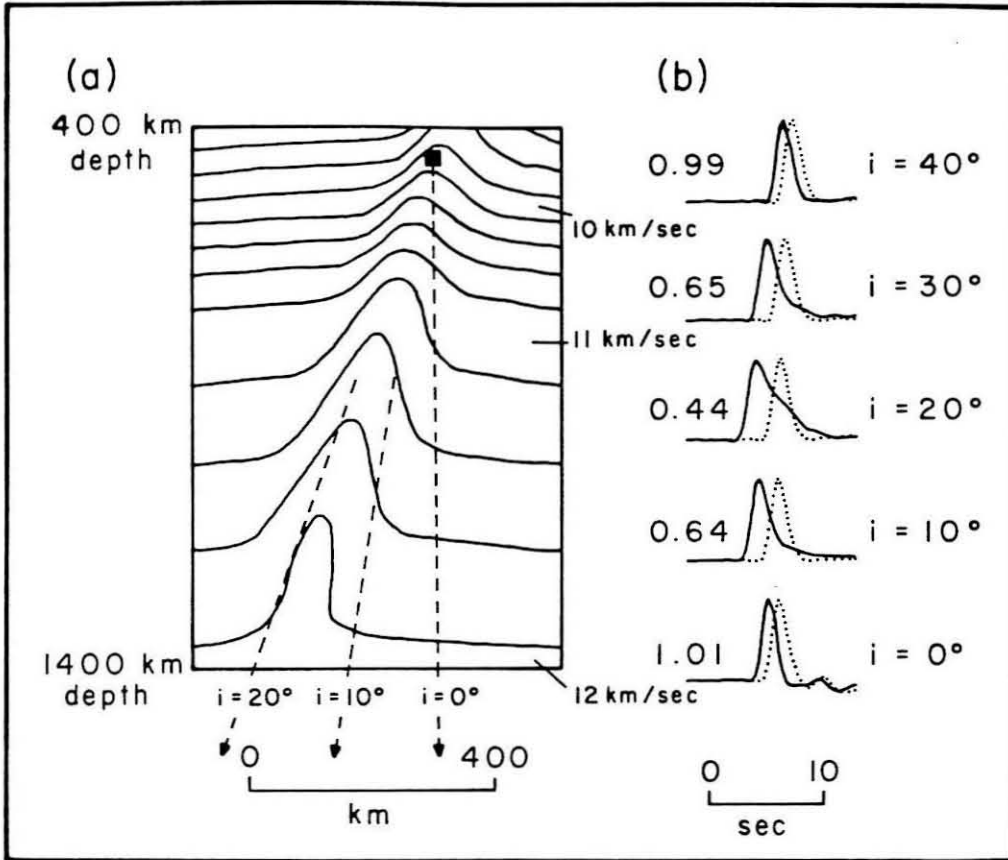


Figure 4.2 P-wave displacement waveforms distorted by propagation through a thermal model of the P-wave velocity structure of subducting slabs. This model is taken from Creager and Jordan (1986) for the slab in the Kurile-Kamchatka subduction zone. The seismograms are computed at a range of 10,000 km for take-off angles ranging from 0° to 40° . The dotted seismograms are calculated from a model with no slab velocity anomaly. Printed above each trace is the amplitude ratio of the seismograms affected by the slab to the seismograms with no slab. Lateral velocity variations are assumed to depend only on the temperature variations.

Jeanloz and Knittle (1986) and others argue that layered convection is occurring. If there is a large enough intrinsic density contrast between the upper and lower mantle, the slabs cannot penetrate the lower mantle as is indicated by the geometries in Figures 4.3a and 4.3b. If they did, the upper and lower mantles would be thoroughly mixed by now. The smoothed results from Creager and Jordan (1986) match well the smoothed pattern of travel time anomalies, so if slabs only extend to 650 km, the velocity anomalies must be stronger than indicated in Figure 4.3a to produce the same amount of travel time anomaly from a shorter travel path in the anomalous slab. Anderson (1986) finds that it is likely that the slab is composed of ilmenite minerals (the cold, high-pressure forms of enstatite, diopside, and garnet) below 400 km depth, which would be 10-20% faster than the surrounding mantle. Also, the short slab would have to be thinner than the long slab to produce even approximately the same residual sphere, at least in the isotropic case. Figure 4.3c shows such a short, thin and anomalously fast slab.

The seismograms from the models in Figure 4.3a, 4.3b, and 4.3c are shown in Figures 4.4a, 4.4b, and 4.4c. The "trim" slab derived from Creager and Jordan's (1986) model strongly affects the seismograms. The amplitude of the traces where the take-off angle is straight down the slab are a factor of three lower than for the case with no slab. The waveforms are broadened up to 20 sec by the non-geometrical arrival late in the record. The flaring slab also produces an long-period bump, though of smaller amplitude than the trim slab. The amplitude anomaly is still a factor of 2.5 for the flaring slab. The thin slab has such a narrow wave guide that the arrival begins gradually and even the upswing is broadened. The amplitude anomaly is again a factor of

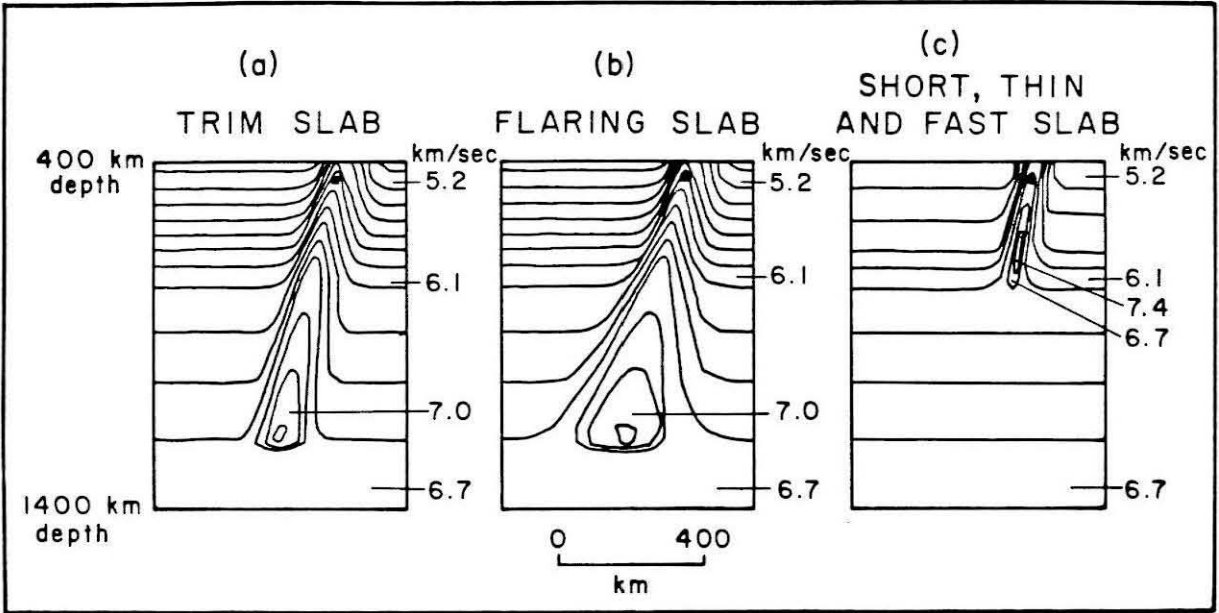


Figure 4.3 Possible isotropic S-wave velocity structures for subducting slabs. (a) shows a structure similar to Figure 4.2a, but with twice the percentage anomaly as the P-wave slab model. (b) shows a model of a slab that flares out as it sinks deeper in the lower mantle. (c) shows a slab that ends at a 700 km depth, but has a 20% velocity anomaly in its center. This short, fast slab is also only half as wide as the slab in (a).

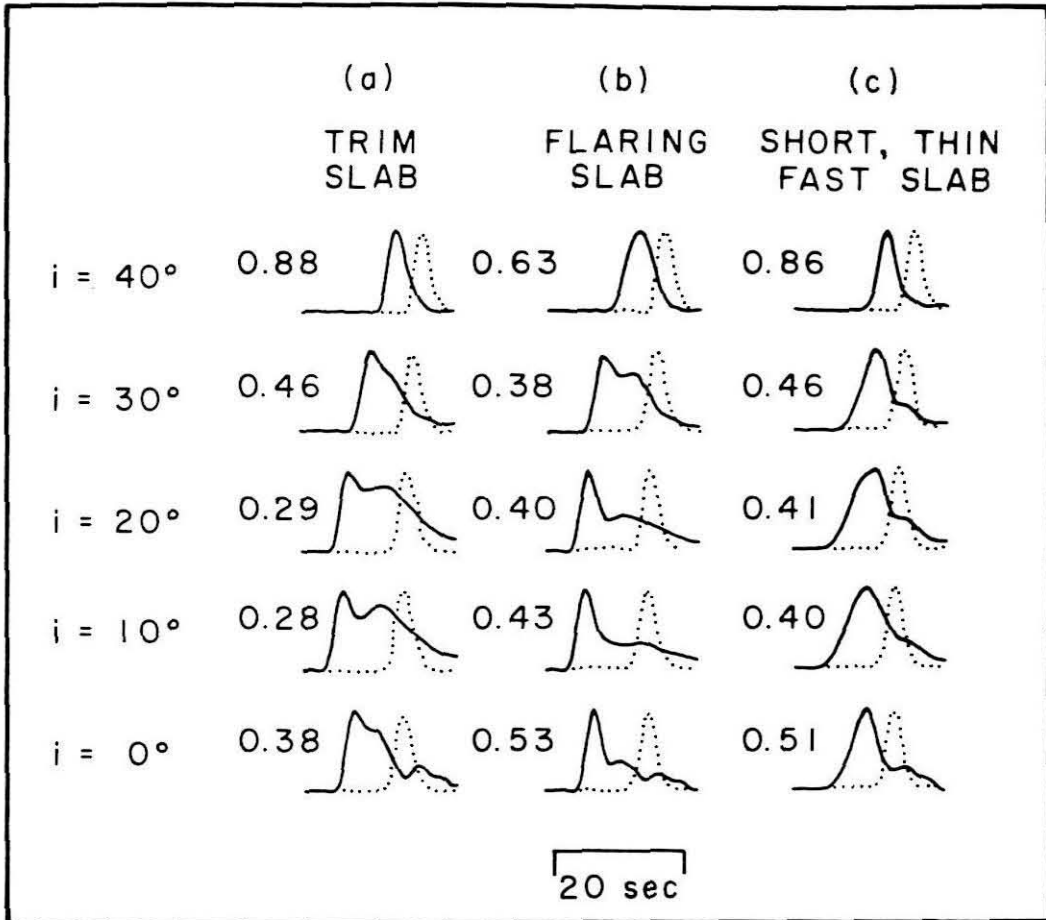


Figure 4.4 SH displacement waveforms distorted by propagation through the 3 models of the S-wave velocity structure shown in Figure 4.3. The seismograms are computed at a range of 10,000 km for take-off angles ranging from 10° to 40° . The dotted seismograms are calculated from a model with no slab velocity anomaly. Printed above each trace is the amplitude ratio of the seismograms affected by the slab to the seismograms with no slab. The take-off angle of $i = 20^\circ$ corresponds to rays taking off directly down dip.

2.5, and the broadening is again up to 10 secs.

These results suggest that the anomalous effects of the slab would be spread over a range of $20-30^\circ$ in take-off angle. A careful analysis of Figure 4.4 shows that, as one expects, the flared slab produces a wider band of fast arrivals than the trim slab. The figure also suggests, however, that the best discriminant between the slab models is the waveform and amplitude data. S-waves may determine slab structure better than P-waves because the S-wave velocity anomalies are probably larger, as mentioned above. P-waves, however, have the advantage that Q has less effect.

Broadening of the S-wave displacement pulses of up to 20 sec has been observed for seismic signals from deep earthquakes by Silver and Chan (1985). His observations have an azimuth and range that suggest the seismic energy took off from the source along the slab. Silver and Chan's (1985) data varies more rapidly with takeoff angle than the synthetic seismograms generated in this paper, suggesting that his broadened waveforms are the result of some structure closer to the stations than the slab. Beck and Lay (1986) examined numerous S and ScS records from deep earthquakes at various azimuths and failed to see a systematic pattern of waveform broadening.

4.3 Conclusions

The effects on waveform and amplitude of competing isotropic models for the velocity structure in the area of subducting slabs may be calculated. The anomalous features of these models are of an observable magnitude.

The anomalous features are of three kinds. First, the faster material in the slab advances the arrivals that leave the source region in the plane of the slab, as has been noted previously (e.g. Sleep, 1973, Jordan, 1977). This feature can be most easily investigated by ray-tracing. Second, the faster material in the slab tends to defocus energy leaving the source region in the plane of the slab. This anomaly can also be investigated by ray-tracing, although smooth models would be required and the results from standard ray-tracing are only correct for infinite frequency. Third, the waveforms of energy that leaves the source region in this direction can be distorted, with emergent first arrivals and long-period, late diffracted arrival, which can make the full waveform appear as a broadened pulse rather than simply the source time function convolved with a Q operator as it would if there were no structure. Some type of full wave theory is required to properly reproduce these effects.

We have developed a scheme that combines an FD algorithm with a Kirchhoff surface, and can properly treat all three of the above features. We do not address the travel time anomalies, as they are investigated elsewhere (Creager and Jordan, 1986). In general, thinner slabs of a given length produce more waveform broadening and smaller amplitudes for signals that leave the source region in the plane of the slab. Amplitude anomalies are more sensitive to details in the structure, but, for the structures used in this note, are large enough to be observable.

In a preliminary comparison with the finite-difference-Kirchhoff synthetic seismograms, a profile of long-period WWSSN records shows no obvious effect of the slabs (Vidale and Helmberger, 1986). Also, we see no obvious difference between record sections along the strike of the Kurile Islands slab and record

sections perpendicular to the strike. This suggests that the slab becomes thicker with depth or the slab velocity anomaly is less than has been proposed. Reconciliation of the amplitude, waveform distortion, and timing of body waves from deep events is necessary to understand the geometry of slabs near and below the 650 km discontinuity. Anisotropy near the source can also give azimuthal travel time residuals and complicates the problem of inferring slab structure.

References

Aki, K., P.G. Richards, *Quantitative Seismology, theory and methods*, W.H. Freeman and Co., San Francisco, 1980.

Alewine, R.W., III, Application of linear inversion theory toward the estimation of seismic source parameters, *Ph.D. Thesis*, California Institute of Technology, Pasadena, California, 303 pp., 1974.

Alford, R.M., K.R. Kelley and D.M. Boore, Accuracy of finite-difference modeling of the acoustic wave equation, *Geophysics*, 39, 834-842, 1974.

Allen, C.R., T.C. Hanks, and J.H. Whitcomb, San Fernando earthquake: Seismological studies and their implications, in *San Fernando, California, Earthquake of February 9, 1971, Volume I, Geological and Geophysical studies*, U.S. Government Printing Office, Washington, D.C., 1973.

Alterman, Z., and F.C. Karal, Propagation of elastic waves in layered media by finite difference methods, *Bull. Seism. Soc. Am.*, 58, 367-398, 1968.

Anderson, Don L., The mineralogy of deep slabs (abstract), *EOS Trans. AGU*, 67, 379, 1986.

Apsel, R.J., Dynamic Green's functions for layered media and applications to boundary value problems, PhD Thesis, University of California at San Diego, 1979.

Apsel, R.J. and J.E. Luco, On the Green's functions for a layered halfspace, *Bull. Seism. Soc. Am.*, 73, 909-925, 1983.

Barker, J.S., L.J. Burdick, and T.C. Wallace, Analysis of near-field seismic waveforms from underground nuclear explosions, Scientific Report No. 1, AFGL-TR-85-0321, Woodward-Clyde Consultants, Pasadena, Ca., 1985.

Beck, S.L., and T. Lay, Effects of lower mantle heterogeneity on broadband S and ScS displacement pulses from deep-focus earthquakes (abstract), *EOS Trans. AGU*, 67, 303, 1986.

Boore, D.M., Finite difference methods for seismic wave propagation in heterogeneous materials, in *Methods of computational physics*, v. 2, B. Alder, S. Fernbach, and M. Rotenberg, Eds., New York, Academic Press, 1-37, 1972.

Burdick, L.J., Modeling near-field and teleseismic observations from the Amchitka test site. *J. Geophys. Res.*, 89, 4373-4388, 1984.

Burdick, L.J., and G.R. Mellman, Inversion of the body waves from the Borrego Mountain earthquake to the source mechanism, *Bull. Seism. Soc. Am.*, 66, 1485-1499, 1976.

Burridge, R., E.R. Lapwood, and L. Knopoff, First motions from seismic sources near a free surface, *Bull. Seism. Soc. Am.*, 54, 1889-1913, 1964.

Butler, R.H., Surface wave analysis of the 9 April 1968 Borrego Mountain earthquake, *Bull. Seism. Soc. Am.*, 73, 879-883, 1983.

Cerveny, V., M.M. Popov and I. Psencik, Computation of seismic wave fields in inhomogeneous media, Gaussian beam approach, *Geophys. J.*, 70, 109-128, 1982.

Chapman, C. H., A new method for computing synthetic seismograms, *Geophys. J.*, 54, 481-518, 1978.

Clayton, R.W. and J.E. Vidale, Finite-difference wave simulation, in preparation, 1986.

Creager, K.C., and T.H. Jordan, Slab penetration into the lower mantle, *J. Geophys. Res.*, 89, 3031-3049, 1984.

Creager, K.C., and T.H. Jordan, Slab penetration into the lower mantle beneath the Mariana and other island arcs of the Northwest Pacific, *J. Geophys. Res.*, *91*, 3573-3589, 1986.

de Hoop, A.T., A modification of Cagnaird's method for solving seismic pulse problems, *Appl. Sci. Res.*, *B8*, 349-356, 1960.

Doyle, H.A., and A.L. Hales, An analysis of the traveltimes of S waves to North American station, *Bull. Seism. Soc. Am.*, *57*, 761-771, 1967.

Drake, L.A., and A.K. Mal, Love and Rayleigh waves in the San Fernando Valley, *Bull. Seism. Soc. Am.*, *62*, 1673-1690, 1972.

Duke, C.M., J.A. Johnson, Y. Kharraz, K.W. Campbell, and N.A. Malpiede, *Subsurface site conditions and geology in the San Fernando earthquake area*, UCLA-ENG-7206, School of Engineering, UCLA, 1971.

Dziewonski, A.M., and D.L. Anderson, Preliminary reference Earth model, *Phys. Earth Planet. Int.*, *25*, 297-356, 1981.

Ebel, J.E., and D.V. Helmberger, P-wave complexity and fault asperities: the Borrego Mountain, California earthquake of 1968, *Bull. Seism. Soc. Am.*, *72*, 413-437, 1982.

Edwards, M., C. Hsiung, D. Kosloff, M. Reshef, Elastic 3-D forward modelling by the Fourier method, expanded abstracts of the 1985 Soc. Explor. Geophys. annual meeting, 534-535, 1985.

EERL, Caltech, Strong Motion Earthquake Accelerograms, vol. II, Report from Earthquake Engineering Research Laboratory, California Institute of Technology, Pasadena, California, 1974.

Engdahl, E.R., Seismic effects of the MILROW and CANNIKIN nuclear explosions, *Bull. Seism. Soc. Am.*, *62*, 1411-1423, 1972.

Fuis, G.S., W.D. Mooney, J.H. Healy, G.A. McMechan, and W.J. Latter, A seismic refraction survey of the Imperial Valley region, California, *J. Geophys. Res.*, *89*, 1165-1189, 1983.

Gilbert, F. and L. Knopoff, The directivity problem for a buried line source, *Geophysics*, *26*, 626-634, 1961.

Hager, B.H., Fluid dynamics of the 670 discontinuity, *EOS Trans. AGU*, *67*, 381, 1986.

Hanks, T.C., Strong ground motion of the San Fernando, California earthquake: ground displacements, *Bull. Seism. Soc. Am.*, *65*, 193-225, 1975.

Harkrider, D.G., Potentials and displacements for two theoretical sources, *Geophys. J.*, *47*, 97-133, 1976.

Heaton, T.H., The 1971 San Fernando earthquake: a double event? *Bull. Seism. Soc. Am.*, *72*, 2037-2062, 1982.

Heaton, T.H., and D.V. Helmberger, A study of the strong ground motion of the Borrego Mountain, California, earthquake, *Bull. Seism. Soc. Am.*, *67*, 315-330, 1977.

Helmberger, D.V., Theory and application of synthetic seismograms, earthquakes: observations, theory and observations. Proceedings of the International School of Physics, Course LXXXV, edited by H. Kanamori and E. Boschi, 1983.

Helmberger, D.V., G.R. Engen, and S.P. Grand, Notes on wave propagation in laterally varying structure, *Geophys. J. R. astr. Soc.*, *58*, 82-91, 1985.

Helmberger, D.V., and D.M. Hadley, Seismic source functions and attenuation from local and teleseismic observations of the NTS events JORUM and HANDLEY, *Bull. Seism. Soc. Am.*, 71, 51-67, 1981.

Helmberger, D.V., and D.G. Harkrider, Modeling earthquakes with generalized ray theory, in *Modern Problems in Elastic Wave Propagation*, edited by J. Miklovitch and J.D. Achenbach, John Wiley, New York, 1978.

Jeanloz, R. and E. Knittle, Reduction of mantle and core properties to a standard state by Adiabatic decompression, in *Chemistry and Physics of Terrestrial Planets*, S.K. Saxena, ed., Springer-Verlag, New York, pp. 275-309, 1986.

Jordan, T.H., Lithospheric slab penetration into the lower mantle beneath the sea of Okhotsk, *J. Geophys.*, 43, 473-496, 1977.

Joyner, W.B., and D.M. Boore, Peak horizontal acceleration and velocity from strong-motion records including records from the 1979 Imperial Valley, California earthquake, *Bull. Seism. Soc. Am.*, 71, 2011-2038, 1981.

Kanamori, H., and D. Hadley, Crustal structure and temporal velocity change in southern California, *Pageoph.*, 113, 257-280, 1976.

Langston, C.A., The February 9, 1971 San Fernando earthquake: a study of source finiteness in teleseismic body waves, *Bull. Seism. Soc. Am.*, 68, 1-29, 1978.

Langston, C.A., and D.V. Helmberger, A procedure for modeling shallow dislocation sources, *Geophys. J. R. astr. Soc.*, 42, 117-130, 1975.

Lay, T., D.V. Helmberger, and D.G. Harkrider, Source models and yield-scaling relations for underground nuclear explosions at Amchitka Island, *Bull. Seism. Soc. Am.*, 74, 843-862, 1984.

Liu, H.L., and T.H. Heaton, Array analysis of the ground velocities and accelerations from the 1971 San Fernando California earthquake, *Bull. Seism. Soc. Am.*, 74, 1951-1968, 1984.

Madariaga, R. and P. Papadimitriou, Gaussian Beam Modeling of Upper Mantle Phases, *Annales Geophysicae*, 3, 799-812, 1985.

Marfurt, K.J., Accuracy of finite-difference and finite-element modeling of the scalar and elastic wave equations, *Geophysics*, 49, 533-549, 1984.

McGarr, A., Scaling of ground motion parameters, state of stress, and focal depth, *J. Geophys. Res.*, 89, 6969-6979, 1984.

McCowan, D.W., P. Glover, S.S. Alexander, A static and dynamic finite element analysis of the 1971 San Fernando, California earthquake, *Geophys. J. R. astr. Soc.*, 48, 163-185, 1977.

Meuller, R.A. and J.R. Murphy, Seismic characteristics of underground nuclear detonations. Part I. Seismic spectrum scaling, *Bull. Seism. Soc. Am.*, 61, 1675-1694, 1971.

Montalbetti, J.F., and E.R. Kanasewich, Enhancement of teleseismic body phases with a polarization filter, *Geophys. J. R. astr. Soc.*, 21, 119-129, 1970.

Orphal, D.L., C.T. Spiker, L.R. West, M.D. Wronski, Analysis of seismic data, Milrow Event, Environmental Research Corporation report NVO-1163-209, 1970.

Rogers, A.M., R.D. Borchardt, P.A. Covington, D.M. Perkins, A comparative ground response study near Los Angeles using recordings of Nevada nuclear tests and the 1971 San Fernando earthquake, *Bull. Seism. Soc. Am.*, 74, 1925-1949, 1984.

Sibson, R.H., Fault zone models, heat flow, and the depth distribution of earthquakes in the continental crust of the United States, *Bull. Seism. Soc. Am.*, 72, 151-163, 1982.

Silver, P., and W. Chan, Subducted slabs in the lower mantle: evidence from bodywave multipathing (abstract), *EOS Trans. AGU*, 66, 957, 1985.

Sleep, N.H., Teleseismic P-wave transmission through slabs, *Bull. Seism. Soc. Am.*, 63, 1349-1373, 1973.

Stead, R., and D.V. Helmberger, The effect of basin geometry on surface wave propagation, *EOS Trans. AGU*, 66, 964, 1985.

Stead, R.J., and D.V. Helmberger, Numerical-Analytical interfacing in two dimensions with applications to modeling NTS seismograms, manuscript in preparation, 1986.

Stevens, J.L. and S.M. Day, The physical basis of m_b , M_S and variable frequency magnitude methods for earthquake/explosion discrimination. *J. Geophys. Res.*, 90, 3009-3020, 1985.

Strick, E., Propagation of elastic wave motion from an impulsive source along a fluid-solid interface, parts II and III, *Phil. Trans. Roy. Soc. London, Series A*, 251, 465-523, 1959.

Sumino, Y. and O.L. Anderson, Elastic constants and minerals: in CRC handbook of physical properties of rocks, Carmichael, Robert S., ed., Boca Raton, Florida, 39-138, 1984.

Trifunac, M.D., and A.G. Brady, A study on the duration of strong earthquake ground motion, *Bull. Seism. Soc. Am.*, 65, 581-626, 1975.

Vidale, J.E., Complex polarization analysis of particle motion, *Bull. Seism. Soc. Am.*, *76*, 1393-1406, 1986.

Vidale, J.E. and R.W. Clayton, A stable free-surface boundary condition for 2-D elastic finite-difference wave simulation, to appear in December, *Geophysics*, 1986.

Vidale, J.E. and D.H. Helmberger, Waveform effects of high-velocity, subducting slabs, submitted to *EOS Trans. AGU*, *68*, 1986.

Virieux, J., P-SV wave propagation in heterogeneous media: Velocity-stress finite-difference method, *Geophysics*, *51*, 889-901, 1986.

von Seggern, D. and R. Blandford, Source time functions and spectra for underground nuclear explosions, *Geophys. J.*, *31*, 83-97, 1972.

Whitcomb, J.H., C.R. Allen, J.D. Garmany, and J.A. Hileman, San Fernando earthquake series, 1971: Focal mechanisms and tectonics, *Rev. Geophys. Space Phys.*, *11*, 693-730, 1973.

Witte, D., P.G. Richards, Anelastic wave propagation by the pseudo-spectral method, *EOS Trans. AGU*, *67*, 303, 1986.